Copyright Warning & Restrictions

The copyright law of the United States (Title 17, United States Code) governs the making of photocopies or other reproductions of copyrighted material.

Under certain conditions specified in the law, libraries and archives are authorized to furnish a photocopy or other reproduction. One of these specified conditions is that the photocopy or reproduction is not to be "used for any purpose other than private study, scholarship, or research." If a, user makes a request for, or later uses, a photocopy or reproduction for purposes in excess of "fair use" that user may be liable for copyright infringement,

This institution reserves the right to refuse to accept a copying order if, in its judgment, fulfillment of the order would involve violation of copyright law.

Please Note: The author retains the copyright while the New Jersey Institute of Technology reserves the right to distribute this thesis or dissertation

Printing note: If you do not wish to print this page, then select "Pages from: first page # to: last page #" on the print dialog screen

NJIT New Jersey's Science & Technology University

The Van Houten library has removed some of the personal information and all signatures from the approval page and biographical sketches of theses and dissertations in order to protect the identity of NJIT graduates and faculty.

ABSTRACT

CORONAL MAGNETOMETRY AND ENERGY RELEASE IN SOLAR FLARES

by
Yuqian Wei

As the most energetic explosive events in the solar system and a major driver for space weather, solar flares need to be thoroughly understood. However, where and how the free magnetic energy stored in the corona is released to power the solar flares remains not well understood. This lack of understanding is, in part, due to the paucity of coronal magnetic field measurements and the lack of comprehensive understanding of nonthermal particles produced by solar flares. This dissertation focuses on studies that utilize microwave imaging spectroscopy observations made by the Expanded Owens Valley Solar Array (EOVSA) to diagnose the nonthermal electrons and coronal magnetic field in solar flares.

In the first study, a partial eruption of a twisted solar filament is observed in Hα and extreme ultraviolet (EUV) wavelengths during an M1.4-class solar flare on September 6, 2017. The microwave counterpart of the filament is observed by EOVSA. The spectral properties of the microwave source are consistent with nonthermal gyrosynchrotron radiation. Using spatially resolved microwave spectral analysis, the magnetic field strength along the filament spine is derived, which ranges from 600–1400 Gauss from its apex to the legs. The results agree well with the non-linear force-free magnetic model extrapolated from the pre-flare photospheric magnetogram. The existence of the microwave counterpart also suggests that the newly reconnected magnetic field lines have the flare-accelerated electrons injected into the filament-hosting magnetic flux rope cavity.

The second study focuses on another eruptive solar flare event that features three post-impulsive X-ray and microwave bursts immediately following its main

impulsive phase. A tight positive correlation between the flux rope acceleration and electron energization is found during the post-impulsive phase bursts, conforming to the standard flare–coronal-mass-ejection scenario, in which positive feedback between flare reconnection and flux rope acceleration is expected. In contrast, such a correlation does not seem to hold during its main impulsive phase. The lack of flux rope acceleration during the main impulsive phase, as interpreted in this dissertation, is mainly attributed to the tether-cutting reconnection scenario when the flux rope eruption has not been fully underway. In addition, observations suggest a weakening guide field may contribute to the hardening of the nonthermal electron spectrum throughout the main- and post-impulsive phase of the event, shedding new light on understanding the electron acceleration mechanisms in solar flares.

CORONAL MAGNETOMETRY AND ENERGY RELEASE IN SOLAR FLARES

by
Yuqian Wei

A Dissertation
Submitted to the Faculty of
New Jersey Institute of Technology and
Rutgers, The State University of New Jersey – Newark
in Partial Fulfillment of the Requirements for the Degree of
Doctor of Philosophy in Applied Physics

Department of Physics

May 2023

Copyright © 2023 by Yuqian Wei
ALL RIGHTS RESERVED

APPROVAL PAGE

CORONAL MAGNETOMETRY AND ENERGY RELEASE IN SOLAR FLARES

Yuqian Wei

Dr. Bin Chen, Dissertation Advisor — Date
Associate Professor of Physics, NJIT

Dr. Haimin Wang, Dissertation Co-Advisor — Date
Distinguished Professor of Physics, NJIT

Dr. Dale E. Gary, Committee Member — Date
Distinguished Professor of Physics, NJIT

Dr. Gregory Fleishman, Committee Member — Date
Distinguished Research Professor of Physics, NJIT

Dr. Jason T. L. Wang, Committee Member — Date
Professor of Computer Science, NJIT

BIOGRAPHICAL SKETCH

Author: Yuqian Wei

Degree: Doctor of Philosophy

Date: May 2023

Undergraduate and Graduate Education:

- Doctor of Philosophy in Applied Physics,
  New Jersey Institute of Technology, Newark, NJ, 2023
- Bachelor of Science in Physics,
  Jilin University, Jilin, Changchun, China, 2013

Major: Applied Physics

Presentations and Publications:

[1] **Yuqian Wei**, Bin Chen, Sijie Yu, Haimin Wang, Ju Jing, and Dale E. Gary., "Coronal Magnetic Field Measurements along a Partially Erupting Filament in a Solar Flare," *The Astrophysical Journal*, 923 (2): 213., 2021.

[2] **Yuqian Wei**, Bin Chen, Sijie Yu, Haimin Wang, Yixian Zhang, and Lindsay Glesener, "Energy Release During the Post Main Impulsive Phase of a Solar Flare," *The Astrophysical Journal, under preparation*, 2023

[3] Jiale Zhang, Bin Chen, Sijie Yu, Hui Tian, **Yuqian Wei**, Hechao Chen, Guangyu Tan, Yingjie Luo, and Dale E. Gary., "Implications for Additional Plasma Heating Driving the Extreme-ultraviolet Late Phase of a Solar Flare with Microwave Imaging Spectroscopy," *The Astrophysical Journal*, 932 (2): 53., 2022.

[4] **Yuqian Wei**, Bin Chen, Sijie Yu, "Energy Release During the Post Main Impulsive Phase of an Eruptive Solar Flare" *Presentation*, Triennial Earth-Sun Summit (TESS) , Bellevue/Seattle, WA, August 8-11, 2022.

[5] **Yuqian Wei**, Bin Chen, Sijie Yu, Haimin Wang, Ju Jing, and Dale E. Gary. "Magnetic Field Measurements Of A Twisted Flux Rope In A Failed Solar Eruption," *Presentation*, American Astronomical Society (AAS), Virtual, June, 2021.

[6] **Yuqian Wei**, Bin Chen, "Joint GST and EOVSA Observation of an M1.4 Flare on 2017 Sep 6," *Presentation*, American Astronomical Society (AAS)/Solar Physics Division (SPD) Meeting 51, Virtual, August 18-19, 2020.

[7] **Yuqian Wei**, Bin Chen, Sijie Yu, Haimin Wang, "Joint GST and EOVSA Observation of an M1.4 Flare on 2017 September 6," *iPoster Presentation*, American Astronomical Society (AAS)/Solar Physics Division (SPD) Meeting 50, St. Louis, MO, June 9-13, 2019.

To my family

ACKNOWLEDGMENT

I would like to thank all those who have contributed to the successful completion of this Ph.D. dissertation.

First and foremost, I would like to express my deepest gratitude to my advisor, Dr. Bin Chen. Throughout my doctoral studies, he guided me to think, perform analysis, cooperate, and present/express as a scientist; Helps me focus on and try to solve the scientific problem that may contribute to the solar physics community. Helps me build a big picture and passion for the research I did with his deep insight. I cannot express my gratitude enough to Dr. Bin Chen, a mentor and a friend of mine, his patient instruction would encourage me throughout my research career.

Likewise, my deepest gratitude goes to my advisor Dr. Haimin Wang, who not only gave me insightful guidance in academics but also gave me valuable advice on my academic and career planning. When I faced any difficulties, his patience and thoughtfulness guidance always helped me stay positive.

I am grateful to the members of my dissertation committees, particularly to Dr. Dale E. Gary, whose constant efforts on EOVSA form the foundation of this dissertation. Throughout my doctoral studies, I continuously learned from him through his lectures, group meetings, and discussions. Thanks to Dr.Gregory Fleishman for giving me much help with the theoretical perspective, especially through the discussions in the journal clubs. I would also like to thank Dr. Jason T. L. Wang for his suggestions from the perspective of statistical science and for being my committee member.

I would like to thank Dr. Sijie Yu in particular. His patience in answering my questions is greatly appreciated. Throughout my entire Ph.D. journey, he has provided me with invaluable experience, guidance, and feedback on my studies. My

works also benefit a lot from his software development and his persistent efforts on the EOVSA data pipeline.

I would like to express my sincere gratitude to all the professors, colleagues, and fellow students in the solar radio group. I am grateful to Dr.Surajit Mondal for his help in terms of instrumentation and his diligent efforts in the EOVSA data product; to Dr.Gelu M. Nita for developing the inspiring software and for his assistance in software development and utilization. I am grateful to all my classmates Yingjie Luo and Meiqi Wang, with whom I had many discussions and from whom I have learned a lot from their paper sharing in the journal clubs. I want to express my appreciation to all the fellow students in our group, Shaheda Shaik, Sherry Chhabra, Yi Chai, Natsuha Kuroda, Brian O'Donnell, Ivan Oparin, Stasia Kuske, and Sabastian Fernades. Their work really opened my eyes. I would also like to thank Dr. Owen Giersch for his constant maintenance of EOVSA.

I would also like to thank Dr.Yan Xu, Dr.Ju Jing, Dr.Jeongwoo Lee, and Dr.Satoshi Inoue who have continuously provided feedback and suggestions on my work with many valuable comments and ideas from the perspective of low solar atmospheric processes, flare geometry, magnetic field extrapolation, and MHD simulations. They have greatly expanded the observational options that I apply to the event. Thanks to Dr.Wenda Cao who gave me many suggestions and instructions. I would also like to give special thanks to my classmates, Nian Liu, Jiasheng Wang, Qin Li, Ying Wang, and Xu Yang, not only for the discussions they had with me on my studies but also for the help and concern they gave me as friends. Their companionship helped me get through the most difficult times.

My work and graduate studies would not have been possible without the help of administrative staff in various departments: Many thanks to Ms.Cheryl James and Ms.Christine A Oertel for helping me with all the paper works; to Ms.Clarisa

Gonzalez-Lenahan for helping me with my campus life as an international student and reviewing my dissertation.

I would also like to acknowledge NSF and NASA for the supporting grants.

This precious stage of life would not have been possible without my wife Nengyi Huang and the little feline family member, Nebula. Finally, my parents, Dong Wei and Lin Li, are the heroes of my life.

TABLE OF CONTENTS

TABLE OF CONTENTS
(Continued)

Chapter **Page**

LIST OF TABLES

LIST OF FIGURES

CHAPTER 1

INTRODUCTION

1.1 Solar Flares

1.1.1 Observations of solar flares

Ever since the first reported observation [32], solar flares, the most violent energy release in the solar system, have been extensively observed. Although *in situ* detection of flare-accelerated particles has been frequently reported, remote-sensing observations of flare radiation at multiple wavelengths remain the most important means of studying solar flares. Flare radiation covers a wide range of the electromagnetic spectrum, observed by both ground-based and space-based instruments from radio to γ-ray wavelengths. Soft X-ray (SXR) flux at the 1–8 Å channel measured by the Geostationary Orbiting Environmental Satellites (GOES) has been used to classify flares owing to its sensitivity to the flare-heated hot plasma and the long-term operation of the GOES satellites. As shown in Table 1.1, the flares are classified into X-, M-, C-, B-, and A- classes according to the logarithm of the peak flux of the GOES 1–8 Åchannel. The number following the class category letter indicates the linear scale within the same category. For example, the top 2 largest flares of solar cycle 24, the X9.3 class flare on September 6, 2017, and the X8.2 class flare on September 10, 2017, have a peak flux of $9.8 \times 10^{-4}\ W/m^2$ and $8.2 \times 10^{-4}\ W/m^2$, respectively [111]. Unlike the other categories, there is no upper class above X. The largest flare that has been ever observed by GOES is the X28 flare that occurred on November 4, 2003 [254].

The multi-wavelength observation of the flare is critical for people to understand the temporal evolution of solar flares, which is characterized by varying time intervals seen at or dominated by various wavelengths. As shown in Figure 1.1, solar flares, in

Table 1.1 GOES Flare Category

Class	*Peak Flux* $(W/m^2)^a$
X	$I > 10^{-4}$
M	$10^{-5} < I < 10^{-4}$
C	$10^{-6} < I < 10^{-5}$
B	$10^{-7} < I < 10^{-6}$
A	$I < 10^{-7}$

[a]The classification is based on the SXR peak flux in 1-8 Å.

general, can be divided into three phases. The dotted lines in Figure 1.1 demarcate the representative flare time history into the "pre-flare phase", "impulsive phase", and "decay phase". In some cases, the "flash phase" is specifically designated as the late-impulsive phase, when the $H\alpha$ intensity increases rapidly. These flare phases will be discussed in more detail in Subsection 1.1.2 in the context of flare models.

1.1.2 Energy build-up and release in standard flare model

In the solar atmosphere, the magnetic field free energy dominates over the thermal and gravitational potential energy and is the only source of energy that is capable of powering solar flares. Free magnetic energy is defined as the extra energy compared to a fully relaxed potential field, which can be expressed as [168]:

$$E_{\rm ff} = \frac{1}{\mu_0} \int_{xy} B_z \left[x \left(B_x - B_{x,p} \right) + y \left(B_y - B_{y,p} \right) \right] {\rm d}x \ {\rm d}y \tag{1.1}$$

$$E_{free} = \int_V \frac{B^2}{8\pi} dV - \int_V \frac{B_p^2}{8\pi} dV \tag{1.2}$$

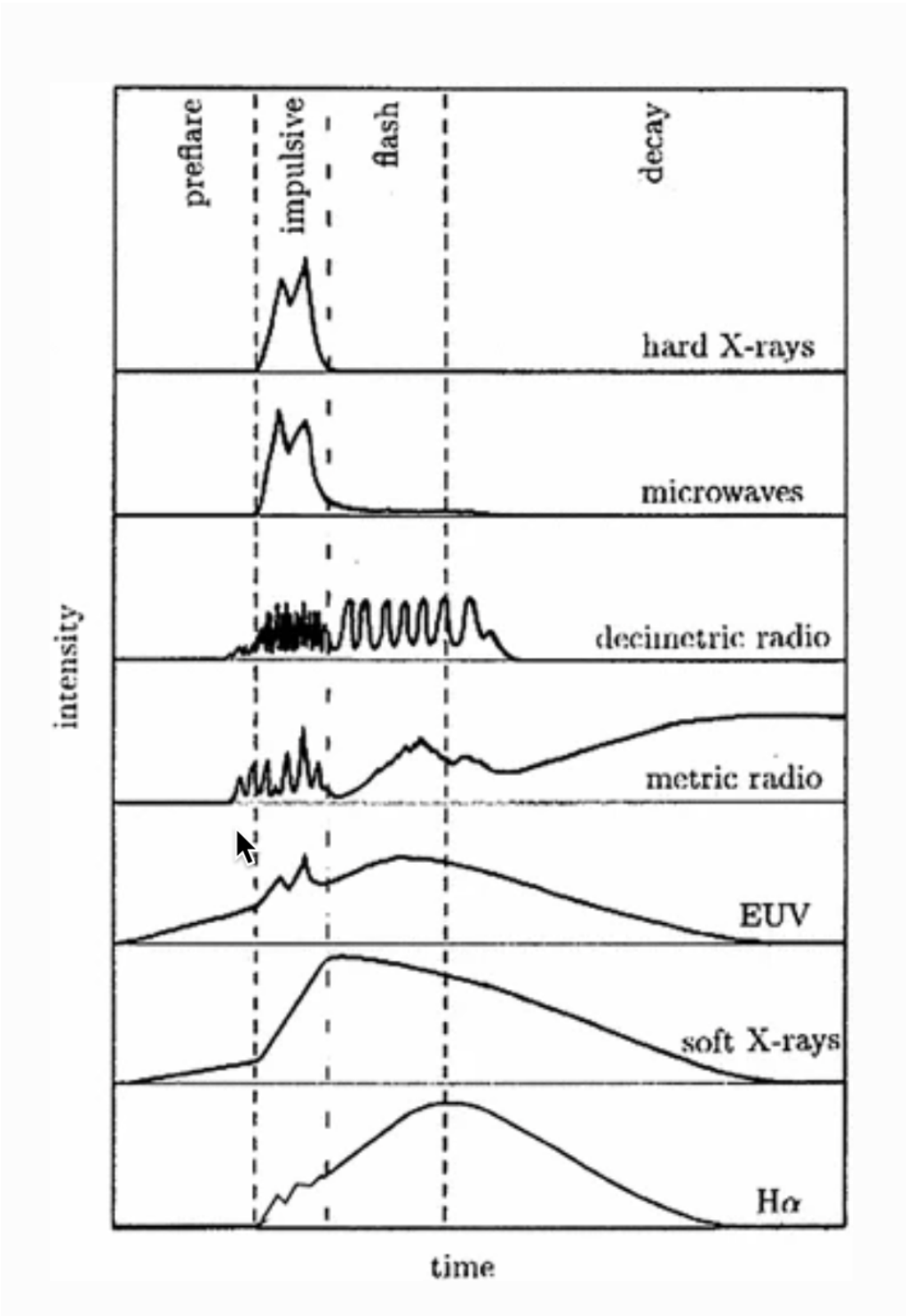

Figure 1.1 Schematic flux time-profile of flare in multi-frequencies. Typically, solar flares are divided into three phases with dotted lines in the figure, referred to as stages "pre-flare phase", "impulsive phase", and "decay phase". In some cases, the "flash phase" is specifically designated as the late-impulsive phase, when the $H\alpha$ intensity increase rapidly)
(Source: [18])

It is generally acknowledged that free magnetic energy is the source of energy for solar flares. Compared to the lower atmosphere, the corona has a large enough volume to store the free magnetic energy. The assumption is strongly supported by a recent observational study [72] about the coronal magnetic field strength measurement on X8.2 class flare occurs on Sep 10, 2017, in which the coronal magnetic field decays at a rate of $\sim$5 G/s for $\sim$ 2 minutes (Figure 1.3). With the increasing number of large flare observations and modernized photospheric vector magnetic field measurements, a close correlation between the non-potentiality of the active region and their evolution is revealed. The non-potentiality of the active region strongly attributes to magnetic shearing and new flux emergence [137, 103, 233], which are often reflected as δ photospheric magnetic field configuration, highly sheared polarity inversion lines, formation of magnetic flux ropes, etc [233]. Figure 1.2 shows the evolution of magnetic fields of AR12673 which is well-known for its high flare productivity.

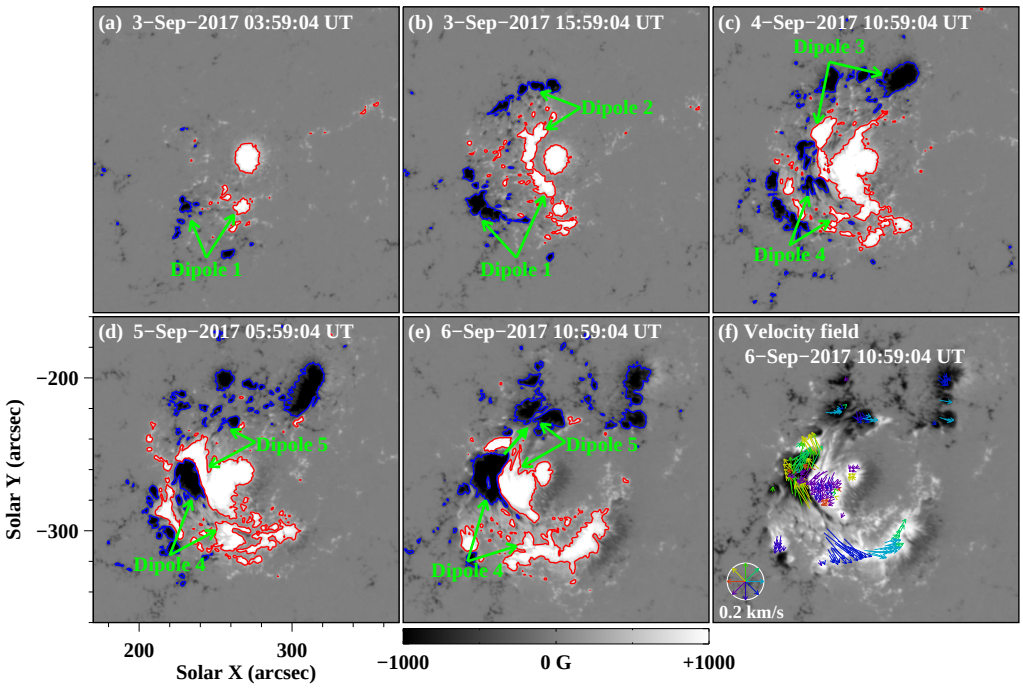

Figure 1.2 Evolution of magnetic fields in AR 12673 from Sep 3 to 6, 2017 *(Source: [111])*

However, the question of how, where, and when the free magnetic energy stored in the lower corona is released is still not well understood. Multi-wavelength observations not only allow a more complete coverage of solar flares over their lifespan, but also probe the thermal plasma and nonthermal particles in and around the flaring region. Meanwhile, three-dimensional magnetic field mapping of ARs and flares is crucial for understanding and modeling solar flares.

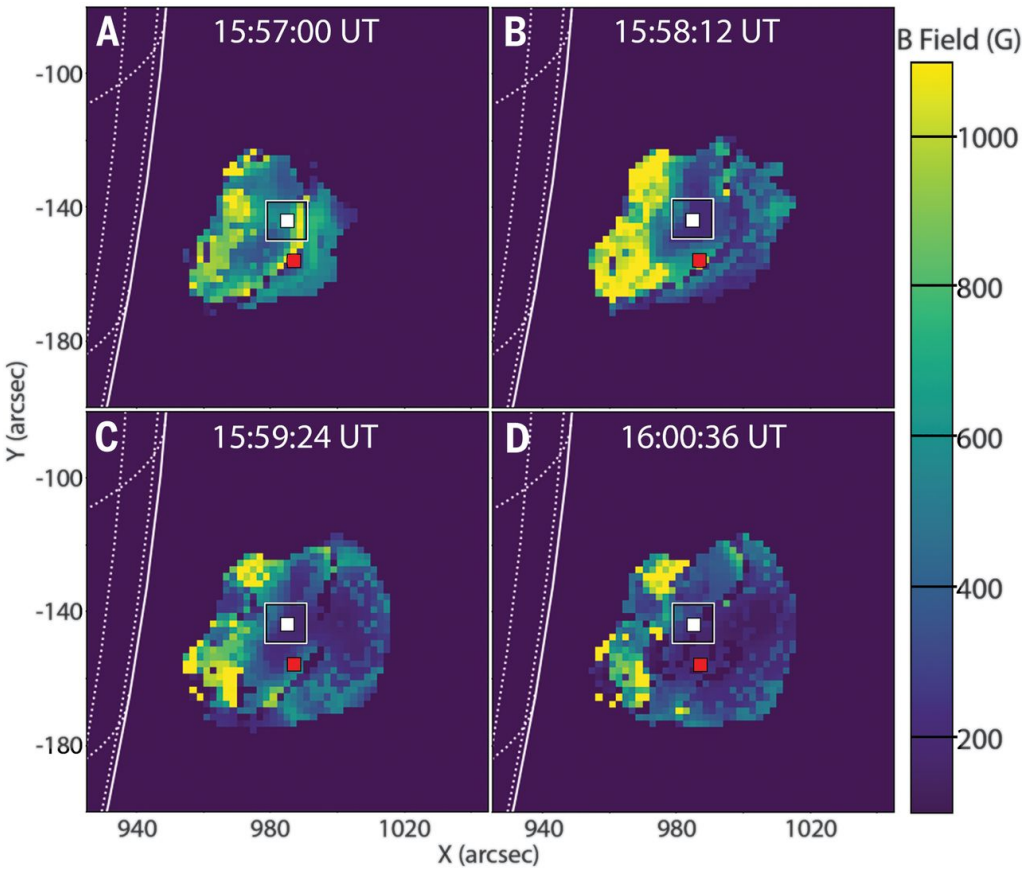

Figure 1.3 coronal magnetic field maps derived for the 10 September 2017 flare, separated by 72 s.
(Source: [72])

The X-ray emission during the solar flares is mainly due to the bremsstrahlung radiation [196], which arises from the Coulomb collision between the electrons and the much heavier ions in the ionized plasma. According to the energy of the emitted photons, X-ray radiation can be categorized into soft X-ray (SXR, $E_{photon} \lessapprox 10\ keV$)

and hard X-ray (HXR, $E_{photon} \gtrapprox 10\ keV$). During solar flares, coronal loops can be filled with plasma that is heated from 1.5 MK to over 30 MK [60, 19]. The thermal electrons (following the Maxwellian distribution [59]) in the plasma produce strong emission in SXR and Extreme ultraviolet (EUV) wavelength [247]. As shown in an example in Figure 1.4, the bright SXR source takes the shape of an arcade, which corresponds to reconnected magnetic field lines anchored at the photosphere. The photon flux density of thermal bremsstrahlung (in units of $\mathrm{cm}^{-2}\ \mathrm{s}^{-1}\ \mathrm{keV}^{-1}$) observed at a distance of d is expressed as [108]:

$$I(\epsilon) = \frac{1}{4\pi d^2} \int_V \int_\epsilon^\infty n_{i^+}(\mathbf{r}) f_{e^-}(E, \mathbf{r}) \sigma_{ff}(\epsilon, E) dE dV, \tag{1.3}$$

where ϵ and E are the energy of the photon and the involved electron, respectively. n_{i^+} is local ion density. f_{e^-} is the thermal electron energy distribution function, which can be expressed as [227]:

$$f_e^-(E) = \frac{2n_e^-}{\pi^{1/2}(kT)^{3/2}} E^{1/2} \exp(-E/kT) \tag{1.4}$$

And $\sigma_{ff}(\epsilon, E)$ in Equation (1.3) is the angularly averaged, non-relativistic cross-section based on Bethe-Heitler approximation [21], expressed as [227]:

$$\sigma_{ff}(\epsilon, E) = \frac{7.9 \times 10^{-25} \overline{Z^2}}{\epsilon E} \ln \frac{1 + (1 - \epsilon/E)^{1/2}}{1 - (1 - \epsilon/E)^{1/2}}, \tag{1.5}$$

where $\overline{Z^2}$ is the square of the abundance-weighted mean atomic number, which is $\simeq 1.4$ in solar atmosphere [68]. Therefore, the spectrum of the X-ray emission due to thermal bremsstrahlung serves as an excellent diagnostic tool for the plasma temperature and density (or "emission measure"). The SXR emission from the coronal loop increases rapidly during the impulsive phase, as shown in Figure 1.1, indicating a rapid increase of the thermal energy within the reconnected flare loops.

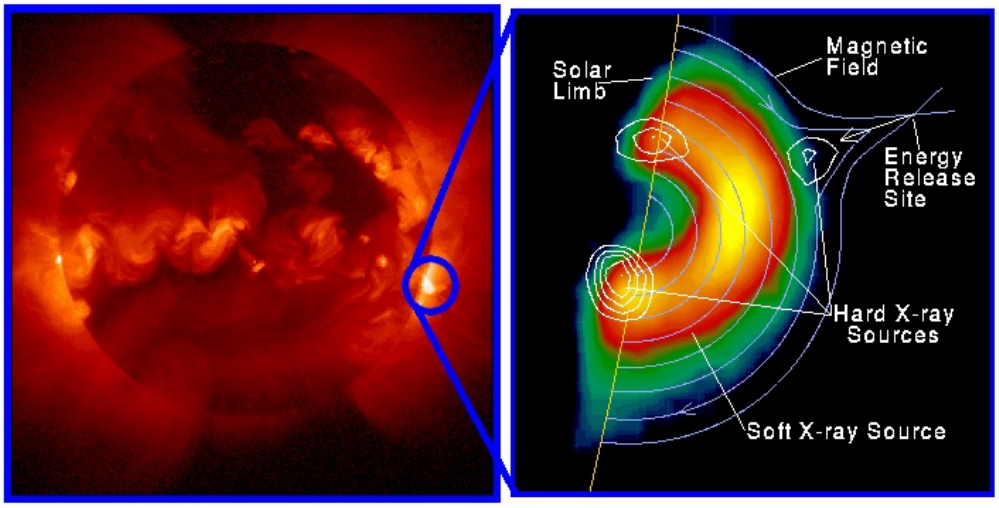

Figure 1.4 Soft X-ray and hard X-ray imaging of a limb event on Jan 13, 1992. Left: full-disk soft X-ray image of the Sun, taken with the Yohkoh Soft X-ray Telescope. Right: hard X-ray (white contour) taken with the Yohkoh hard X-ray Telescope overplotted on zoomed soft X-ray intensity map and schematic magnetic field line. *(Source: Yohkoh imaging team and NASA/Goddard)*

The hard X-ray emission, on the other hand, is dominated by the bremsstrahlung radiation between ions and nonthermal electrons from a few tens of kilo-electron volts (keV) to >100 keV. The latter has a distribution that does not follow the Maxwellian distribution [26]. As shown in Figure 1.4, two lower (closer to the solar surface) HXR sources, usually referred to as "footpoint source," connect the coronal loop outlined by the SXR source. These footpoint sources are the most commonly observed HXR sources during solar flares. They are located in the solar chromosphere. Spectral analysis reveals that certain HXR sources can extend to up to 250–500 keV [138, 108]. For a given region, if the nonthermal electrons can dissipate most of their energy through Coulomb collisions within the observation time, the case falls into the "thick-target" regime. In comparison, when the energy loss is insignificant, the case falls into the "thin-target" regime. The expressions for the X-ray flux density

expected from the two bremsstrahlung regimes are, respectively [26, 108]:

$$I_{\mathbf{thick}}(\epsilon) = \frac{1}{4\pi R^2}\frac{1}{\bar{Z}K}\int_{E_0=\epsilon}^{\infty} F_{e^-}(E_0)\int_{E=\varepsilon}^{E_0} E\sigma(\epsilon, E)dEdE_0 \tag{1.6}$$

$$I_{\mathbf{thin}}(\epsilon) = \frac{n_{i^+}V}{4\pi R^2}\int_{E_0=\epsilon}^{\infty} F_{e^-}(E_0)\,\sigma(\epsilon, E_0)dE_0 \tag{1.7}$$

For the uniform source electrons that follow single power-law distribution: $F_{e^-}(E) \propto E^{-\delta}$, the resulting photon spectrum takes the form of $I(\epsilon) \propto \epsilon^{-\gamma}$. An important observational difference between the thick-target model and the thin-target model is that $\gamma_{thick} = \delta - 1.5$ while $\gamma_{thin} = \delta + 0.5$ [108]. The spectrum of footpoint HXR sources is usually fitted with a thick-target bremsstrahlung model because they are due to nonthermal electrons bombarding against the dense chromosphere and losing most of their energy [25]. The fitting results usually suggest that a large number of electrons are accelerated to nonthermal energies and arrive at the footpoints of the coronal loops.

Compared to chromospheric HXR emission, the coronal HXR emission during the impulsive phase is believed to be more intimately related to flare energy release (see more detailed discussions in Krucker et al. [138]). In certain events, an HXR source is found to be located above the looptop of the flare arcade (as shown in Figure 1.4). The source is referred to as the "above-the-loop-top" (ALT) source or the "Masuda" source after S. Masuda who made the first discovery [174], followed by multiple, but rather infrequent reports, e.g.[232, 140, 84]. The spectral analysis reveals a compact nonthermal electron population, centered at $\lessapprox 7000\ km$ above the thermal coronal looptop, with the maximum flux falls into the range of 30–50 keV, likely emitting X-rays according to the thin-target regime owing to the relative small plasma density in the coronal source [174]. The intensity of the source also follows a similar time evolution as the footpoint sources [174]. However, the spectrum of

the nonthermal electron from the "Masuda source" is usually softer than that of footpoint sources [138]. This is because while the footpoint source is due to thick-target bremsstrahlung, the coronal HXR source is usually produced in the thin-target regime. With the assumption of the same nonthermal electron population, a difference of $\gamma_{thin} - \gamma_{thick} = 2$ is expected. However, although γ_{thick} is almost always smaller than γ_{thin}, the difference between them does not always match the theoretical expectation [15]. It is suggested that the "thickness" of the target may vary with the energy of the electron. In addition, transport effects from the corona to the footpoints may also play a significant role [16, 238].

The temporal relation between the SXR and HXR flux usually exhibits the so-called "Neupert Effect" [191], named after the author who first discovered that the derivative of the SXR flux at 1.87 Å has a good correlation with the microwave radio flux. The Neupert Effect usually refers to the correlation between the derivative of the SXR flux and the HXR flux, i.e., $dF_{sxr}(t)/dt \propto F_{hxr}(t)$, because the latter is highly sensitive to the nonthermal electron population that also produces the microwave radio emission during the solar flare. The Neupert effect has been observed in many flare events. As the nonthermal electrons are thermalized at footpoints in the dense chromosphere, the local plasma is heated and therefore is driven into the flare loop by the enhanced pressure. The process is termed "chromospheric evaporation" [170], resulting in bright post-flare loops observed in EUV and SXR wavelengths and bright or dark loops in $H\alpha$ observation [161, 261]. Although there are observations inconsistent with the Neupert Effect [237], which may suggest energy transport mechanisms other than downward propagating energized electrons [74], the widely accepted explanation of the Neupert Effect is: The SXR-emitting plasma is mainly heated by the accelerated electrons, which are responsible for HXR emission.

The multi-wavelength observations, exemplified by the X-ray observation described above (the same perspective from EUV, UV, visible, and radio observation

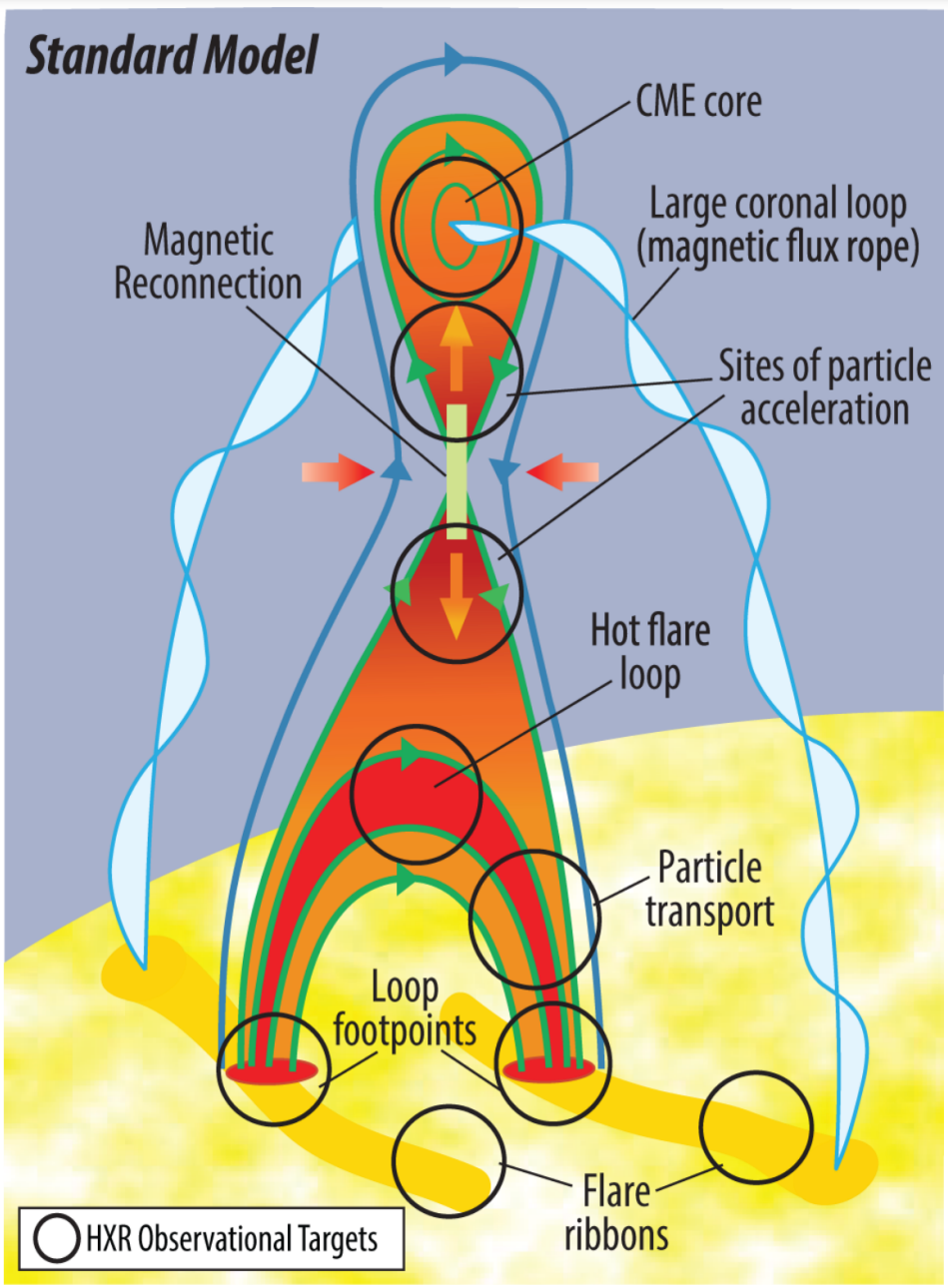

Figure 1.5 Schematic representation of the standard flare model that shows and explains the main observable features.
(Source: [50])

will be mentioned or described in detail in the following sections), form the basis of the "Standard Flare Model." The model is also referred to as the "CSHKP model" [31, 224, 107, 135]. A number of widely observed and modeled physical processes have been progressively attached to the model. As shown in the sketch of the standard flare model (Figure 1.5), the energy release process during the solar flare is due to the magnetic reconnection[258]. The magnetic reconnection occurs within a thin, vertical region in the corona above the flare loops, named the current sheet (green box in Figure 1.5). During the reconnection, the field lines at the two opposite sides of the current sheet approach each other (red arrows in Figure 1.5). The field lines break and reconnect, changing the magnetic topology in the corona rapidly and releasing the energy in the forms of Poynting flux, enthalpy flux, bulk kinetic flux, and accelerated particles [199]. The energy fraction of each component is, however, not well understood [22]. One of the most important forms of energy relevant to this dissertation is energetic particles. Although there is ongoing debate about the dominating acceleration mechanism(s) and acceleration site [62, 262, 66, 110, 200, 53], it is well accepted that most of the electrons should be accelerated in the vicinity of the reconnection region.

The standard flare model still needs to be tailored to the realistic topology of flares and improved. Observations of solar flares that deviate from the CSHKP model are common. Take "Veronig-Brown flare" [238] for example, a coronal thick target loop is observed instead of the thick target chromospheric footpoint source (also be seen in Veronig et al. [237]) or the thin target coronal ALT source. The two studied event is revealed to have loop column densities that are consistent with nonthermal thick-target HXR emission from electron with $E_{e^-} \gtrapprox 50\ keV$. About 50% of hard X-ray events show a deviation from the Neupert effect pattern in the timing of soft and hard X-ray emissions [57, 177, 237]. Alternative models that do not attribute SXR emission exclusively to energization of the nonthermal electrons are proposed

[1, 57]. A model [74] that allows the energy released in magnetic reconnection to be transported through the corona to the lower atmosphere via large-scale Alfvén wave is proposed to avoid the problems with the beam model [58, 142, 173] and to address the "number problem" [76, 140].

In addition, the original CSHKP standard flare model is a two-dimensional model. However, three-dimensional features are frequently reported and discussed [**?** 9, 122]. The motion of the footpoint source in HXR [75] and EUV [33, 205] along the ribbon is observed. More importantly, the shear of the flare arcade with respect to the polarity inversion line (PIL) is frequently observed, which appears to decrease as the flare evolves [205], indicating a decreasing guide field component, the magnetic field component along the third dimension. It has been proposed that the guide field plays an important role in the magnetic reconnection [201] and particle acceleration processes [62, 52, 7].

The energy release processes that are discussed in this section so far mainly focus on the area below the reconnection region from the perspective of X-ray observations. As shown in Figure 1.5, a magnetic flux rope (MFR) which is above the reconnection region, is critical in driving the flare evolution and energy release. The MFR will be discussed in detail in Section 1.2. As an important diagnostic tool for flare energy release and coronal magnetometry, and as the core observation of the thesis, radio diagnostics in solar flares will be introduced in Section 1.3.

1.2 Magnetic Flux Rope in Solar Flares

1.2.1 MFRs, CMEs and solar flares

As discussed in Ssubsection 1.1.2, the standard flare model features an outward-going (erupting) MFR which is defined as a magnetic structure in which field lines wrap around an axial magnetic field line. Depending on whether there is a successful MFR eruption, the flares can be categorized as confined events [234, 100] (the MFR fails to erupt), partially eruptive events [162, 134] (only a part of the MFR erupt),

and eruptive events. Eruptive events, and some partial eruptive events, are often associated with coronal mass ejections (CMEs).

CMEs are large magnetic structures that carry plasma and are expelled from the solar atmosphere into the interplanetary space [248]. The correlation between the CMEs and solar flares has been comprehensively studied. On one hand, 60% of the large flares [2] ($\geq$ M Class), and 90% of X class flares [246] are associated with CMEs, the rest of the 10% are suggested to be confined by the overlying arcade field [246]. On the other hand, if only the earth-directed CMEs are considered, in which the associated flare is potentially observable, 88% of the CMEs are associated with solar flares, and 80% of the CMEs origins inside the active regions [266]. The asymmetry of the two association rates cannot be simply attributed to the causality of the two phenomena (see detailed discussions in Webb and Howard [249]).

Although there is no one-to-one correlation between CMEs and solar flares, the strong correlation between the two phenomena led to various hypotheses about their causality: (I) Solar flares cause CMEs, e.g. [63, 175]. (II) Solar flares are the byproducts of CMEs [126]. (III) When a solar flare has an associated CME, they are both part of an underlying magnetic process [106, 263, 249]. The increasing presence of observations showing the detailed correlation between the kinematic evolution of the CMEs and the released energy of the solar flares favors the third hypothesis. The involved models are summarized and reviewed in Forbes et al [77].

1.2.2 Observation of magnetic flux ropes

MFRs have a wide distribution of size. They can grow into 10^4–10^5 Mm in the interplanetary space [249]. On the other hand, in coronal jets, the mini-MFRs are only 10^3–10^4 km in size [222]. MFRs are believed to be the core structure of the eruptions (successful or failed) during solar flares, especially in CME-associated events. In white-light coronagraphs, CMEs usually display a three-part structure [118, 42, 241].

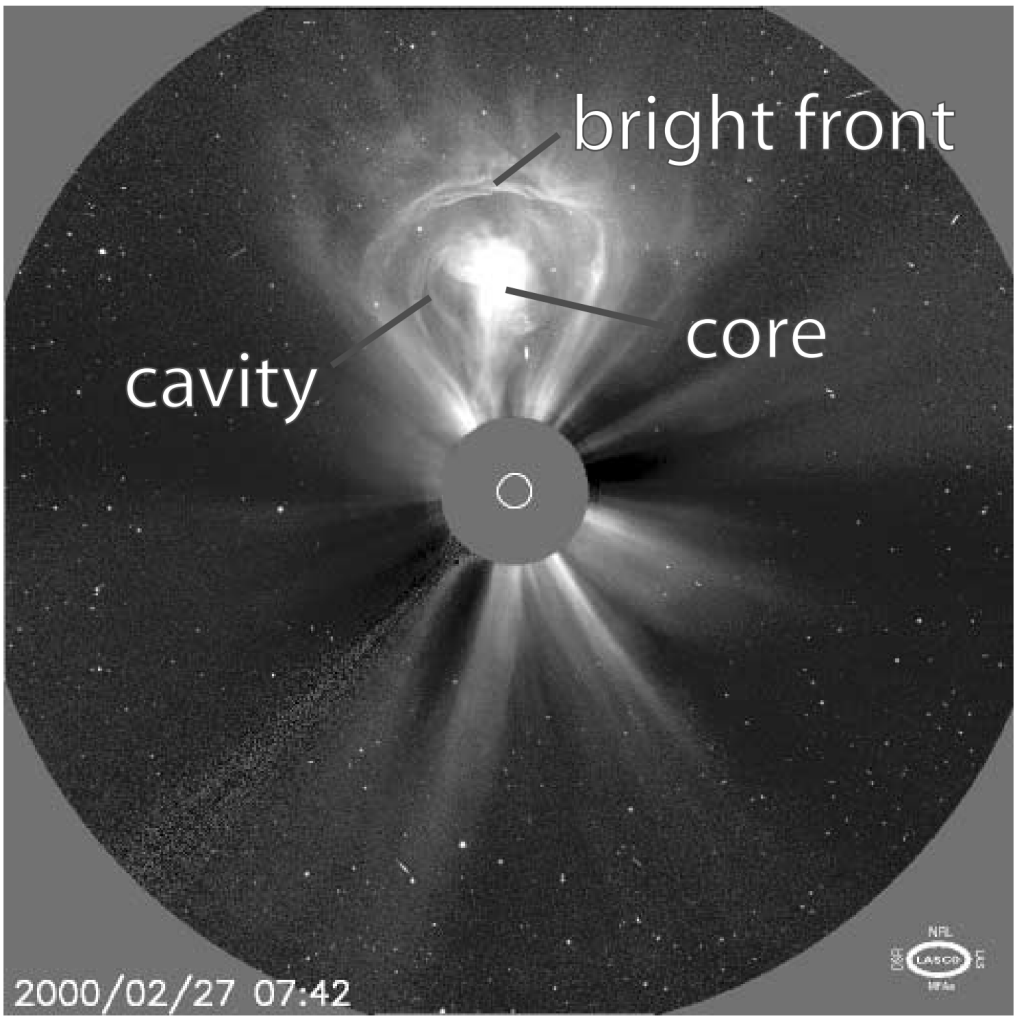

Figure 1.6 A typical three-part CME observed in white-light, the three parts are annotated.
Source: [211]

From outside to the inside, they are a bright leading edge, a dark cavity, and a bright core, as shown in Figure 1.6. The dark cavity is typically attributed to a low density volume wrapped by MFR [169]. The bright leading edge is interpreted as the accumulated plasma at the front of the rising MFR [255, 216]. There is some controversy about the interpretation of the bright core. It is used to be widely regarded as the filament/prominence [118], which is the dense plasma supported at the bottom of the MFR. However, recent observations suggest the bright core can be the MFR itself without the need of a filament/prominence [112, 239, 219].

Magnetic flux ropes are essentially magnetic field structures. Although the vector magnetic field has been measured within the CMEs in the interplanetary space, named "ICME", by in-situ observation (e.g. [44]), the observation of the MFRs in the solar atmosphere still relies on the associated observable features and magnetic field extrapolations. Filaments are relatively cool (10^4 K) and dense (10^{11}–10^{12} cm^{-3}) plasma "floating" in the hot and attenuated corona [160]. When observed on the solar disk, filaments are dark features against the bright solar disk in chromospheric lines such as $H\alpha$ and EUV due to the strong absorption and weak emission in these passbands. However, when the phenomena are observed above the solar limb (termed as "prominence"), the plasma appears bright in the chromospheric lines against the coronal background (Figure 1.7). Filaments are one of the primary indicator of the MFRs [90, 28, 164, 150]. The dense plasma of the filament is supported by the magnetic dip at the bottom of the MFR [144] which also isolates the filament from the hot corona. Other models, such as filaments supported by the sheared-arcades [5], are reviewed with detail in Gibson [90], Liu [160].

As possible CME precursors [115, 89], sigmoids are regarded as another excellent indicator of MFRs. Sigmoids are usually observed as bright S-shaped coronal structures in SXR and EUV. The sigmoids are usually described as the plasma heated by a curved current sheet (CS) between the MFR and the surrounding field [132, 88].

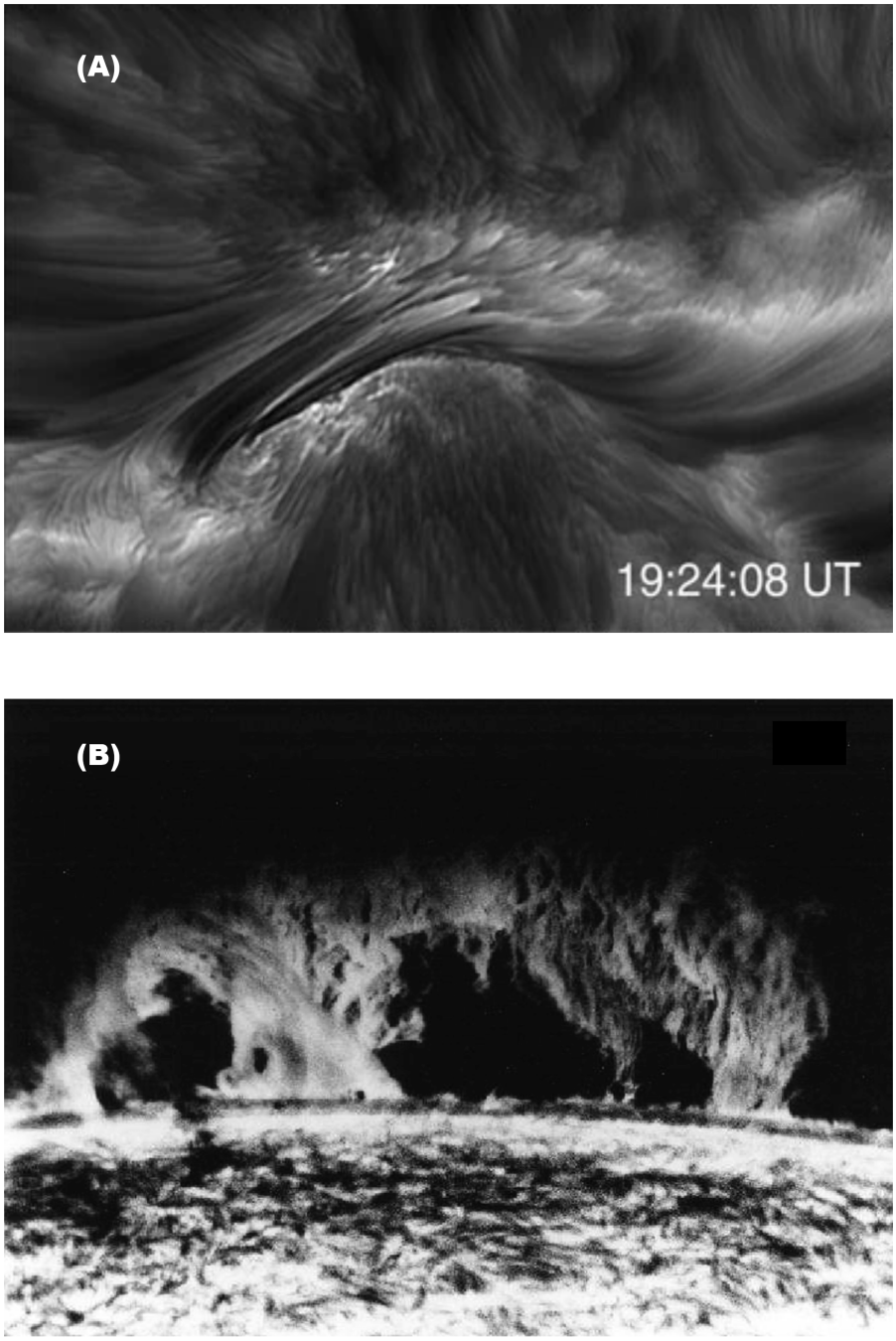

Figure 1.7 **A** Filament observed by BBSO/GST VIS images at the $H\alpha$ line center, the image is taken from NOAA Active Region 11817 on Aug 11, 2013 (from [243]). **B** A small quiescent prominence observed by BBSO in $H\alpha$ from 1970.
Source: BBSO image gallery https://www.bbso.njit.edu/images.html, Retrieved on Apr 1, 2023

Although the magnetic structure of the MFR is not directly observable, the helicity sign can be inferred from the evolution of the sigmoid during its eruption. The helicity sign is found to be consistent with that inferred from the features of the associated filament [97]. In some events, the S-shaped emissions are found to evolve from two J-shaped emissions, which show up before the eruption [96]. The observation is consistent with a model in which the MFRs, characterized by the S-shape bright structure, is formed by "flux-cancellation" or "tether-cutting" reconnection between the sheared arcades, characterized by the two J-shaped bright structures [98].

In some recent events, "hot channel" is found to be a more direct observable feature of the MFR [264, 192], the hot channel is evolved from a sigmoid appears earlier [264]. The hot channels are usually observed in EUV observation which is sensitive to plasma at a temperature of $\gtrapprox 8$ MK [46, 264]. There are plentiful common features that are shared by the observed hot channel and the modeled MFR (see discussion in Song et al. [217]). In addition, both the morphology and the height evolution of the hot channel in EUV are found to be consistent with the cavity or bright core in white-light CMEs [264, 47]. The evolution of the hot channel is shown in Figure 1.8 [264].

1.2.3 Magnetic topology of MFRs

helical magnetic field lines wind around the central axis in the same direction and share similar magnetic connectivity. Compared to the ambient field lines, the field lines in MFRs feature similar magnetic connectivity and helicity [88]. The two parameters which are widely used [8, 122, 120, 166] to describe the magnetic connectivity and helicity of the field lines are the "squashing factor" [231] and the magnetic twist number [20].

When applied to the solar magnetic field, the squashing factor usually measures the gradients in the mapping of a field with respect to its footpoints, which is powerful

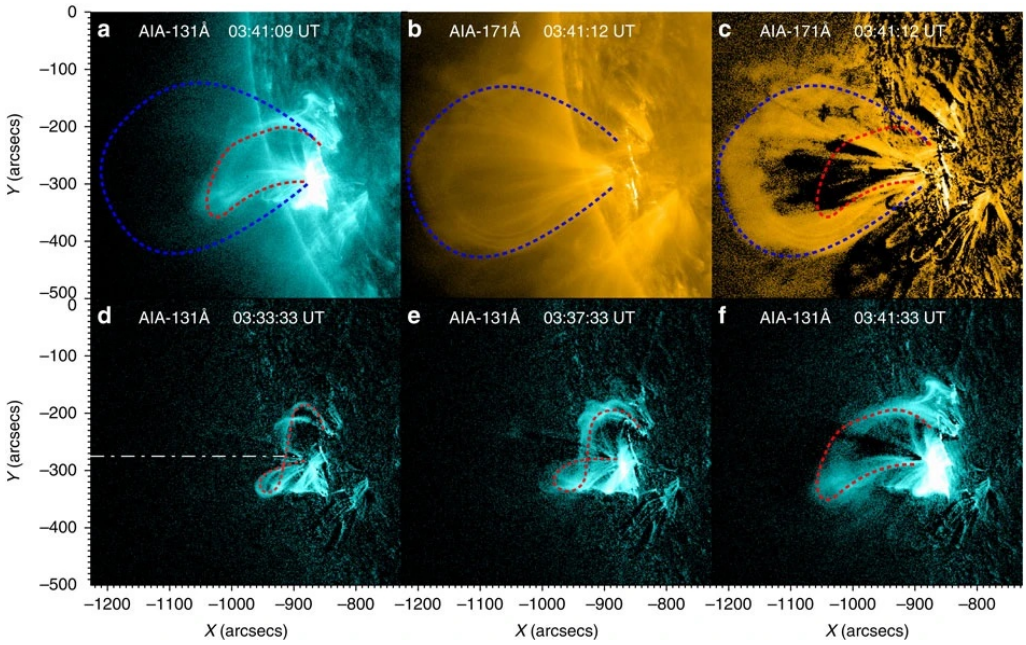

Figure 1.8 The evolution an observed hot channel in SDO/AIA 131 Å(red dashed lines). While the blue dotted line indicates the cool compression front.
Source: [264]

in identifying magnetic field in different magnetic domains. The squashing factor is defined as [231, 160]:

$$\mathrm{Q} \equiv \frac{\mathrm{a}^2 + \mathrm{b}^2 + \mathrm{c}^2 + \mathrm{d}^2}{\mid \mathrm{B_{n,1}}\left(\mathrm{x_1}, \mathrm{y_1}\right) / \mathrm{B_{n,2}}\left(\mathrm{x_2}, \mathrm{y_2}\right) \mid}, \tag{1.8}$$

where a, b, c, and d are derived from the Jacobian matrix associated with the mapping:

$$\mathrm{D_{12}} = \left[\frac{\partial \mathbf{r}_2}{\partial \mathbf{r}_1}\right] = \begin{pmatrix} \partial \mathrm{x_2}/\partial \mathrm{x_1} & \partial \mathrm{x_2}/\partial \mathrm{y_1} \\ \partial \mathrm{y_2}/\partial \mathrm{x_1} & \partial \mathrm{y_2}/\partial \mathrm{y_1} \end{pmatrix} \equiv \begin{pmatrix} \mathrm{a} & \mathrm{b} \\ \mathrm{c} & \mathrm{d} \end{pmatrix}, \tag{1.9}$$

and $\mathrm{B_{n,1}}\left(\mathrm{x_1}, \mathrm{y_1}\right)$ and $\mathrm{B_{n,2}}\left(\mathrm{x_2}, \mathrm{y_2}\right)$ are the normal components of the magnetic field at the footpoints (photosphere). With the definition of the squashing factor, the quasi-separatrix layers (QSLs) [197] is defined as a layer with steep gradients in magnetic connectivity (squashing factor). Therefore, the MFR usually has a boundary in the form of a QSL [197]. The QSL is also commonly used as an indicator of

magnetic reconnection. In three-dimensional reconnection models, e.g., [198], the self-intersecting QSL forms a hyperbolic flux tube (HFT) [231]. The null point in the HFT is believed to be the reconnection site, whose 2D counterpart is shown as the reconnecting "X-point" in Figure 1.5. For the MFR at a relatively low height, the QSLs could be in the form of bald-patch-separatrix surfaces (BPSS)[230]. As shown in Figure 1.9, the dips of the purple field lines, termed BPSS, graze the photosphere. The heating due to reconnection occurring at the sigmoidal BPSS is consistent with the observed sigmoid in morphology [88, 96].

The number of turns that a magnetic field winds about the axis can be measured by the magnetic twist number $\mathcal{T}_g$ [20], which can be well approximated by [20]:

$$\mathcal{T}_w = \frac{\mu_0}{4\pi} \int_L \frac{\mathbf{J} \cdot \mathbf{B}}{B^2} dl, \tag{1.10}$$

where $\mathbf{J} = \nabla \cdot \mathbf{B}/\mu_0$, is the induced current of $\mathbf{B}$, whose component that is parallel to $\mathbf{B}$, $J_\parallel = \mathbf{J} \cdot \mathbf{B}/|\mathbf{B}|$, then:

$$\frac{\mathrm{d}\mathcal{T}_w}{\mathrm{d}s} = \frac{\mu_0 J_\parallel}{4\pi |\mathbf{B}|} \tag{1.11}$$

As mentioned in Section 1.2, the total magnetic energy of the MFR can also be classified into potential and free magnetic energy, which can also be written in the following form [212]:

$$E_m = \int_V \frac{B^2}{8\pi} dV = \frac{1}{8\pi} \int_V B_p^2 dV + \frac{1}{2c} \int_V \mathbf{A}_c \cdot \mathbf{J} dV, \tag{1.12}$$

where $\mathbf{B}_p$ is the potential component of the magnetic field and $\mathbf{A}_c$ is the magnetic vector potential of the non-potential component of the magnetic field. As shown in Equation (1.12), the magnetic field of MFR is crucial to understanding the energy release processes, which will be discussed in Chapter 2.

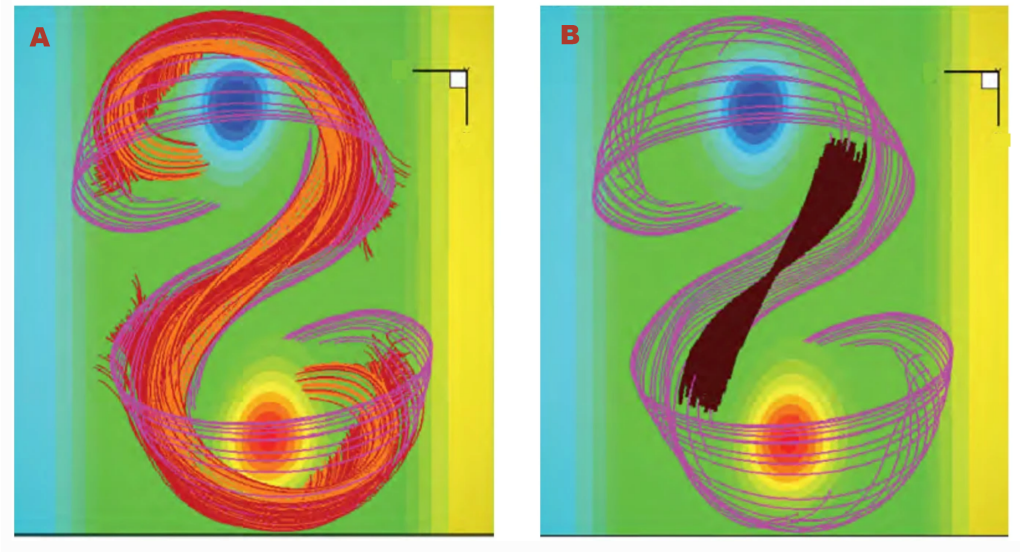

Figure 1.9 Simulated magnetic topology of the MFR in a dipole configuration. **A** The BPSS is shown as the purple field lines. The current-sheet-intersecting field lines are drawn in red/orange. **B** Filament (dark brown lines) are supported by the dipped field lines.
Source: [90]

As the key question about the role that the MFRs play in solar eruptions, the relationship between the MHD instability of MFR and eruption initiation or the debate on whether MFR existed before the flare will not be discussed in detail in this dissertation; we refer interested readers are to other works [88, 249, 90, 160], where the topics are discussed more thoroughly.

1.3 Microwave Emission in Solar Flares

The radio band is the widest window of observations from the ground in the entire electromagnetic spectrum. Although restricted by the absorption and the reflection of the atmosphere and the ionosphere of the earth at low frequencies ($\lesssim$20 MHz), the available ground-based radio window ranges from a few MHz to a few hundred GHz. Solar radio observations provide many unique diagnostics for understanding the physics of solar flares. The section will start with general concepts in solar radio and then focus on the microwave band (cm-λ) analysis in solar flares.

1.3.1 Basic conceptions

The radio flux measured within a certain frequency range ν–$\nu + d\nu$ and a given solid angle $d\Omega$ is called "specific intensity," defined as:

$$I_\nu = \frac{dE_\nu}{dt(d\sigma cos\theta)d\nu d\Omega}, \tag{1.13}$$

where E_ν is the energy receieved, I_ν is in unit of J m^{-2} Hz^{-1} s^{-1} sr^{-1}. ν, σ, θ, Ω, are the frequency of the emission in Hz, the surface area of the source in m^2, inter angle between the observing surface normal and the line from the source to the observer in radian, the solid angle of the source in radian, respectively. Integrating the specific intensity over the solid angle and then applying the "small source approximation" ($cos\theta \approx 1$), another commonly used measurement of a radio source, flux density, can be defined as:

$$S_\nu = \frac{dE_\nu}{dtd\sigma d\nu} = \int_{4\pi} I_\nu \cos\theta d\Omega \approx \int_{4\pi} I_\nu d\Omega. \tag{1.14}$$

The flux density is usually expressed in Jansky (Jy; 1 Jy = 10^{-22} W m^{-2} Hz^{-1}). In solar radio astronomy, the solar flux unit (sfu) is also commonly used (1 sfu = 10000 Jy).

Consider radiation at a monochromatic intensity of I_ν, passes vertically through a medium that only absorbs and does not emit at the current frequency with a thickness of dl, the change in intensity is $-dI_\nu$. In a uniform distributed medium, the amount of change is proportional to the thickness of the medium, which can be written into:

$$-dI_\nu = \kappa_\nu I_\nu dl \tag{1.15}$$

In Equation (1.15), κ_ν is the absorption coefficient, in units of cm^{-1}. With the definition of absorption coefficient, the optical depth can be defined as:

$$\tau_\nu = \int_L \kappa_\nu dl \tag{1.16}$$

The optical depth, which is dimensionless, can be used to conveniently describe the intensity reduction of emission between the source and the observer: $I_\nu = I_{\nu 0} e^{-\tau_\nu}$.

Similarly to the absorption coefficient, when it comes to the capability of radiation of the medium at the current frequency, the emissivity η_ν, in units of erg cm^{-3} s^{-1} Hz^{-1} sr^{-1}, can be written into:

$$\eta_\nu = \frac{dE_\nu}{dV dt d\nu d\Omega} \tag{1.17}$$

In some specific cases, absorption coefficient and emissivity are related. In local thermodynamic equilibrium (LTE), the absorption coefficient and emissivity follow the Kirchoff's law:

$$\eta_\nu = \kappa_\nu B_\nu(T) \tag{1.18}$$

$B_\nu(T)$ is the Planck function. In the radio regime ($h\nu \ll kT$), the Plank function follows the Rayleigh-Jeans approximation:

$$B_\nu(T) = \frac{2\nu^2 k_B T}{c^2}, \tag{1.19}$$

where k_B is the Boltzmann constant and c is the speed of light. Following the definition in black body radiation, a "brightness temperature" T_b can be defined as the temperature that a black body would need to have to emit the same observed brightness.

With the definition of brightness temperature under the Rayleigh-Jeans limit ($h\nu \ll kT$), Equation (1.19) can be rewritten as the "Rayleigh-Jeans" equation to

describe the relationship between observed flux density and brightness temperature:

$$S_\nu = \frac{2\nu^2 k_B}{c^2} \int_\Omega T_b d\Omega \tag{1.20}$$

1.3.2 Radio emission mechanisms

The solar radio emission is dominated by the electrons interacting with the local plasma, magnetic field, etc. [11, 80]. Solar radio imaging spectroscopy and the well-modeled emission mechanisms provide not only the tools for probing the thermal/nonthermal electrons but also diagnosis of the environmental plasma parameters. Figure 1.10 schematically shows the relationship between height above

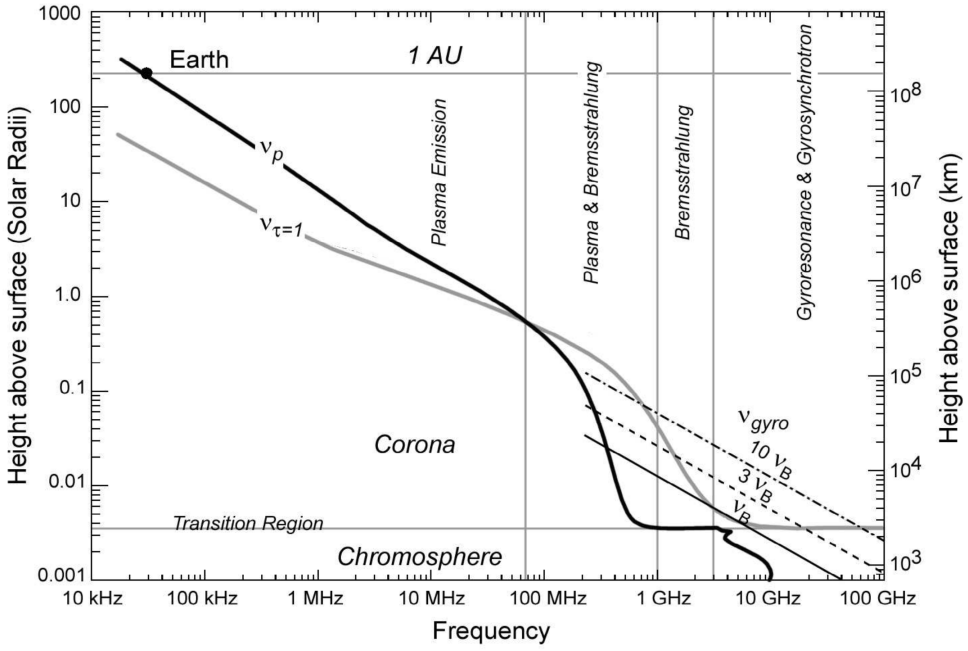

Figure 1.10 Diagram illustrating the relationship between height above the solar surface and characteristic radio frequencies of each usual radio emission mechanism. The mechanism in the upper right of the diagram is dominating at a certain frequency/height. The model of temperature, density, and magnetic field can be found in Gary and Keller [80]
Source: Gary and Keller [80]

the solar surface and characteristic radio frequencies of each usual radio emission mechanism. There are two essential frequencies in Figure 1.10, ν_p and ν_{gyro},

representing the plasma frequency and the electron gyrofrequency, respectively. The involved emission mechanisms will be elaborated on in the following part of this section. Solar bursts exhibit a vast range of emission mechanisms, competing for dominance across various frequencies. However, the apparent complexity of these bursts can be comprehended by considering ν_p and ν_{gyro} [80].

Coherent emission Coherent emission, also termed as "collective plasma radiation processes" [179], refers to the emission in which the electrons move in a highly coordinated fashion (in phase) due to the particle-wave and wave-wave interaction, so that the emission is in phase as well. As a result, the coherent emission usually features a high brightness temperature.

Plasma radiation is one type of the coherent emissions, which features emission at a frequency that is near the fundamental or second harmonic of the plasma frequency

$$\nu_p = \sqrt{\frac{n_e e^2}{\pi m_e}} \approx 8980\sqrt{n_e} \tag{1.21}$$

The overall conception of the theory for plasma radiation remains more or less the same since it was first proposed [93]. Three stages are usually involved:

- Langmuir wave is caused by a micro-instability termed "bump-on-tail" instability, which is caused by multi-peaked electron velocity distribution.
- The fundamental emission and (or) backward-propagating Langmuir waves are generated through the scattering of Langmuir waves on ion acoustic waves or density structures.
- Emission at second harmonic plasma frequency ($\nu = 2\nu_p$) results from the nonlinear wave–wave coalescence to yield the harmonic emission.

Here we refer the readers to Dulk [65], Melrose [180], and the references therein for a more comprehensive discussion of the theory for plasma radiation. Because of

its sensitivity to the local plasma density, plasma emission is often used to diagnose the bulky motion of plasma and electrons. The corresponding measurement can be identified as various features in the observed dynamic spectra in a wide frequency range of a few kilo-Hertz (kHz) to $\approx$ 1 GHz (Figure 1.11). The features are summarized as solar radio bursts in various types [65]. As shown in Figure 1.11, Type II and type III radio bursts are believed to originate from plasma radiation. Readers are referred to Gary and Keller [80] for more details about diagnosis with solar radio bursts due to plasma radiation.

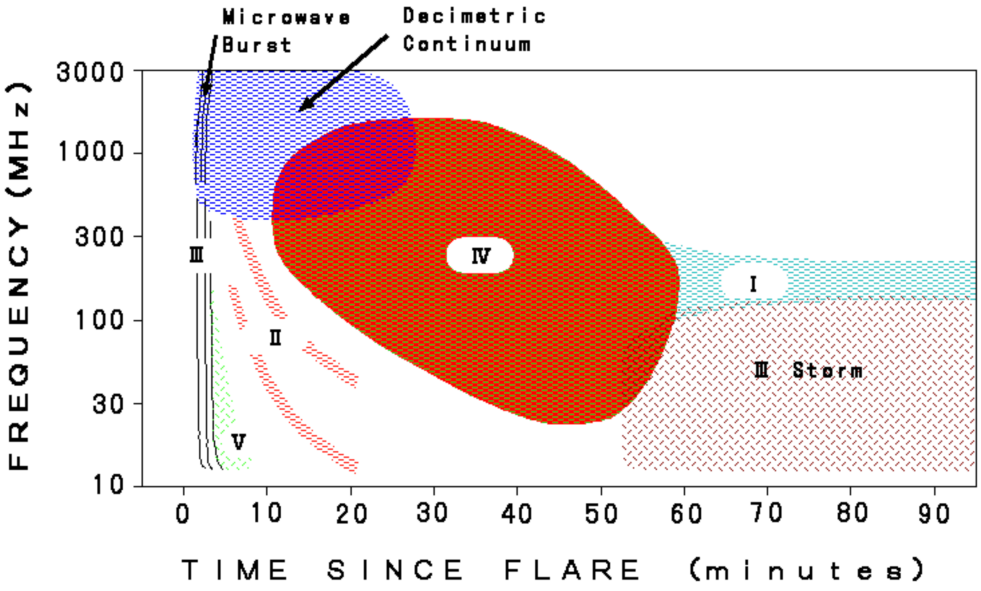

Figure 1.11 Diagram illustrating the typical features of Solar Radio Bursts.
Source: HiRAS Solar Observatory

Incoherent emission In the microwave domain is usually dominated by bremsstrahlung, gyroresonance, and gyrosynchrontron radiation. All three mechanisms are categoried as incoherent radio emission. Compared to coherent emission, the electrons are not emitting in phase; in other words, the radiation process from the electrons is independent of each other.

Bremstrahlung As mentioned in Subsection 1.1.2, bremsstrahlung refers to the radiation produced by Coulomb collisions between electrons and ions in the highly ionized plasma. Shown as the gray curve in Figure 1.10, $\nu_{\tau=1}$ at higher frequency shows up at a smaller assumed height (larger number density). The curve can be explained by the absorption coefficient of thermal bremsstrahlung [65]:

$$\kappa_\nu \approx 9.78 \times 10^{-3} \frac{n_e}{\nu^2 T^{3/2}} \sum_i Z_i^2 n_i \times \begin{cases} 18.2 + \ln T^{3/2} - \ln \nu & (T < 2 \times 10^5 \text{ K}) \\ 24.5 + \ln T - \ln \nu & (T > 2 \times 10^5 \text{ K}) \end{cases} \tag{1.22}$$

In Equation (1.22), n_e, T, ν, Z_i, and n_i are electron number density, electron temperature, observing frequency, ion charge, and ion number density. As a great example of combining the concept of radiative transfer equation, brightness temperature, and optical depth, the observed brightness temperature can be substituted into the radiative transfer equation:

$$T_b = T_{chr} e^{-\tau_{cor}} + T_{cor} \left(1 - e^{-\tau_{cor}}\right) \tag{1.23}$$

Where T_{chr} and T_{cor} are the electron temperatures of the chromosphere and corona, respectively. τ_{cor} is the optical depth of the corona. The solid curve in Figure 1.12 shows a brightness temperature spectrum for thermal bremsstrahlung from a 10^6 K corona and a 10^4 K chromosphere as the background. By comparing it to the dashed curve (the spectrum for the coronal contribution alone), we can see how background chromosphere plays a role in the observed brightness temperature spectrum. The optical depth of thermal bremsstrahlung, as shown in Equation (1.22) and Equation (1.16), is sensitive to the electron temperature, the electron number density, and the integrated length along the line-of-sight. The arrows in Figure 1.12 show how the growth of the above three parameters would change the shape of the thermal bremsstrahlung spectrum. Deriving the parameters

from the observed spectrum as shown in this example, termed "spectral diagnostic," is a critical technique used in this dissertation for interpreting the EOVSA microwave observations.

Gyroresonance and gyrosynchrontron emission Gyroemission, also known as "magneto-bremsstrahlung," originates from the centripetal acceleration of electrons as they move around a magnetic field. The gyro-emission from tnon-relativistic electrons is known as "cyclotron emission," in which the electrons gyrate at a fixed frequency (gyro-frequency) that only depends on the magnetic field strength:

$$\nu_b = \frac{eB}{m_e \pi c} = 2.8 \times 10^6 B \text{ Hz} \tag{1.24}$$

When the electrons are in temperature ($\sim 10^5$–10^6 K) that the relativistic effect can not be neglected, the sinusoidal dipole pattern due to symmetric circular motion in cyclotron emission will be changed then results in emission at harmonics of the gyro-frequency:

$$\nu_{gyroresonance} = s \times 2.8 \times 10^6 B \text{ Hz (s=1,2,3...)} \tag{1.25}$$

The gyroresonance emission dominates the region that features a strong magnetic field ($\gtrapprox$ 100 G, e.g., the corona above the sunspot where the temperature is also satisfied). Because the emission frequency of the gyroresonance emission is discrete and occurs at harmonics of the gyrofrequency, the emission provides diagnostics on the **absolute** magnetic field strength B. The readers are referred to Chapters (4) and (5) in Gary and Keller [80] for details about emission mechanisms, diagnosis, and examples of diagnosis with actual observations.

As mentioned in the previous section, electrons can be accelerated during an explosive event like a solar flare. When the electrons are in the mildly-relativistic regime ($\sim 10^2$–10^3 keV), the emission pattern becomes more asymmetric angularly,

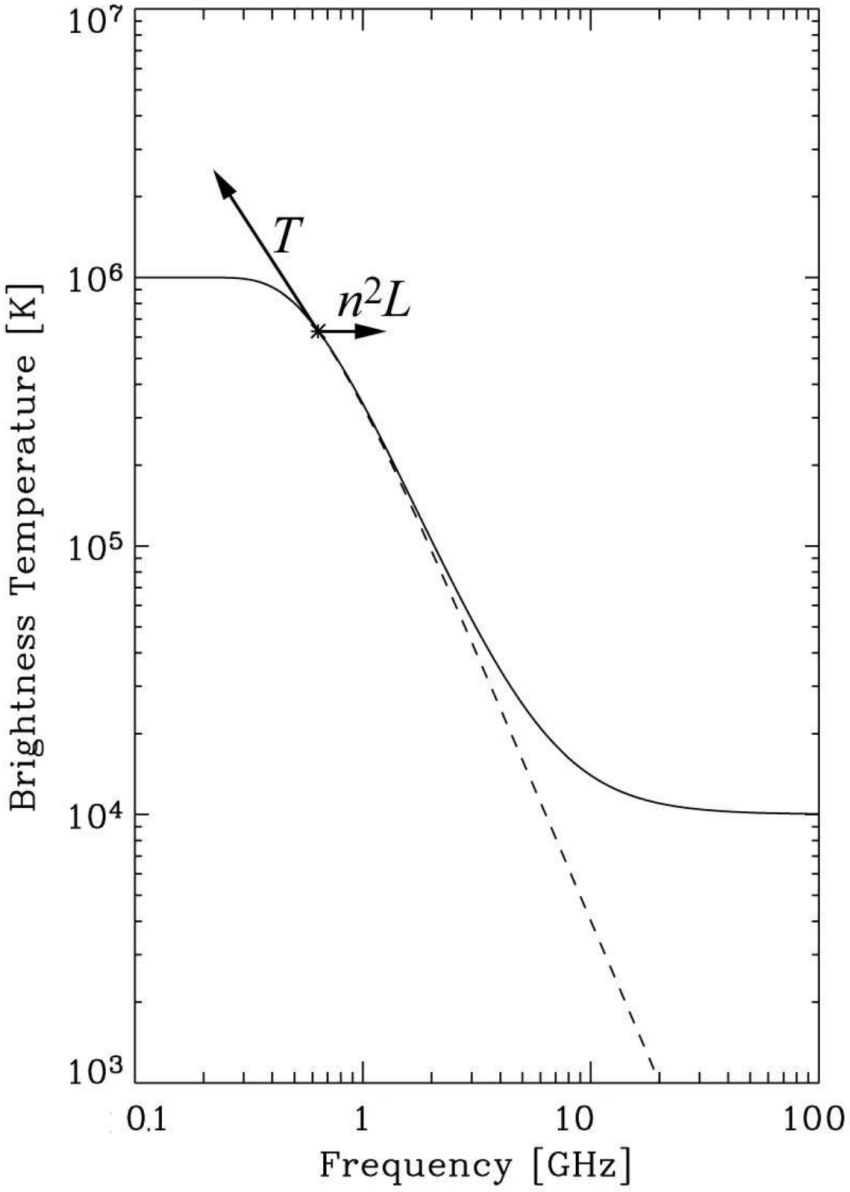

Figure 1.12 Brightness temperature spectrum for thermal bremsstrahlung from a 10^6 K corona and a 10^4 K chromosphere (solid line). The spectrum without the cooler chromosphere as the background is shown as the dashed line.
Source: [80]

and the emission peaks at harmonics of 10–100. Meanwhile, the thermal broadening of the line is more serious. As a result, the harmonics are smeared out and can be approximated as a continuum emission, known as gyrosynchrontron emission, which dominates the microwave emission during flares. The theoretical expressions of the gyrosynchrotron emissivity and absorption coefficient are shown in Ramaty [207]. The complexity of the theoretical expressions makes numerical solutions a commonly used method to calculate the gyrosychrotron spectra. Nevertheless, even for modern computing resources, the exact numerical solution is still too computationally intensive. One of the approaches is fitting the empirical expressions to the numerical results. Dulk [65] shows the simplified empirical expressions for T_{eff}, η_ν and κ_ν with constraining on power-law index of the nonthermal electron distribution δ, viewing angle θ, and harmonic:

$$T_{eff} \approx 2.2 \times 10^9 10^{-0.31\delta} (\sin\theta)^{-0.36-0.06\delta} s^{0.05+0.085\delta} \tag{1.26}$$

$$\frac{\eta_\nu}{BN} \approx 3.3 \times 10^{-24} 10^{-0.52\delta} (\sin\theta)^{-0.43+0.65\delta} s^{1.22-0.90\delta} \tag{1.27}$$

$$\frac{\kappa_\nu B}{N} \approx 1.4 \times 10^{-9} 10^{-0.22\delta} (\sin\theta)^{-0.09+0.72\delta} s^{-1.30-0.98\delta} \tag{1.28}$$

The fast gyrosynchrotron codes developed by [71] (and their recently updated version [146]) is a more accurate approach to calculate the gyrosynchrotron spectra (compared to the approximations above) while also reduces the computation time by several orders of magnitude (compared to using the exact formula). The method is adopted to calculate the gyrosynchrotron emission throughout this dissertation.

Figure1.13 is a typical brightness temperature spectra for gyrosynchrotron emission from power-low distributed homogeneous nonthermal source. The spectra reach its peak value at "turn over frequency" ν_{to}, where the optical depth $\tau \approx 1$. The optical thick and optical thin regimes are on the left and right sides of the

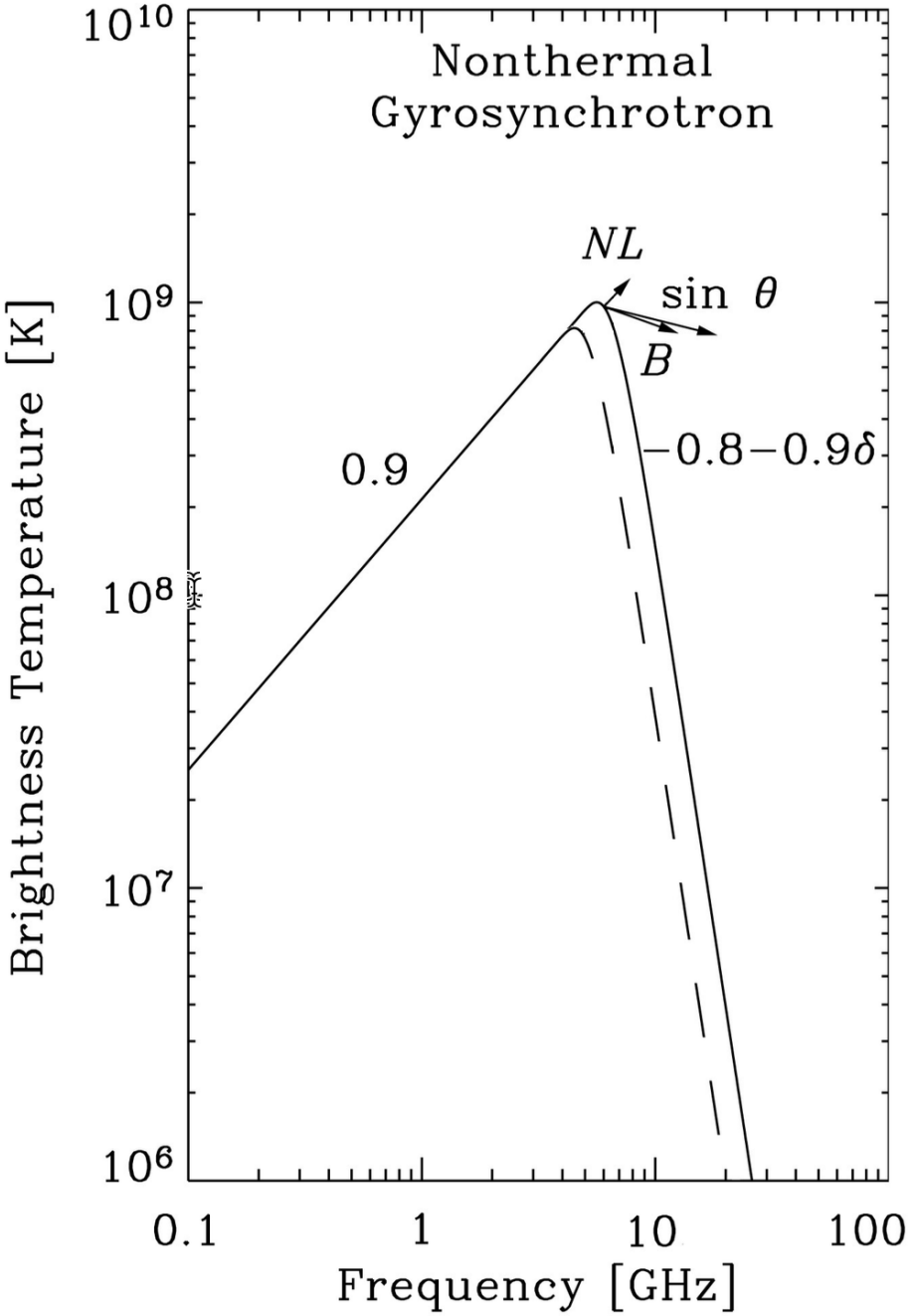

Figure 1.13 Brightness temperature spectra for a typical gyrosynchrotron emission from power-low distributed nonthermal electron. The direction and the length of the arrows indicate how does quadruple the annotated parameters would change the spectra. The solid line shows the "x-mode" spectra while the dashed line shows the "o-mode" spectra.
Source: Gary and Keller [80]

ν_{to}, respectively. On the optical thick side, the brightness temperature at higher frequency attributes to electrons with higher effective temperature, giving rise to a higher brightness temperature. Therefore, this part of the spectra features a positive slope. In Figure 1.13, the direction and the length of the arrows indicate how does quadruple the annotated parameters would change the spectra. N and L are the number density of the nonthermal electron and column depth, respectively. Increasing the total amount of the nonthermal electron would simply increase the ν_{to}. On the other hand, the higher magnetic field strength is equivalent to a higher base gyro-frequency, which shifts the entire spectra towards the right (higher frequency). On the optical thin side, the brightness temperature drops fast with a negative slope α_{thin}, which can be approximately expressed by $\alpha_{thin} \approx -0.8 - 0.9\delta$, where δ is the power-low index of the nonthermal electron energy distribution.

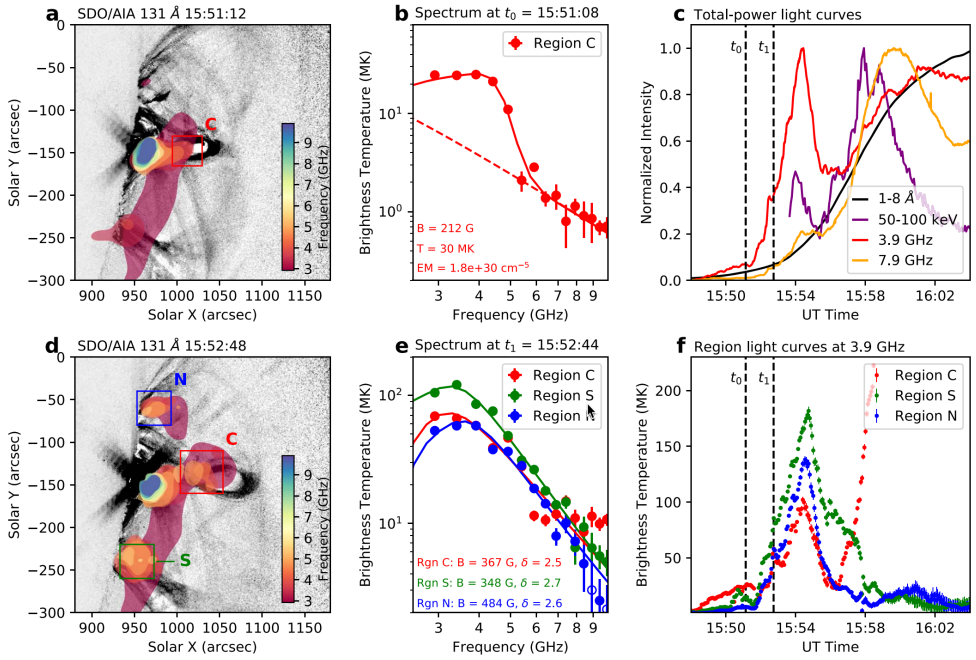

Figure 1.14 Spatially resolved microwave spectra and light curves of the erupting flux rope during the early impulsive phase of the X8.2-class limb flare on Sep 10, 2017 *Source: Chen et al. [37]*

Because of the diagnostic power of the gyrosynchrontron spectra for solar flares, the spatially resolved microwave imaging spectroscopy provides unique diagnostics

that not only reveals the spatial distribution and spectral information of the accelerated electrons but also constrain the magnetic field strength at the emission region. Figure 1.14 shows the EOVSA microwave imaging spectroscopy observation of a limb flare on September 10, 2017. In this observation, the microwave images serve as the probe of nonthermal/thermal electrons and magnetic structure, which shows the geometry evolution of nonthermal electron distribution and magnetic structure. The spectral diagnosis, on the other hand, reveals magnetic field strength and spectral information of the nonthermal/thermal electron, indicating the electron acceleration, transportation, and heating processes during the early impulsive phase of the event. The results agree well with the standard model for eruptive solar flares which is introduced in Subsection 1.1.2. This observation also serves as evidence for particle transport along an erupting magnetic flux rope, which is the basis for the study discussed in Chapter 2.

1.4 Instrumentation

In this dissertation, the flare energy release is mainly derived from multi-band observations of flares. These observations reveal the magnetic field topology and its evolution during the flares at different scales and altitudes. They also provide spatially resolved measurements of plasma temperature, density, kinetics, and other properties. These observations can be used to diagnose the spatial distribution, energy distribution, and density of the accelerated electrons. Finally, they provide diagnostics of the magnetic field strength and measurements or extrapolation of three-dimentional vector magnetic field. The most utilized instruments in this dissertation are:

- **Expanded Owens Valley Solar Array (EOVSA)** The Expanded Owens Valley Solar Array (EOVSA; Gary et al. 84) is a solar-dedicated radio interferometer updated from the Owens Valley Solar Array (OVSA [83]). EOVSA has been providing full sun daily imaging spectroscopy since early

2017, which features a frequency range of 1.1–18 GHz (2.8–18 GHz before 2019), 451 frequencies in 50 spectral windows (134 frequencies in 31 spectral windows before 2019), a high spectral resolution of $\lesssim$ 40 MHz, a high temporal resolution of 1 s (sample time of 20 ms), and full stokes (IQUV) polarization measurements[1]. The EOVSA has thirteen 2.1 m antennas (78 baselines) in a three-armed spiral configuration array with a size of 1.08 km in east-west and 1.22 km in north-south, featuring an angular resolution of 57 ″ and 51 ″ at 1 GHz, respectively. One of the two existing 27 m antennas operates for precision calibration.

- **Goode Solar Telescope (GST)** Goode Solar Telescope (GST; Goode and Cao 95) at Big Bear Solar Observatory (BBSO), is a ground-based telescope that operates at 4305 Å – 10830 Å wavelength range. GST features a 1.6-meter aperture primary mirror and a high-order and multi-conjugate Adaptive Optics (AO) system, which provide an image scale down to 0.08 ″/pixel at 5000 Å. There are five instruments operating on the optical system now, they are Broad-Band Filter Imager (BFI), Visible Imaging Spectrometer (VIS), Near Infra-Red Imaging Spectropolarimeter (NIRIS), Cryogenic Infrared Spectrograph (CYRA), and Fast-Imaging Solar Spectrograph (FISS). VIS is the only instrument that is highly involved in this dissertation, which produces a narrow (0.07 Å) bandpass over a circular field of view measuring 70 ″, tunable within the 550–700 nm range. VIS is currently operating at the Hα line at 6563 ÅThe image cadence is 15 s, in which VIS takes images at 11 wavelengths around the center wavelength. For each wavelength, 25 frames are taken. The image scale of VIS at all the wavelengths is 0.034 ″/pixel. The characteristics of the rest of the imaging/imaging-spectroscopic instruments can be found at BBSO instrument specifications (Retrieved on Apr 1, 2023).

- **Reuven Ramaty High Energy Solar Spectroscopic Imager (RHESSI)** RHESSI [157] is part of Small Explorer (SMEX) missions which is specifically designed to examine the mechanisms of particle acceleration and energy release that occur during solar flares. To accomplish this, RHESSI employs an imaging and spectroscopy technique that analyzes hard X-ray/gamma-ray continua emitted by high-energy electrons, as well as gamma-ray lines produced by energetic ions. RHESSI is capable of providing high-resolution full-sun hard X-rays imaging spectroscopy with a spectral resolution ranges between 1 and 10 keV FWHM over an energy range of 3 keV to 17 MeV and a spatial resolution as fine as 2.3″. RHESSI was launched by NASA on February 5, 2002, and operated until 2018.

[1]The different types of antennas in the array, however, have hampered the commissioning of full polarimetry for scientific use. An upgrade is being proposed to enable this key capability.

- **Solar Dynamic Observatory (SDO; Pesnell et al. 195)** is part of NASA's Living With a Star (LWS) program, which aims to study the Sun and its interactions with the Earth's environment. The SDO equipped with three main instruments, according to the extent of their involvement in this dissertation, they are:

  1. **The Atmospheric Imaging Assembly (AIA; Lemen et al. 148)** takes images of the solar atmosphere in ten wavelengths ranging from extreme ultraviolet (EUV) to ultraviolet (UV). The images feature spatial resolution of 1.5″ and temporal resolution of 12″/24″ for EUV/UV images. The wavelengths are:
     - 94 Å, emitted by Fe XVIII at temperatures of $\sim$ 6 MK, represent regions of the corona during a solar flare.
     - 131 Å, emitted by Fe XX/Fe XXIII at temperatures of $\sim$ 10 MK/$\sim$ 16 MK, represent heated material in solar flare.
     - 171 Å, emitted by Fe IX at temperatures of $\sim$ 0.6 MK, represent quiet corona and magnetic structures like coronal loops.
     - 211 Å, emitted by Fe XIV at temperatures of $\sim$ 2 MK, represent a slightly higher region of the corona and the latter represents hotter, active regions in the solar corona.
     - 304 Å, emitted by He II at temperatures of $\sim$ 0.05 MK. The line is emitted from the upper transition region and the chromosphere in which filaments are readily visible.
     - 335 Å, emitted by Fe XVI at temperatures of $\sim$ 2.5 MK, represent the active regions in the corona.
     - 1600 Å, emitted by C IV and continuum emission at temperatures of $\sim$ 5000 K. The line is emitted from the transition region.
     - 1700 Å, emitted by continuum emission at temperatures of $\sim$ 5000 K. The line is emitted from the photosphere.
     - 4500 Å, emitted by continuum emission at temperatures of $\sim$ 5000 K. The line is emitted from the photosphere.

  2. **Helioseismic and Magnetic Imager (HMI; Scherrer et al. 214)** provides full disk magnetogram and surface flow measurement by taking series of images every 45″ at a wavelength of 6173 Åemitted by FeI line. The full-disk magnetogram contains a line-of-sight magnetic field (LOS) component map (with a cadence of 45″) and vector magnetogram (with a cadence of 720″).

  3. **Extreme Ultraviolet Variability Experiment (EVE; Woods et al. 253** provides solar EUV irradiance from 1 to 1050 Å with a spectral resolution of 1 Å, temporal cadence of 10″, and accuracy of $\sim$20%.

In addition, there are additional instruments that have been analyzed in the works of this dissertation and have played important roles, they are: Large Angle Spectroscopic COronagraph on board the Solar and Heliospheric Observatory

(SOHO/LASCO; Brueckner et al. 27), K-coronagraph of the Mauna Loa Solar Observatory (MLSO/K-Cor; Elmore et al. 67), Extreme UltraViolet Imager (EUVI; Wuelser et al. 256) onboard STEREO-A, one of the two Solar Terrestrial Relations Observatory (STEREO; Kaiser et al. 127) spacecraft, and Gamma-ray Burst Monitor (GBM; Meegan et al. 178).

1.5 Scientific Goal and Dissertation Outline

Although the standard model of solar flares [31, 224, 107, 135] has been successful in interpreting many observational signatures of eruptive flares. However, there are still many problems that remain unresolved. As mentioned in Section 1.1, solar flares are essentially the process of releasing the free magnetic energy stored in the solar corona by drastic reconfiguration of the coronal magnetic field. The "big questions" in this process, are summarized in Benz [19] as:

- **Coupling atmospheric layers**: How do flare signatures in the photosphere, chromosphere, and corona relate to each other?
- **Flare geometry**: Where is the flare energy released?
- **Energy budget**: What forms is the energy released into?
- **Signatures**: Which emissions are direct signatures of energy release?
- **Acceleration processes**: How are particles accelerated?

With the "big questions" in mind, this dissertation focuses on two "specific questions":

- What are the three-dimensional magnetic structures of solar flares and MFRs?
- What is the relationship between the different forms of energy that are released during a flare? How are they coupled together?

With the diagnostics of the magnetic field and nonthermal electrons using microwave imaging spectroscopy observations combined with multi-wavelength data, this dissertation aims to shed some light on these two specific questions. Chapter 2

reports an EOVSA microwave imaging spectroscopy observation of an M1.4-class solar flare that occurred on 2017 September 6. This flare event is associated with a partial eruption of a twisted filament observed in Hα by GST/VIS. The event features a microwave counterpart, whose spatial and temporal evolution closely follows the filament seen in Hα and EUV. Using spatially resolved microwave spectral analysis, we derive the magnetic field strength along the filament spine, and compare it to the non-linear force-free magnetic model extrapolated from the pre-flare photospheric magnetogram. Chapter 3 presents another case study with EOVSA microwave imaging spectroscopy observation. The event is a C9.4-class eruptive limb flare occurred on 2017 August 20, which is accompanied by a magnetic flux rope eruption and a white light coronal mass ejection. The event features three post-impulsive X-ray and microwave bursts immediately following its main impulsive phase. For each burst, both microwave and X-ray imaging suggest that the non-thermal electrons are located in the above-the-loop-top region. Interestingly, contrary to many other flares, the peak flux of the three post-impulsive microwave and X-ray bursts shows an increase in time. During the main-impulsive phase and each post-impulsive phase burst, the acceleration of the magnetic flux rope and the non-thermal energy release are measured by microwave/X-ray spectral analysis and EUV feature tracking, respectively. We discuss the correlations between flux rope acceleration and electron energization in three post-impulsive phase bursts. We also discussed the potential impact of the guide field on the acceleration of non-thermal electrons in each phase. In Chapter 4, the major results are summarized and discussed in the context of the two specific questions. Future work is also discussed in Chapter 4.

CHAPTER 2

CORONAL MAGNETIC FIELD MEASUREMENTS ALONG A PARTIALLY ERUPTING FILAMENT IN A SOLAR FLARE

2.1 Introduction

Magnetic flux ropes (MFRs) are the key to understanding solar eruptions [69]. Since the magnetic field plays a dominant role in the low-plasma-β environment in the low solar corona, measurements of the magnetic properties of MFRs are crucial for understanding their triggering and the associated energy release processes, leading to major solar activities [165].

To date, the most commonly used method to infer the magnetic field of MFRs is through nonlinear force-free field (NLFFF) extrapolations [252]. While the NLFFF method has provided important insights into the magnetic topology and, in some cases, the evolution of the MFRs [e.g., 133, 121, 101], it is, after all, an indirect method with intrinsic limitations [see., e.g., 182, 56, for discussions]. Direct measurements of the coronal magnetic field based on the Zeeman effect, Hanle effect, or a combination of both, have been performed by using polarization measurements of optical or infrared (IR) lines [154, 91, 208]. Occasionally, this technique has been applied to the measurements of the magnetic field of prominences/filaments [23, 181] and coronal rain [145]. Linear polarization of IR forbidden lines are also used to probe the magnetic structure of coronal cavities [61, 17]. Recently, there has also been success in constraining the coronal magnetic field by using certain EUV lines sensitive to the magnetically induced transition (MIT) effect [24, 43, 147]. However, these measurements are often limited by the signal-to-noise ratio and require a relatively long integration time. For instance, with current optical/IR instrumentation, it typically takes tens of minutes for linear polarization and hours for circular polarization [17]. Although the required integration time will be reduced

by an order of magnitude with the operation of the Cryo-NIRSP spectropolarimeter at the Daniel K. Inouye Solar Telescope [105] in the near future (thanks to its large collecting area), it will remain difficult to track the rapidly evolving magnetic field of MFRs at a time scale of order 1–10 s in solar eruptions and flares. In addition, because the spectral lines from the coronal plasma are orders of magnitude weaker than their counterpart from the photosphere, such measurements can only be made above the solar limb.

Waves and oscillations have also been used to diagnose the coronal magnetic field [see, e.g., reviews by 189, 3, and references therein]. Despite recent success to obtain spatially resolved maps of the coronal magnetic field above sunspots [123] and of the quiescent corona [259], it remains difficult to diagnose the rapidly evolving and complex magnetic structures in the flaring region.

Microwave spectral diagnostics provide another means for measuring the coronal magnetic field both over the limb and against the disk. The microwave emission arises from thermal or nonthermal electrons gyrating in the magnetic field, producing gyroresonance or gyrosynchrotron radiation with spectral properties sensitive to the magnetic field strength and direction [79]. Thanks to the operation of the Expanded Owens Valley Solar Array (EOVSA) [193, 84], significant progress has been made in measuring the dynamically evolving coronal magnetic field in solar flares using spatially resolved microwave spectroscopy at a high, 1-s cadence. The technique of faithfully reconstructing a coronal magnetic field map of a flare arcade has been previously demonstrated by Gary et al. [82] using a three-dimensional model arcade filled with nonthermal electrons. With EOVSA data, a fast decay of the coronal magnetic field in the cusp region above the flare arcade was first reported by Fleishman et al. [72]. In Chen et al. [34], EOVSA imaging spectroscopy is used to derive the magnetic field profile along a large-scale reconnection current sheet trailing an erupting MFR, which matches very well with results from numerical simulations.

Similar techniques can be used to derive spatially resolved measurements of the magnetic field along an erupting MFR. However, such measurements have not been realized heretofore due to the lack of suitable observational data. This work will fill that gap.

Although nonthermal counterparts of the erupting MFRs or coronal mass ejections (CMEs) have been occasionally reported in both radio [223, 81, 12, 242, 171, 236, 10, 30, 187, 36, 183, 49] and X-ray wavelengths [128, 116, 139, 94], where the nonthermal electrons are accelerated and how they gain access to the MFR/CME cavity remain outstanding questions. In the low corona, it is often assumed that the electrons, presumably accelerated at or around the flare reconnection site, are injected into the MFR cavity following the newly reconnected field lines. In the upper corona, additionally, the CME-driven shocks may play an increasingly important role in particle acceleration. As such, transport of the shock-accelerated electrons (and ions) from downstream of the shock to the CME cavity would be important for understanding the associated nonthermal emissions. To elucidate these processes, detailed spectral imaging of these radio/X-ray sources with sufficient temporal and angular resolution would be particularly helpful. In a recent study by Chen et al. [36], aided by spectral imaging enabled by EOVSA, microwave counterparts that outline the central region and the two conjugate footpoints of an erupting MFR cavity have been identified in the low corona ($<0.2R_{\odot}$ above the surface) with an edge-on viewing perspective. Their similar light curves and spectral properties suggest that the three sources are likely associated with the same nonthermal electron population injected from the underlying reconnecting current sheet during the erupting of the MFR.

Here we report a multi-wavelength study of a GOES M1.4-class solar flare on 2017 September 6, which is associated with a partial eruption of a filament. Different from the event in Chen et al. [36], which has an edge-on viewing perspective over the limb, this erupting filament is viewed against the solar disk, thus giving us a unique

opportunity to derive the coronal magnetic field *along* the filament axis using both microwave spectral analysis and non-linear force-free field (NLFFF) extrapolations. After an overview of the multi-wavelength observations and a discussion of the flare context in Section 2.2, we present the microwave imaging spectroscopy observations of the filament eruption in Section 2.3. Also discussed there are the magnetic field measurements returned from the spatially resolved microwave spectral analysis in comparison to the NLFFF extrapolation results. In Section 2.4, we discuss the nature of the filament/MFR system revealed by the multi-wavelength observations, as well as a possible interpretation of the partial eruption.

2.2 Event Overview

2.2.1 Multi-wavelength data

The flare under study took place in active region (AR) 12673, which had a record-breaking fast magnetic flux emergence [226] and high photospheric and coronal magnetic field strength [244, 4]. The event occurred about 7 hours after the peak of the X9.3 class flare (SOL2017-09-06T11:53, the largest flare in Solar Cycle 24) in the same AR. During the decay phase of the X9.3 flare, 4 M-class flares occur, including the SOL2017-09-06T19:29:30 M1.4 flare[1] under study here (Figure 2.1(C)). At the time, as shown in Figure 2.1(B), the photospheric magnetic field configuration of the AR appears as a quadrupolar configuration.

The observation of the flaring region obtained by the 1.6-m Goode Solar Telescope of the Big Bear Solar Observatory (BBSO/GST; Cao et al. 29) is available from 19:00 UT–20:09 UT. The Visible Imaging Spectrometer (VIS) at GST provides observation in Hα 6563 Å line center and line wing ($\pm$0.4 Å and $\pm$0.8 Å), with an

[1]The flare classes quoted here follow those reported by NOAA based on GOES 15 data. We note that the GOES 16 shown in Figure 2.1(C) reports a 1–8 Å flux of 2.2×10^{-5} W m^{-2} at the peak of this event, which would be named an M2.2 class. Such an inconsistency is due to a scaling factor applied to data prior to GOES 16, which is well documented by NOAA/NCEI (`https://www.ngdc.noaa.gov/stp/satellite/goes-r.html`, Retrieved on Apr 1, 2023).

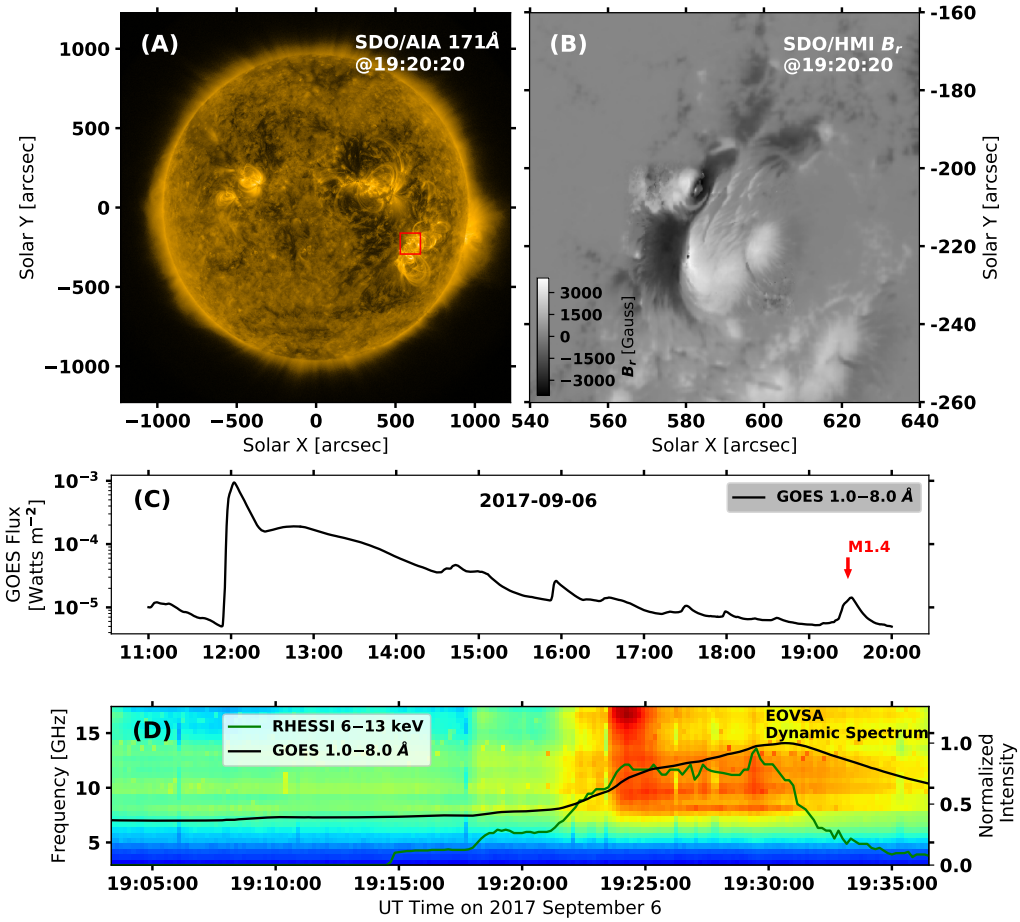

Figure 2.1 (A) AR 12673 as observed in EUV by the SDO/AIA 171 Å filterband on 2017 September 6 at 19:20:20 UT. (B) Detailed view of the SDO/HMI radial field magnetogram of the core region of the AR (red box in (A)). (C) GOES 1–8 Å soft X-ray (SXR) light curve from 11 UT to 20 UT on 2017 September 6. The M1.4 flare event under study (marked by the red arrow) occurs during the late decay phase of the large X9.3 flare. (D) Background-subtracted EOVSA microwave dynamic spectrum from 19:03 UT to 19:37 UT. The black and green curves are for RHESSI 6–13 keV X-ray and GOES 1–8 Å light curves, respectively.

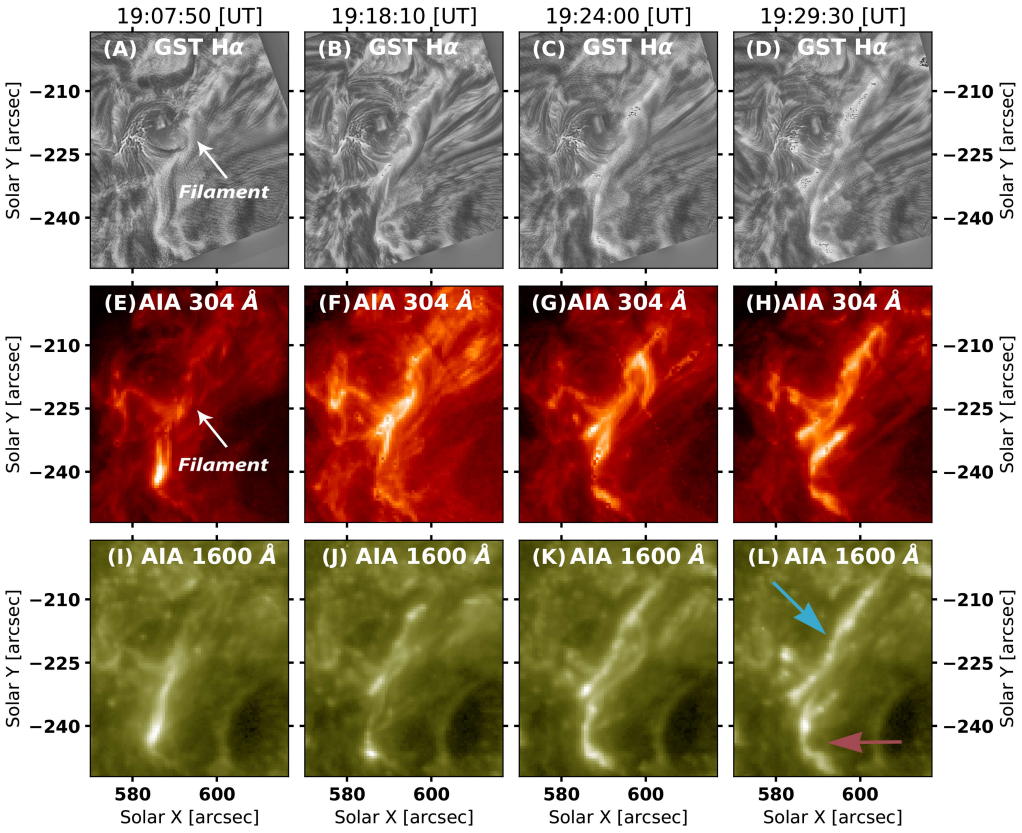

Figure 2.2 (A)–(D) BBSO/GST Hα line center images at four selected times during the event. (E)–(H) SDO/AIA 304 Å images. The dark filament, seen in both Hα and 304 Å, is marked by the white arrows. (I)–(L) SDO/AIA 1600 Å images showing the development of the two flare ribbons (arrows in (L)).

angular resolution of $0''.1$ and a field-of-view (FOV) of $57'' \times 64''$. The Helioseismic and Magnetic Imager (HMI; Scherrer et al. 213) and the Atmospheric Imaging Assembly (AIA; Lemen et al. 149) on-board the Solar Dynamics Observatory (SDO; Pesnell et al. 195) provide full-disk magnetograms and multi-band extreme-ultraviolet (EUV) and ultraviolet (UV) images, respectively, with an angular resolution of $1''$–$1''.5$. The images from BBSO/GST are enhanced with the multi-scale Gaussian normalization (MGN) method [186]. The Reuven Ramaty High Energy Solar Spectroscopic Imager (RHESSI; Lin et al. 157) observed the event from 19:15 UT. The X-ray response from this flare can be detected against the background up to ∼13 keV. X-ray imaging reconstruction is performed during the flare peak using the standard CLEAN method [117] at 6–13 keV with an integration time of 120 s.

The M1.4 event is fully covered by EOVSA with 134 frequencies in 2.5–18 GHz over 31 evenly spaced spectral windows (referred to as SPW 0 to SPW 30). Phase calibration was done against a celestial source 1229+020. A self-calibration procedure in both phase and amplitude is performed based on a 4-s-averaged data around the flare peak. Most of the enhanced microwave emission associated with the flare is in the 5–18 GHz range, which will be the focus of our analysis in Section 2.3.

2.2.2 Partial eruption of a pre-existing filament

At 19:00 UT, when the GST observation of this event starts, a dark filament can be clearly identified in the Hα line center images with many strands that appear twisted (Figure 2.2(A)). The filament can also be distinguished in SDO/AIA 304 Å images albeit with a much lower angular resolution (Figure 2.2(E)). The filament aligns with the magnetic polarity inversion line (PIL) as evidenced in the SDO/HMI radial field magnetogram (Figure 2.3(D)). The magnetogram shows the radial field component B_r derived from the full vector magnetic field measurements (which mitigates the projection effect; see Sun 225) The filament corresponds to highly sheared magnetic

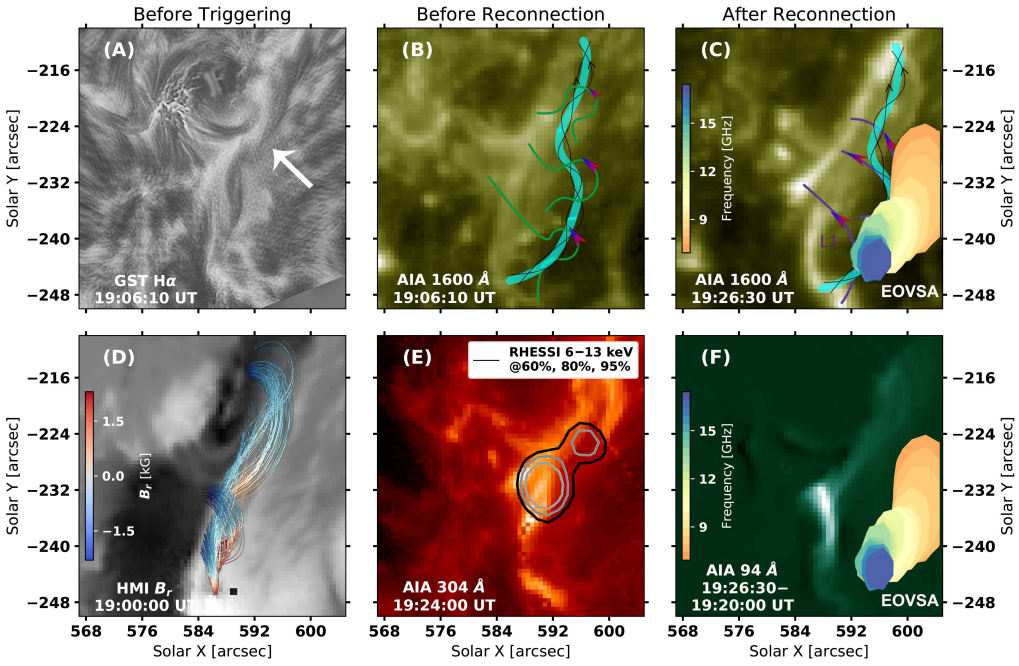

Figure 2.3 (A) Filament as seen by BBSO/GST Hα before the onset of the event at 19:06:10 UT (white arrow). (B) and (C) Schematic of the pre- and post-reconnection magnetic field lines (green and purple curves) induced by the rising filament. The background is the corresponding SDO/AIA 1600 Å image showing the formation of the two bright flare ribbons. EOVSA 6.4–15.9 GHz images at 19:26:30 (pre-flare background subtracted) are also shown in (C) as color contours (90% of the maximum). (D) Selected field lines near the PIL region derived from the NLFFF results based on the SDO/HMI vector magnetogram at 19:00 UT. (E) RHESSI 6–13 keV X-ray source (60%, 80%, and 95% of the maximum) overlaid on SDO/AIA 304 Å EUV image during the impulsive phase. X-ray spectral analysis suggests that the source is associated with thermal bremsstrahlung emission from ∼28 MK plasma. (F) Base difference SDO/AIA 94 Å image (19:26:30−19:20:00 UT) showing the bright post-reconnection flare arcade. EOVSA 6.4–15.9 GHz contours at 19:26:30 are also shown.

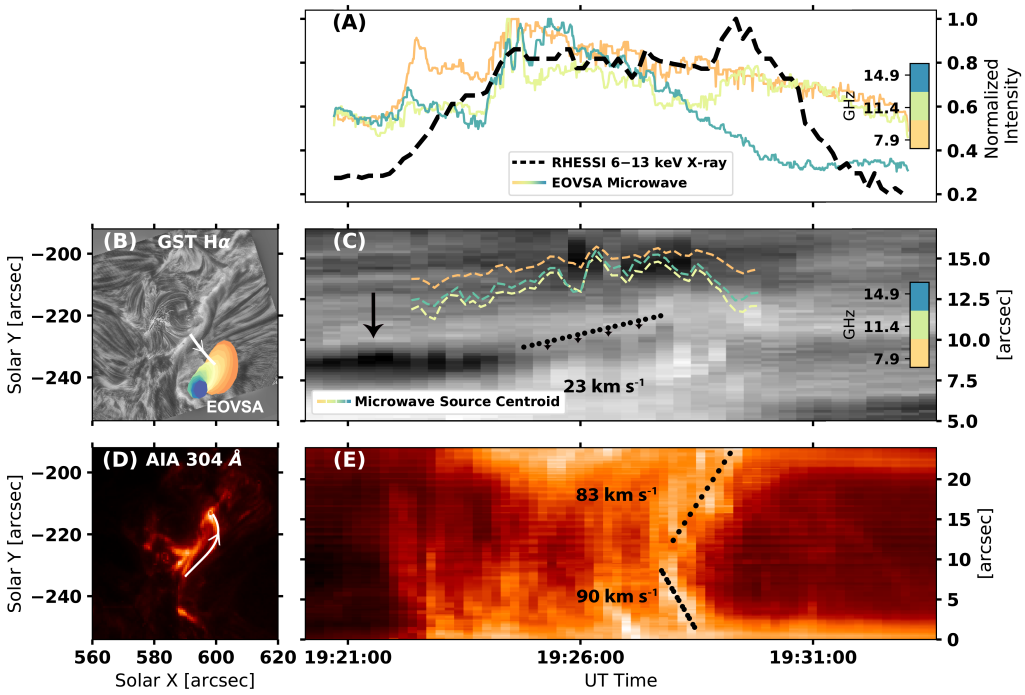

Figure 2.4 (A) X-ray and microwave light curves during the partial eruption of the filament. (B) Reference BBSO/GST Hα image at 19:20:20 UT overlaid with EOVSA 7.9–15.9 GHz contours (90% of the maximum). (C) Time–distance stack plot of the BBSO/GST Hα image series made along a slice as indicated by the white curve in (B). The color dashed curves indicate the location of EOVSA microwave centroid at three selected frequencies. The dark, rising filament is indicated by the black arrow. (D) Reference SDO/AIA 304 Å image at 19:20:20 UT. (E) Time–distance stack plot made along the filament (white curve in (D)), showing the draining filament material following the partial eruption.

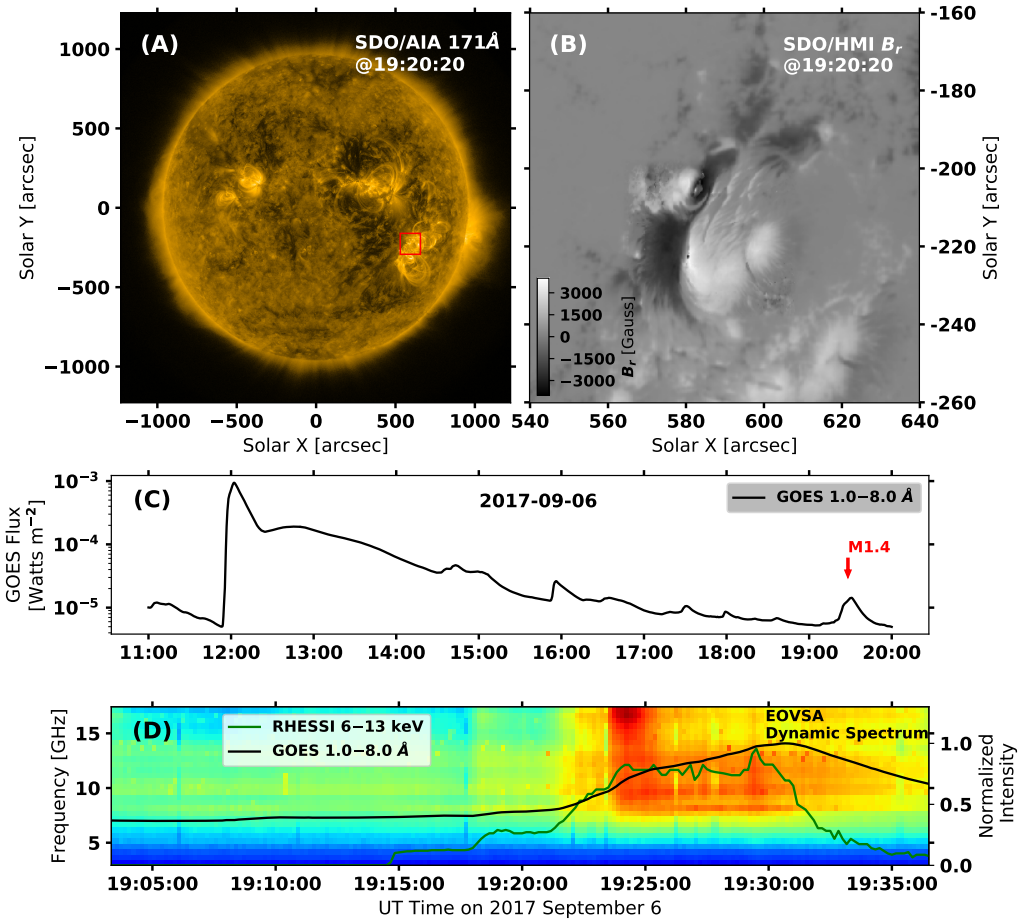

Figure 2.5 (A)–(D) Running difference image of LASCO C2 coronagraph at selected times showing a narrow eruptive feature in the upper corona associated with the M1.4 flare event (red arrows). (E) Time–distance plot of LASCO C2 running difference image series obtained from the slice shown as a dotted line in (A)–(D). GOES light curve of the day is also shown for reference. The vertical red dashed line indicates the time when the event occurs. The yellow dashed line traces the eruption and extrapolates it back to time of the M1.4 flare that peaks at 19:29 UT.

field lines near the PIL (colored curves in Figure 2.3(D)) derived from the NLFFF results based on the pre-event SDO/HMI vector magnetogram.

The flare enters its impulsive phase at around 19:22 UT. The southern tips of both ribbons brighten first (Figure 2.2(J)–(L)). The post-reconnection flare arcade that connects the southern tips of the ribbons is clearly seen in SDO/AIA channels sensitive to hot flaring plasma, as shown in Figure 2.3(F). During this period, an upward motion of the filament is also observed (see Figure 2.2. Figure 2.4(C) shows the time-distance diagram derived from the Hα time-series images made at a slice that is nearly perpendicular to the filament axis (thick curve in Figure 2.4(B)). Synchronous with the onset of the impulsive phase of the flare, the dark filament starts to rise with a projected speed of $\sim$23 km s^{-1} (Figure 2.3(A)). Meanwhile, the 6–13 KeV RHESSI source appears near the top of the bright EUV flare arcade. X-ray spectral analysis suggests that the source is associated with thermal bremsstrahlung emission from $\sim$28 MK plasma (not shown here).

The multi-wavelength observations during the impulsive phase are generally consistent with the standard scenario of eruptive flares as illustrated in Figures 2.3(B) and (C). The rising filament, likely the lower portion of a twisted MFR, stretches the overlying field lines, leading to magnetic reconnection below the filament/MFR. The energy release associated with the reconnection results in a bright EUV flare arcade and a looptop X-ray source as shown in Figures 2.3(E) and (F).

During the impulsive phase of the flare, at $\sim$19:26:20 UT, the rising Hα filament appears to go through a fast eruption and quickly disappears from the field of view of BBSO/GST. Immediately following the eruption, the filament material starts to drain toward either end. Owing to the relatively small scale of the eruption, it is rather difficult to trace the erupted filament material into higher altitudes. However, we have identified a small and narrow CME in the SOHO/LASCO C2 running difference images, as shown in Figures 2.5(A)–(D). Both the initiation time and location of the

eruption, after extrapolating the white light CME in the time-distance diagram in the upper corona ($> 2.5 R_{\odot}$; shown in Figure 2.5(E)) back to the solar surface, are consistent with those of the M1.4 flare event. Considering that the filament feature is still distinguishable after the event (but with an altered appearance), we conclude that only a fraction of the filament material has erupted. Hence, after Gibson and Fan [86, 87], we refer to this event as a "partial eruption."

2.3 Microwave Observations

2.3.1 Microwave counterpart of the erupting filament

In this study, we combine all channels of each of the 30 spectral windows centered at 3.4 to 17.9 GHz (SPW 1–SPW 30) to produce microwave images at 30 equally spaced frequencies. The microwave images at all frequencies feature a source near the filament seen in (E)UV and Hα images. In Figures 2.6(A)–(H)), we choose two representative frequencies (6.9 GHz and 12.4 GHz) to demonstrate the morphology of the microwave sources. Prior to the flare event, the microwave sources are mainly concentrated in the AR with strong magnetic field (Figures 2.6(A) and (E)), indicative of thermal emission associated with the AR (which will be further discussed in the next sub-section). During the event, the microwave source at both frequencies start to display an elongated shape stretching along the direction of the filament. To display the microwave source morphology at different frequencies more clearly, we perform pre-flare background subtraction on all the microwave images and discuss the resulting images in the subsequent analysis. The kernel of these pre-flare background-subtracted microwave sources, defined as 90% of the maximum brightness of each image, is closely aligned with the filament (Figures 2.3(C)). Intriguingly, the microwave emission kernels at the different frequencies form a coherent structure that is distributed along the filament, with its high-frequency end located closer to the southern leg of the filament (Figure 2.3(C)).

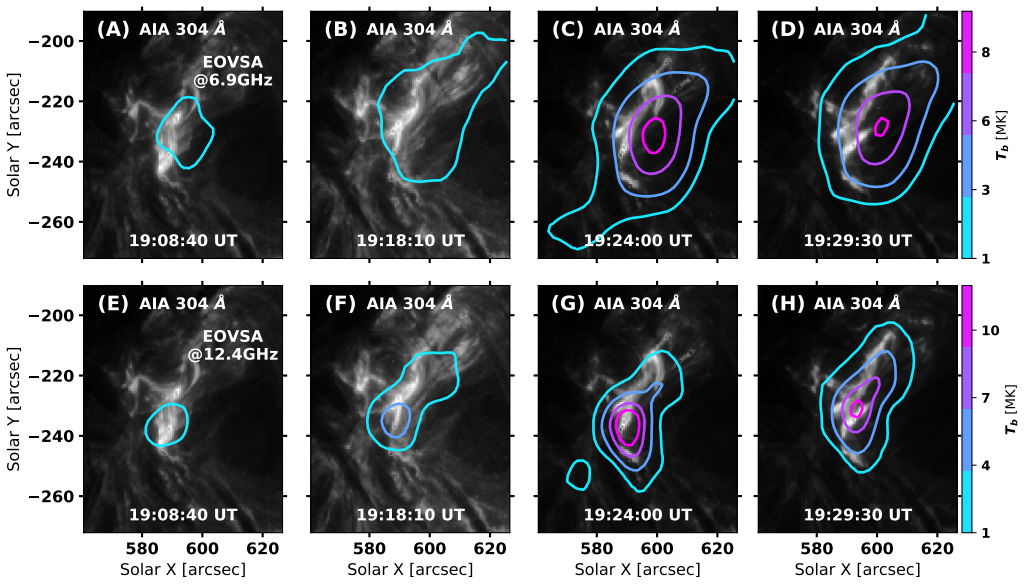

Figure 2.6 Morphology and evolution of EOVSA microwave sources at 6.9 GHz (A)–(D) and 12.4 GHz (E)–(H). Note the contour levels correspond to absolute brightness temperature values shown in the color bars on the right. The background images are from SDO/AIA 304 Å images at the same selected times as those in Figure 2.2.

Moreover, a detailed look at the temporal variation of the source location reveals that the microwave source and the filament also move synchronously during its slow rise phase. In Figure 2.4(C), we show the evolving location of the microwave source kernel (at three selected frequencies) along the same slice used for generating the Hα time–distance stack plot. It is clear that the microwave source rises synchronously with the Hα filament at a similar speed, $\sim$23 km s^{-1} in projection, albeit with a slight, 5–6″ offset toward the direction of the rise motion. Such a close spatial association and synchronized motion between the multi-frequency microwave source kernels and the Hα/EUV filament strongly suggests that the microwave source is a counterpart of the erupting filament. The relation between the microwave emission and the filament will be further discussed and interpreted in Section 2.4.

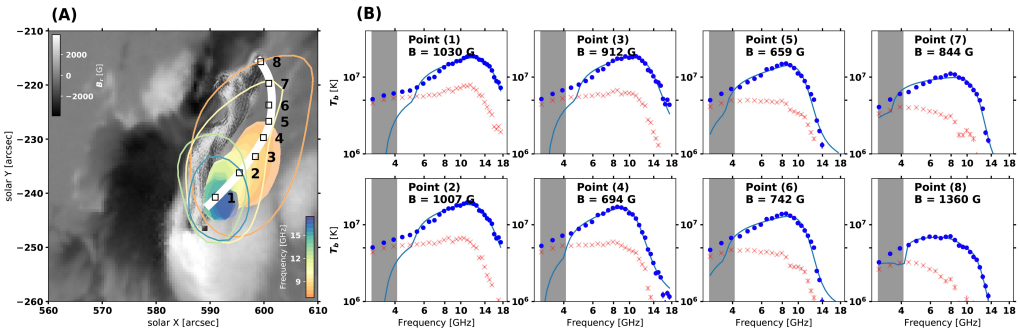

Figure 2.7 Spatially resolved microwave spectra along the microwave counterpart of the erupting filament. (A) Multi-frequency EOVSA microwave images (pre-flare-background subtracted) at 19:24:00 UT. Open and filled contours are 50% and 90% of the maximum, respectively. Background is the pre-flare photospheric magnetogram from HMI, showing the radial component B_r. The filament shown is extracted from the BBSO/GST Hα image. (B) Spatially resolved microwave brightness temperature spectra derived from selected locations along the extension of the microwave source (black squares). The thick white line indicates the selected magnetic flux tube derived from NLFFF extrapolations, which is used to compare with the results obtained by microwave spectral analysis. The spatially resolved spectra and the best fit model are shown as filled blue circles and solid blue curves, respectively. For comparison, the pre-flare microwave spectra at the same locations are shown as the red crosses.

2.3.2 Microwave spectral analysis

In Subsection 2.3.1, we have suggested that the microwave sources are the counterpart of the erupting filament. To investigate the physical parameters of the microwave source region, we derive spatially resolved microwave brightness temperature spectra obtained at different spatial locations along the elongation direction of the microwave source (black boxes in Figure 2.7(A)). Figure 2.7(B) shows the brightness temperature spectra obtained from eight selected locations during the first microwave peak at 19:24 UT (solid blue circles). The pre-flare spectra, obtained from the same locations but at 19:03:10 UT, are shown as the red crosses. We note that the spectra at frequencies below 4.5 GHz show little enhancement during the flare. They have a brightness temperature of $\sim$7 MK and display a nearly flat spectral shape. The corresponding microwave images are also very extended, encompassing almost the entire active region. We suspect that this spectral regime has a significant contribution from

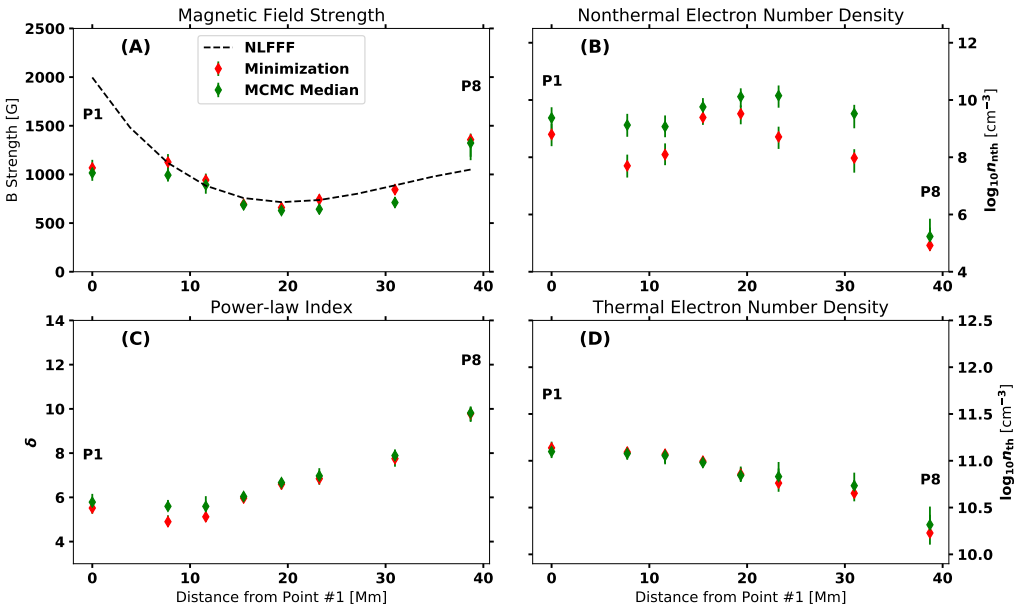

Figure 2.8 Spatial variation of key fit parameters along the microwave counterpart of the erupting filament. Panels (A)–(D) show, respectively, the magnetic field strength B, nonthermal electron density $n_{\rm nth}$, power-law index of the electron energy distribution δ, and thermal plasma density $n_{\rm th}$. Red and green symbols denote those constrained from the χ-square minimization and MCMC, respectively. Also shown in (A) is the magnetic field strength derived from a magnetic flux tube that passes the eight selected locations in the NLFFF results (dashed black curve).

the background thermal emission from the active region, possibly enhanced by the previous X9.3 event. Therefore, in our spectral analysis, we have excluded the data points at <4.5 GHz (shaded gray in Figure 2.7B). At >4.5 GHz, the microwave spectra show a prominent increase during the flare, suggestive of their intimate relationship to the flare energy release. The spectral shape has a positive slope below a peak frequency of ∼8–10 GHz and a negative slope above the peak, characteristic of the nonthermal gyrosynchrotron radiation [64, 79].

We use the fast gyrosynchrotron code of [70] to calculate the nonthermal microwave emission by assuming a homogenous source along the line of sight (LOS) with a power-law electron energy distribution. After Fleishman et al. [72], we adopt a downhill simplex method (implemented in SciPy's [240] `minimize` package as the "Nelder-Mead" algorithm) to minimize the χ-square differences between the observed

and modeled gyrosynchrotron spectra. For the χ-squared minimization based spectral fit, four free parameters are used, which include the magnetic field strength B, the total number density of nonthermal electron $n_{\rm nth}$, the power-law index of the electron energy distribution δ, and the thermal electron density $n_{\rm th}$. The column depth is fixed to $10''$, a value assumed based on the source size in the plane of the sky. The energy range of the power-law distribution is fixed to 10 keV–10 MeV, and the temperature of the thermal plasma is fixed to 7 MK. Following Chen et al. [34] and Chen et al. [40], we also adopt the Markov chain Monte Carlo (MCMC) method to evaluate the reliability and uncertainties of the fit parameters. The best-fit spectra are shown in Figure 2.7(B) as the solid blue curves. The corresponding best-fit parameters of the eight selected locations are shown in Figure 2.8. For completeness, we also show the median values and the associated 1-σ range of the MCMC posterior distributions as the green symbols.

The spectral fit results return a spatially varying magnetic field strength B along the microwave counterpart of the filament, shown in Figure 2.8(A) as red and green symbols (from the minimization and MCMC median, respectively): It decreases from $\sim$1000 G at the southern end of the source to $\sim$600 G near the center, and then increases to $>$1000 G at the northern end. To compare this microwave-constrained magnetic field distribution with the NLFFF results, we extract the magnetic field strength values from an NLFFF-extrapolated magnetic flux tube that passes the selected fit locations in projection, shown in Figure 2.8(A) as the black dashed curve. The two results achieve a qualitative agreement with each other, despite some deviations at either end. The latter may be attributed to the projection effect and/or temporal evolution of the coronal magnetic field from the pre-flare phase when the NLFFF results are derived.

The spectral index of the electron distribution δ and nonthermal electron density $n_{\rm nth}$ also vary along the microwave source, with a greater $n_{\rm nth}$ and a harder δ near

the southern leg of the MFR. It is consistent with the observations presented in Section 2.2, where the bright EUV flare arcade appears near the southern end of the PIL, indicating that the energy release and the associated electron acceleration may be more profound there.

2.4 Summary and Discussions

In the previous sections, we have presented microwave, Hα, and (E)UV observations of a filament that undergoes a partial eruption during an M1.4-class solar flare. In particular, the multi-frequency microwave counterpart of the filament closely follows the morphology and dynamics of the rising filament as seen in Hα and EUV. By fitting the spatially resolved microwave spectra using a gyrosynchrotron radiation model, we derive the magnetic field strength along the filament, which ranges from 600–1400 G from its apex to the legs. The microwave-constrained magnetic field yields a reasonable agreement with those derived from the NLFFF extrapolation. These results strongly suggest that the observed microwave, Hα, and EUV features are all closely associated with the same coherent magnetic structure that hosts the filament, presumably a twisted MFR that undergoes a partial eruption.

It is particularly intriguing that although the multi-frequency microwave source encompasses the filament, the centroid of the microwave source is located consistently above the rising filament as seen in Hα/EUV (Figures 2.4(C)). Figure 2.9(A) shows a representative frame at 19:24:00 UT with EOVSA microwave sources overlaid on the composite AIA 1600 Å (green background) and BBSO/GST Hα (grayscale) image. Similar to Figure 2.7(A), open and filled color contours are 50% and 90% of the microwave source, showing, respectively, the spatial extension and the central kernel of the source at each frequency. We note the viewing geometry of this event is nearly top-down but slightly tilted toward the west. In Figure 2.9(B), we show a schematic of the cross-section of the filament–MFR system (indicated by the

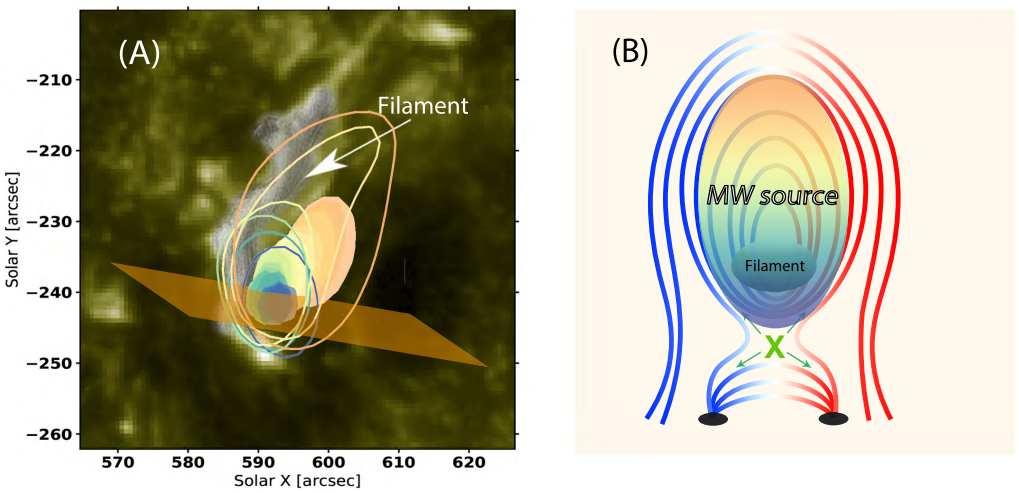

Figure 2.9 Schematic cartoon that shows the relationship between the filament and the microwave source. (A) Multi-frequency EOVSA microwave images (pre-flare-background subtracted) at 19:24:00 UT. Open and filled contours are 50% and 90% of the maximum, respectively. Background is the SDO/AIA 1600 Å image at the moment and the filament shown is extracted from the BBSO/GST Hα image. (B) Schematic cartoon of the cross-section of the flux rope, at a location indicated by the orange surface in (A).

orange plane in (A)). The relative location and cross-section of the microwave source and the filament are illustrated by the green-yellow and gray ellipse, respectively. The position difference between the microwave source and the Hα filament can be understood within the standard scenario of the "three-part" structure of the filament–MFR system in conjunction with the reconnection-driven flare energy release associated with the (partial) filament eruption [e.g., 87, 61, 39, and references therein]: The cool, dense filament observed in Hα and EUV 304 Å can be explained as chromospheric-temperature material supported near the concave-upward bottoms of the field lines of an MFR. Meanwhile, accelerated electrons due to magnetic reconnection induced by the partial filament eruption can enter the extended MFR/CME cavity following the newly reconnected field lines [see, e.g., 94, 34], producing the extended nonthermal microwave source above the rising filament. We note that similar phenomena have also been observed in the upper corona using radio data obtained at longer wavelengths: there have been reports of moving type IV radio

bursts or "radio CMEs" located ahead of the erupting filament [242] or accompanying the extended CME cavity [12, 171, 30, 183, 49].

Because the microwave intensity depends strongly on both the nonthermal electron distribution and the magnetic field strength, the slight offset of the kernel of the microwave emission as a function of frequency relative to the filament contains important information of the magnetic structure and nonthermal electron distribution. Also, the nonthermal-to-thermal electron fraction in the microwave source (which can be up to 10%; c.f., Figures 2.8(B) and (D)) may provide diagnostics for the acceleration processes. However, since the nonthermal electrons responsible for the observed microwave sources are probably accelerated elsewhere, they cannot be understood straightforwardly without detailed modeling of electron acceleration and transport in the eruption-induced magnetic reconnection geometry. An in-depth interpretation for such observed phenomenon is a topic for future studies that incorporates macroscopic plasma and particle modeling.

Finally, we offer a possible interpretation for the partial eruption of the filament–MFR system under the framework of the torus instability. Following earlier works [e.g., 14, 130], we calculate the potential coronal magnetic field above the AR, and compute the decay index using the transverse component of the pre-flare potential field. Figure 2.10 shows the decay index map in a vertical plane that aligns with the main filament axis (nearly perpendicular to the orange plane in Figure 2.9(A)). The regions colored in brown have a decay index of <1.5, which are stable against the torus instability. In contrast, the regions colored in green have a decay index of >1.5, where the MFR is unstable to the torus instability and hence is more likely to erupt. It can be seen from the decay index map that the MFR is largely stable against the torus instability. However, once the filament is activated and driven upward by, e.g., the Lorentz force from pre-flare reconnection events [124], the southern portion of the filament (to the right in the diagram) can quickly ascend into a region in the

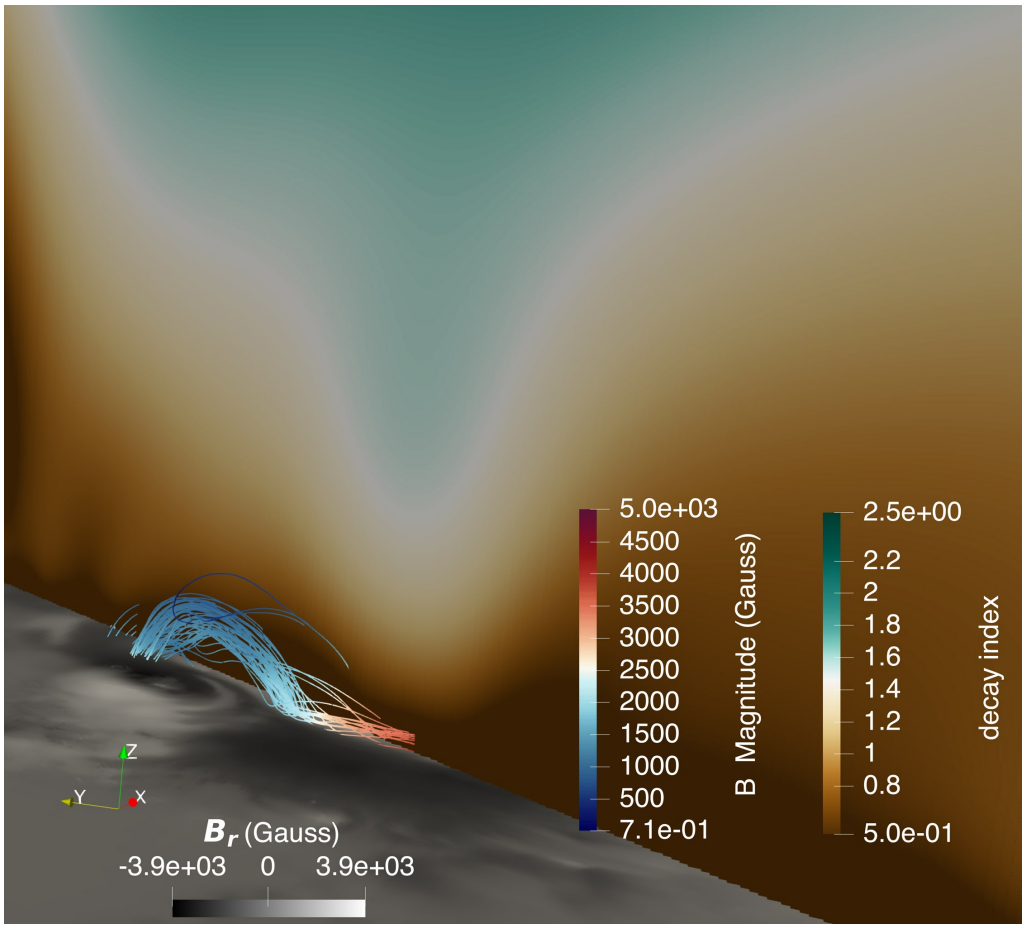

Figure 2.10 Decay index distribution above the flux rope. The decay index is calculated from the potential extrapolated magnetic field while the flux rope is from the NLFFF extrapolation.

torus-unstable regime. However, the northern portion of the filament has much more difficulty erupting owing to the more extended torus-stable region above the MFR. Such a north-south asymmetry may explain the observed partial eruption of the filament and the concentration of the nonthermal microwave source near its southern end.

To briefly summarize, by combining multi-wavelength observations from BBSO/GST, SDO, RHESSI and, in particular, microwave imaging spectroscopy observations from EOVSA, we provide the first measurement of the spatially resolved magnetic field along an erupting filament in a flare-productive AR. The microwave-constrained results are qualitatively consistent with those derived from the NLFFF extrapolation.

Our study demonstrates the unique role of microwave imaging spectroscopy observations in measuring the dynamic magnetic field and accelerated electrons on the active Sun. However, the limited angular resolution, dynamic range, and image fidelity of EOVSA observations of this event do not allow us to derive a detailed map of the magnetic field distribution above the filament. Such a magnetic map would provide the most direct constraints for understanding the eruption conditions including the decay index. These measurements should be routinely available with a next generation solar radio telescope with improved spatial resolution, such as the Frequency Agile Solar Radiotelescope [13].

CHAPTER 3

EPISODIC ENERGY RELEASE DURING THE POST MAIN IMPULSIVE PHASE OF A SOLAR FLARE

3.1 Introduction

The relationship between the kinematics of the coronal mass ejections (CMEs) and the corresponding flaring emissions is important in understanding how magnetic energy is released and subsequently converted into different forms of energy in solar eruptions [e.g. 155]. The close temporal correlation between flare X-ray emission and the early kinematics evolution of the erupting magnetic flux rope/filament during the main impulsive phase (MIP) has been widely observed [263, 172, 229]. As a direct indicator of the flare reconnection, the rate of the magnetic flux change, inferred using the advancing flare ribbon at the photosphere, is found to show a temporal correlation with the acceleration of the associated filament eruption/CME [203, 114]. In a follow-up statistical study, close correlations are found between the acceleration of the erupting filaments and the magnetic flux change rate [125]. More recently, by analyzing a large sample of CME-associated flare events, Zhu et al. [267] confirmed the strong correlation between the peak filament/CME acceleration and the peak rate of magnetic flux change. In addition, they revealed a positive correlation between the total reconnected magnetic flux and the maximum CME velocity in events accompanied with fast CMEs (> 600 km s^{-1}). Such a correlation strongly suggests that the magnetic energy release rate is closely related to flux rope eruption. The correlation is also revealed in resistive magnetohydrodynamic (MHD) simulations [45, 209, 210].

As discussed by Welsch [250], the mechanisms of the flux rope/CME acceleration can be grouped into two general categories: (1) Lorentz force in and around the magnetic flux rope that directly drives its acceleration. These models suggests the

increasing Lorentz force during the flare impulsive phase is attributed to the flare reconnection that adds poloidal magnetic flux to the flux rope and, at the same time, reduces the tension force from the overlaying constraining magnetic fields [155, 156]. (2) Acceleration of the flux rope that is due to momentum transferred from the upward-directed reconnection outflows. The highly bent post-reconnection field lines coming out of the diffusion region bear a large magnetic tension force and are accelerated to near the Alfvén speed [194]. After joining the flux rope and become "dipolarized," the upward-directed reconnection outflows transfer the momentum to the flux rope and facilitates its acceleration [245, 257, 124]. Although multiple models have been proposed to account for the initiation and acceleration of the flux rope, such as the loss of equilibrium model [155], tether-cutting reconnection model [185], breakout reconnection model [6, 129], the net change of the upward Lorentz force and/or the added momentum transfer due to the upward reconnection outflows are both related to the magnetic flux change due to the ongoing flare reconnection. Hence, a positive correlation between the flux rope acceleration and flare energy release is expected.

The level of electron acceleration, usually indicated by the intensity of nonthermal hard X-ray (HXR) and/or microwave emission, is also found to be correlated to the rate of the flare energy release. By measuring the photospheric magnetic field and ribbon expansion, Qiu et al. [203] inferred the rate of the magnetic flux change and reconnection electric field evolution during the impulsive phase of two two-ribbon flares, which are found to be temporally correlated with the microwave emission and the derivative of the SXR emission (as a proxy for HXR emission assuming the Neupert effect [191]). Adopting a similar method, Liu and Wang [158] analyzed 13 two-ribbon flares and found an anti-correlation between the average reconnection electric field and minimum overall photon spectral index from HXR observation. Temmer et al. [228] found that the local reconnection electric

field inferred from the ribbon expansion in Hα/UV observations is uneven along the direction of the magnetic polarity inversion line (PIL). The locations of the spatially resolved HXR footpoint sources were found to be spatially correlated with the local electric field. With the observation of the flare ribbon from the Interface Region Imaging Spectrograph (IRIS; De Pontieu et al. 55, Naus et al. [190] also revealed the strong correlation between the local magnetic flux change rate and the production of the nonthermal electrons inferred from RHESSI HXR data. These studies strongly suggest that the electron acceleration in flares and its temporal and spatial evolution are intimately related to the local electric field in the reconnection region.

Recent modeling studies have suggested that, in addition to the absolute magnetic energy release rate, the guide field, defined as the perpendicular magnetic field to the antiparallel reconnecting magnetic components, also plays a key role in determining the efficiency of particle energization. In particular, a strong guide field can suppress the acceleration of electrons to high energies, resulting in an overall soft spectrum [201, 51, 53, 151, 7]. At present, direct means of measuring the guide field in the reconnection region has not been available, although the present microwave imaging spectroscopy observations, made by the Expanded Owens Valley Solar Array (EOVSA; Gary et al. 84) have provided constraints of the guide field by comparing the overall magnetic field profile along the current sheet to model predictions [35][1]. Alternatively, the inclination angle of the post reconnection flare arcade, usually constrained by comparing the orientation of the conjugate ribbon brightenings with respect to the magnetic PIL, can be used as a proxy to infer the guide field component in the coronal region [e.g. 206]. Recently, using three-dimensional MHD simulations, Dahlin et al. [54] revealed a prominent decrease of the guide field over the impulsive phase of eruptive flares, conforming to the observational evidence reported by Qiu et al. [204].

[1]Prospects of achieving more direct measurements of the guide field can be realized by using microwave imaging spectropolarimetry.

However, the correlations discussed above have focused largely on the peak rates derived during the impulsive phases of the flare-CME events and are based on statistical studies of multiple different events. In this work, we will report a new finding that such a correlation is also present during the post-impulsive phases (PIP) of a single eruptive event. We also compare the difference in the geometry of the magnetic reconnection in two flare phases and its possible effects on flux rope acceleration and electron energization.

In Subsection 3.2.1, we review the event observed in multiple wavelengths and present the early evolution of the erupting flux rope. In Subsection 3.2.2, we present microwave and X-ray imaging spectroscopy observations and spectral analysis of the main- and post-impulsive phase bursts. In Subsection 3.2.3, we report measurements of the kinematics of the erupting magnetic flux rope. In Section 3.3, we interpret the observational results and discuss the implications, especially on the correlation between the flux rope acceleration, electron acceleration, and flare emission during the main- and post-impulsive phase.

3.2 Observations

3.2.1 Event overview

The C9.4-class event under study occurred on the east solar limb on 2017 August 20. The event was well observed in extreme ultraviolet (EUV) by the Atmospheric Imaging Assembly on board the Solar Dynamics Observatory (SDO/AIA; Pesnell et al. 195, Lemen et al. 149) and the Extreme UltraViolet Imager (EUVI; Wuelser et al. 256) onboard STEREO-A, one of the two Solar Terrestrial Relations Observatory (STEREO; Kaiser et al. 127) spacecraft. SDO/AIA observed the flare event near the east limb from the Earth's viewing perspective, while STEREO-A was $\sim$230° west from the Earth and provided observations from another viewing perspective (Figure 3.1). The Geostationary Operational Environmental Satellite (GOES) and the Reuven Ramaty High-Energy Solar Spectroscopic Imager (RHESSI; Lin et al.

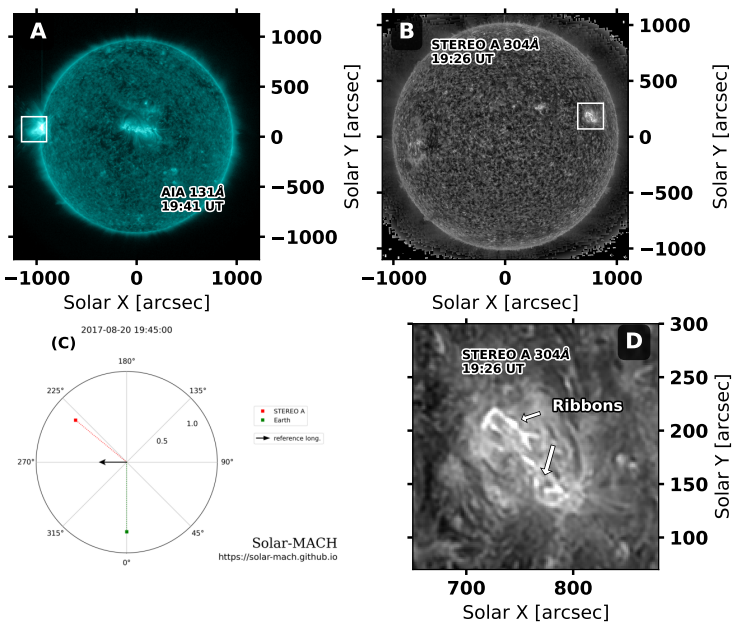

Figure 3.1 (a) The eruptive solar flare event under study as observed in EUV by the SDO/AIA 131 Å filterband on 2017 August 20 at 19:41:00 UT. The white box shows the FOV that is used in Figure 3.4. (b) The event as observed in STEREO/EUVI 304 Å at 19:26:00 UT, with an enlarged view shown in (d) (whose FOV is indicated by the white box in (b)). (c) Relative location of the STEREO-A spacecraft (red cube), the Earth/SDO spacecraft (green cube), and the longitudinal direction of the event in the frame of the HEE coordinate system (produced using the Solar-MACH software; Gieseler et al. 92).

157) had full coverage of the event in X-rays. Meanwhile, EOVSA observed the post-impulsive phase and the decay phase of the event in the microwaves from 1–18 GHz (Figure 3.2). It missed the main impulsive peak because the antennas went off the Sun for calibration during that time.

The event was associated with a white-light CME observed by the K-coronagraph of the Mauna Loa Solar Observatory (MLSO/K-Cor; Elmore et al. 67), as well as the Large Angle Spectroscopic COronagraph on board the Solar and Heliospheric Observatory (SOHO/LASCO; Brueckner et al. 27). Figure 3.3(a) shows a faint, slow ($\sim$250 km s^{-1}), and narrow ($\sim$32°) CME in the LASCO C2 difference image. In MLSO/K-Cor white light images, the CME, as shown in Figure 3.3(b), displays a typical three-part-structure: a leading front, a relatively darker cavity, and

a bright core, which are typically explained as the plasma pileup at the boundary of the erupting flux rope, flux rope, and filament/prominence, respectively [119, 42, 241]. However, based on multi-perspective observations, some recent studies point out that the observed bright core of the CME in white light can be attributed to the flux rope itself [113, 239, 218]. In addition, based on laboratory experiments, an alternative model has been proposed to interpret the cavity as a result of induced reverse current propelling the background plasma away from the core [**?**].

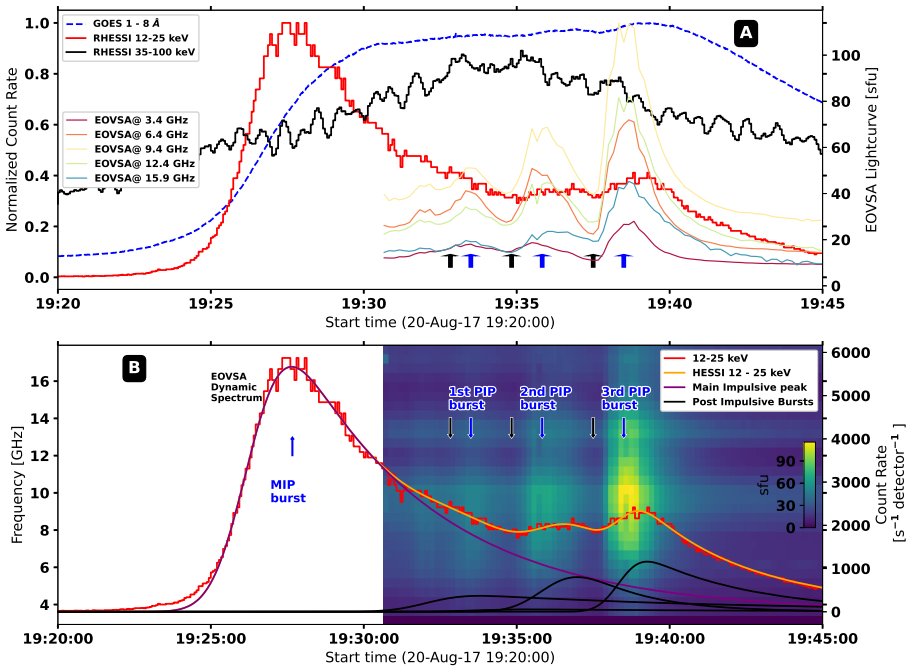

Figure 3.2 (a) RHESSI 12–25 keV X-ray (red curve), RHESSI 35–100 keV HXR (black curve), and GOES 1–8 Å soft X-ray (SXR) (blue dashed curve) light curves from 19:20 UT to 19:45 UT on 2017 August 20. Other color curves show EOVSA microwave flaring-region-integrated light curves at five selected frequencies (3.4, 6.4, 9.4, 12.4, 15.9 GHz) from 19:31 UT to 19:45 UT. The blue arrows indicate the peaks of the main-impulsive phase and the three post-impulsive phase bursts, while the black arrows indicate the corresponding pre-burst time of each burst used for background subtraction. (b) Smoothed RHESSI 12–25 keV X-ray (solid orange curve) decomposed into the main-impulsive phase burst (solid purple curve) and the three post-impulsive phase bursts (solid black curves). The light curve is fitted using four components described in the text. The background is the flare-region-integrated (same as that of the light curves in (a)) microwave dynamic spectrum from 19:31 UT to 19:45 UT.

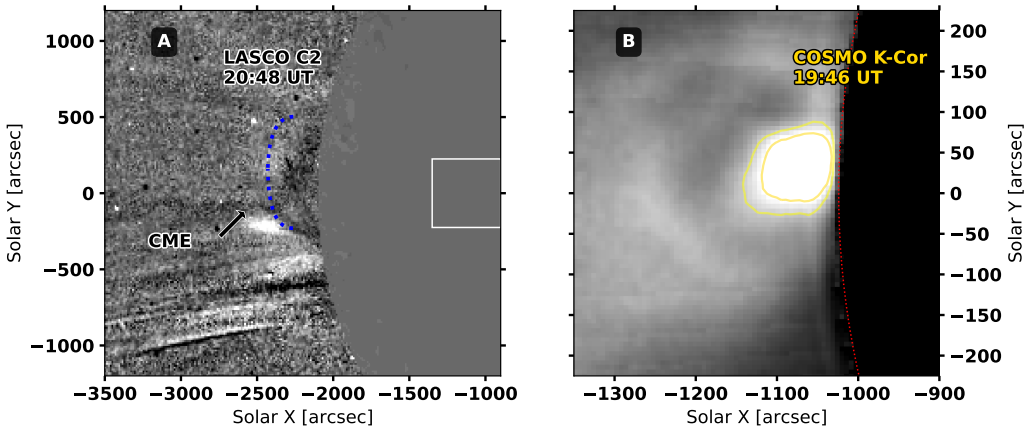

Figure 3.3 The associated CME observed in white light by MLSO/K-cor and SOHO/LASCO C2. (a) The narrow CME as observed in LASCO/C2 running-difference image at 20:48 UT (81 minutes after the flare peak), whose front is indicated by the black arrow and the blue dashed curve. The white box shows the FOV of the MLSO/K-cor image in (b). (b) The three-part-structure CME as observed in MLSO/K-cor white light image at 19:46 UT (19 minutes after the flare peak).

Before the flare, a dark filament can be clearly identified in the EUV passbands (Figure 3.4(a)). At 19:14 UT, two minutes before the HXR flux shows an early rise, two new loops appear in the SDO/AIA 131 Å images (highlighted by the yellow/orange dotted lines in Figure 3.4(b)). Four minutes later, at 19:18 UT, a flare arcade started to appear, which connected the two inner footpoints of the two loops (highlighted by the pink dotted lines in Figure 3.4(d)). Meanwhile, a new coronal structure also appears between the two loops (indicated by the white arrow in Figure 3.4(c) and (d)). The event enters the main impulsive phase at 19:24 UT (c.f., Figure 3.2(a)), when the flare arcade further developed and brightened. The viewing perspective of the STEREO-A/EUVI reveals two J-shaped flare ribbons in a typical two-ribbon configuration (Figure 3.1(d)). The bright coronal structure seen during the pre-impulsive phase disappeared when the event enters the post-impulsive phase (Figure 3.4(f)).

As the event entered the main-impulsive phase, a group of large-scale overlying loops, which bridged the northern and southern ends of the active region, started

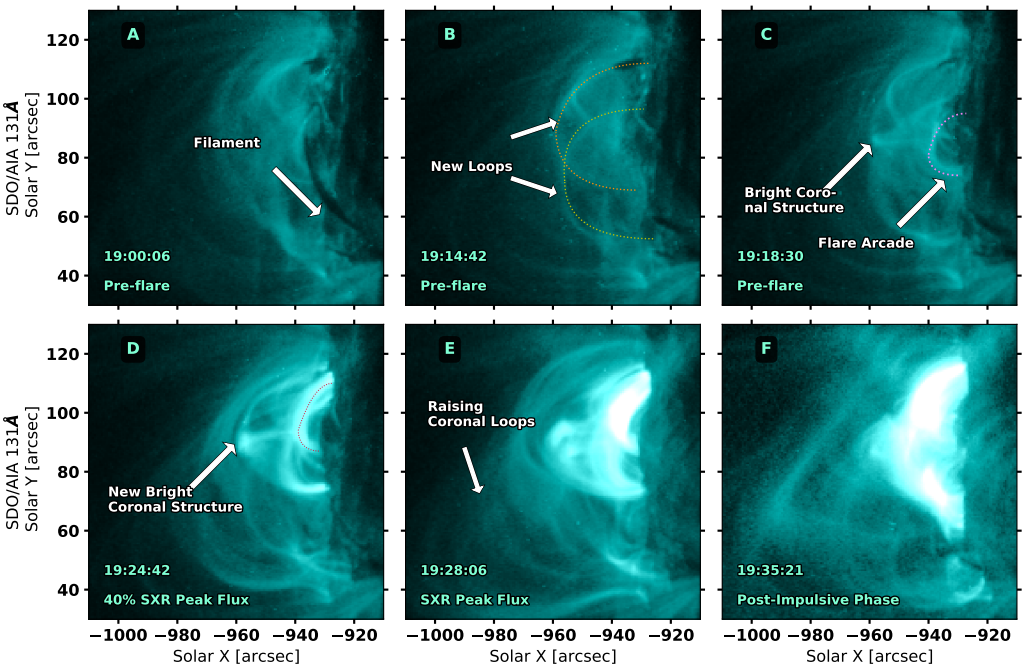

Figure 3.4 Close-up view of the coronal evolution as observed by SDO/AIA 131 Å from the pre-flare phase to the beginning of the post-impulsive phase. (a) The dark filament which exists before the event, marked by the white arrow. (b) The appearance of two loops during the pre-flare phase is highlighted by the yellow/orange dashed curves. (c) The newly formed coronal structure and the flare arcade (pink dashed curve) that appear as the result of a tether-cutting reconnection during the pre-flare phase (indicated by the white arrows). (d) The gradually brightening coronal structure and a flare arcade appear during the main-impulsive phase, indicated by the white arrow and red dashed curve, respectively. (e) and (f) An Enlarged view of the flare region at the SXR flare peak and the beginning of the post-impulsive phase, respectively.

to rise towards the southwest direction in succession (indicated by the white arrow in Figure 3.4(e)). The eruption started to appear clearly during the post-impulsive phase, when an oval-shaped cavity became visible in the SDO/AIA 131 Å images ((Figure 3.5(a))), which we interpret as the cross-section of the erupting magnetic flux rope.

To clearly show the evolution of the erupting cavity, in Figures 3.5(d)–(f), we show SDO/AIA 94 Å images enhanced with the multi-scale Gaussian normalization (MGN) method [186]. A kernel size of 4″.8 is selected to sharpen the edge and reveal

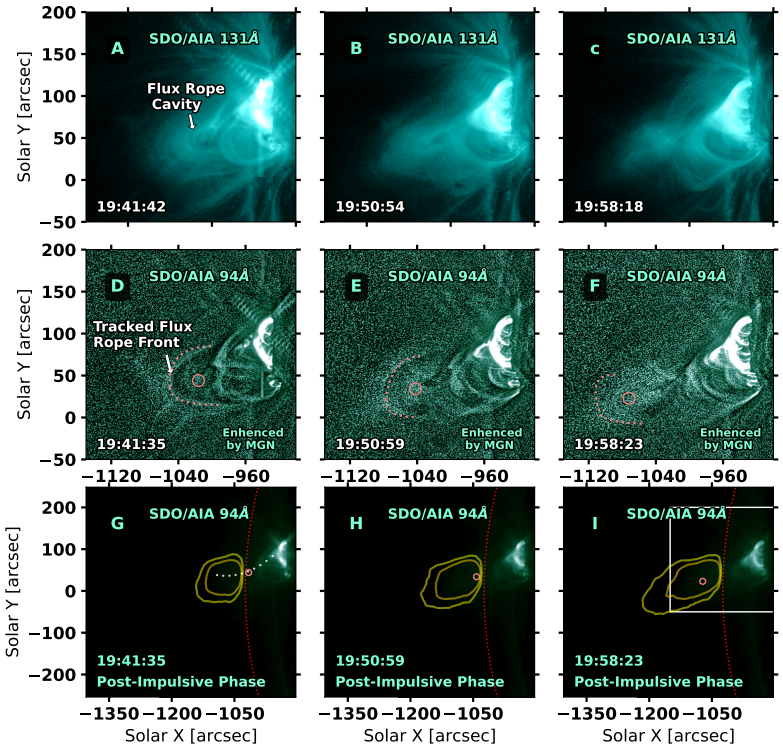

Figure 3.5 Evolution of the rising flux rope during the post-impulsive of the event as observed by SDO/AIA in EUV and MLSO/K-Cor in white light. (a)–(c) SDO/AIA 131 Å images showing the evolution of the erupting flux rope cavity, indicated by the white arrow in (a). (d)–(f) SDO/AIA 94 Å images enhanced with the MGN method. The overlying loop-like feature at the front of the cavity is indicated by the white arrow in (d) and the pink dashed curve in (d)–(f), while the center of the flux rope cavity is indicated by the pink open circle. (g)–(h) Contours of the MLSO/K-Cor white light images (the contour levels are same as that of Figure 3.3(b)) overlaid on SDO/AIA 94 Å images. The same pink open circles in (d)–(f) are also shown. The lower boundary of MLSO/K-Cor's FOV at 1.07 solar radii is indicated by the red dashed curve. The FOV that is used in (a)–(f) is shown as the white box in (i).

the loop-like structure at the front of the cavity. This loop-like structure will be used for measuring the kinematics of the eruption, which will be discussed in detail in Subsection 3.2.3.

When the cavity, whose center is indicated by the pink circle in Figure 3.5(D)–(I)), rises into the inner FOV of the MLSO/K-Cor at 1.07 $R_{\odot}$ (red dashed line in Figure 3.5(G)–(I)), it moves synchronously with the CME bright core in the MLSO/K-Cor white light images (the innermost contour in Figure 3.5(f), (g)). The synchronized

motion of the cavity center in SDO/AIA 94 Å images and the bright core of the K-Cor CME suggest that they represent a coherent erupting structure, most likely a magnetic flux rope.

3.2.2 Microwave and X-ray bursts during the main- and post-impulsive phase

Shortly after the impulsive X-ray peak at 19:27 UT, the event entered its post-impulsive phase. Almost at the same time, EOVSA went back to target (the Sun) at 19:31 UT and fully covered the post-impulsive phase. In this phase, three broadband bursts can be observed in the EOVSA 1–18 GHz dynamic spectrum (Figure 3.7(g)), which peak at 19:33 UT, 19:35 UT, and 19:38 UT respectively. The dynamic spectrum is produced by integrating the total flux of the flaring region using images integrated from 19:32 UT to 19:45 UT with 134 frequencies in 2.5–18 GHz over 31 evenly spaced spectral windows (referred to as SPW 0 to SPW 30). While post-impulsive phase microwave bursts have been reported in previous studies [e.g. 260, 136], this event shows an increase in the peak intensity of later bursts later. The peak flux density at, 9.4 GHz for example, increases from 50 sfu for the first burst to 114 sfu for the last one.

As shown in Figure 3.2, the bursts also have the response in GOES 1–8 Å SXR light curve and RHESSI 12–25 keV X-ray light curves. To investigate the relationship between the microwave and HXR bursts, we carried out a forward fitting on the RHESSI 12–25 keV light curve using a 'heating-decay" function following Gryciuk et al. [99]. For each burst, the time profile can be written as:

$$f(t) = \int_0^t g(t')h(t-t')\mathrm{d}t', \tag{3.1}$$

which is the result of a Gaussian-shaped pulse $g(t)$ convoluted with an exponential decay term $h(t)$. They are, respectively,

$$g(t) = g_0 \exp\left(-\left(t - t_0\right)^2 / 2\sigma^2\right) \tag{3.2}$$

and

$$h(t) = \exp(-Dt), \tag{3.3}$$

where g_0, t_0, σ, and D are the parameterized amplitude, peak time, the standard deviation of the distribution (0.42 time of the half-peak duration), and exponential decay coefficient, respectively.

The observed RHESSI 12–25 keV light curve is fitted with four pulses, which correspond to the main-impulsive peak and the three post-impulsive bursts, respectively. Similar to post-impulsive microwave bursts, RHESSI 12–25 keV X-ray bursts also show an increase in the peak intensity for later post-impulsive bursts, as shown in Figure 3.2.

X-ray imaging and spectral analysis We reconstruct the RHESSI 6–12 keV images using the `CLEAN` algorithm [117] with a 40 s integration time, based on measurements from detectors 1, 3, and 8. The X-ray sources are plotted as green open contours in Figure 3.7(a), (c)–(e). During the main-impulsive phase (Figure 3.7(a)), three sources can be distinguished. The main source is located at the top of the flare arcade. The lower (western) source coincides with the southern footpoint of the arcade, while the upper (eastern) source coincides with the bright coronal structure discussed in Subsection 3.2.1. During the post-impulsive phase, the upper X-ray source quickly fades away following the rise of its EUV counterpart, while the looptop and the footpoint sources remain. The detailed spatial evolution of the HXR source during the post-impulsive phase will be further presented and discussed in Subsection 3.2.4.

We utilize the `OSPEX` tool, which is part of the SolarSoft IDL package (`sswidl`; Freeland and Handy 78) distribution, to perform the X-ray spectral analysis. Due to the increasingly more severe pulse pileup effect that affected RHESSI X-ray measurements toward the end of its operations, we limited our spectral analysis to data obtained from detector 3. This particular detector, thanks to its low sensitivity at the time of observation, showed the least amount of pileup effect among all active detectors. For the X-ray spectrum at each impulse, we fit three components, which include a single-temperature thermal bremsstrahlung function (`vth`), a broken power-law (`bpow`) and a pseudo function that accounts for the pileup effect (`pileup_mod`), to the observed photon count rate spectrum. The fitting results for the three X-ray pulses are presented in Table 3.1, and the associated uncertainties are estimated using the built-in Monte Carlo module in `OSPEX`.

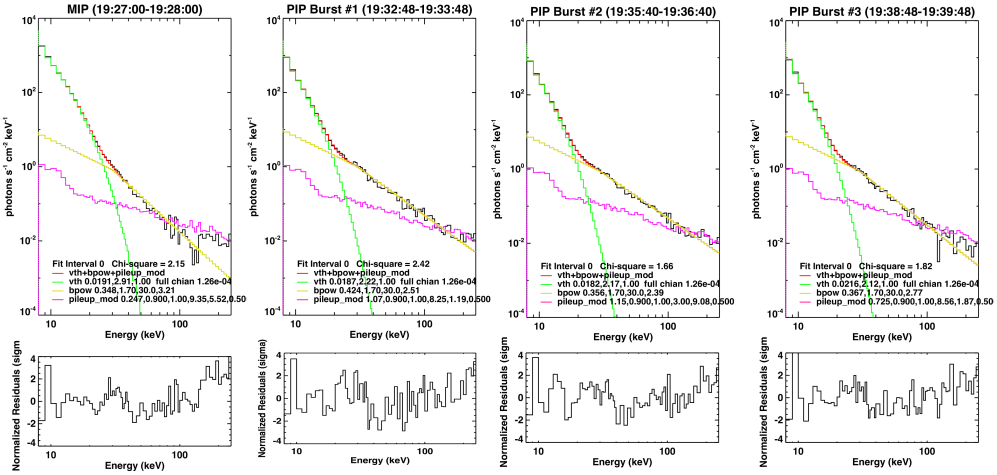

Figure 3.6 RHESSI photon flux spectra and spectral fitting results for the bursts during the main-impulsive phase (a) and the three post-impulsive phase burst (b)–(d). The key fit parameters are summarized in Table 3.1.

Interestingly, compared to the post-impulsive phase bursts, the nonthermal component during the impulsive phase derived from the RHSSI HXR spectra has a softer (larger) spectral index and a smaller normalization at 30 keV, despite having a much larger intensity at lower energies. Another piece of evidence of the less

	Emission Measure $[10^{49} cm^{-3}]$	**Plasma Temperature** $[keV]$	**Normalization at Epivot**	**Negative Power-law Index**
main-impulsive Phase	0.1910±0.0005	2.91±0.05	0.348±0.011	3.21±0.16
1st PIP Impulse	0.0187±0.0004	2.22±0.05	0.424±0.009	2.51±0.06
2nd PIP Impulse	0.0182±0.0002	2.17±0.06	0.356±0.010	2.39±0.09
3rd PIP Impulse	0.0216±0.0003	2.12±0.06	0.367±0.008	2.77±0.09

Table 3.1 RHESSI X-ray spectral fitting results at the main-impulsive phase and the three post-impulsive phase bursts. The two-sigma uncertainties are estimated by running the built-in Monte Carlo analysis in OSPEX.

prominent electron energization during the main-impulsive phase is that the RHESSI 35–100 keV light curve, shown as the black curve in Figure 3.2(a), peaks during the post-impulsive phase. Although the EOVSA microwave nonthermal electron diagnosis is unavailable during the main-impulsive phase and HXR diagnostics is complicated by the pile-up effects, the results of the HXR spectral analysis are consistent with a less prominent nonthermal electron component during the main-impulsive phase than the post-impulsive phase.

Microwave imaging spectroscopy EOVSA missed the main-impulsive phase of the event but had full coverage of the post-impulse phase. Figure 3.7(b) shows EOVSA microwave images as open contours (50% of the maximum brightness at each frequency) at 19:32 UT just before the first post-impulsive phase burst. At high frequencies, the microwave source is concentrated on the northern part of the flare arcade. The sources extend from north to south (southeast in the viewing perspective of STEREO-A/EUVI images) and align with the ridge of the post-flare arcades. The microwave sources evolved rapidly during the peak time of each post-impulsive burst. To better reveal their evolution, we performed difference imaging against the pre-burst background time, with the selected background times pointed by the black arrows in Figure 3.2. The difference imaging results for the peaks of the three bursts (blue

arrows in Figure 3.2) are shown in Figures 3.7(c), (d), and (e), respectively. To avoid doing the non-linear synthesis imaging two times as in the case of image-plane-based difference imaging, the image subtraction is done in the visibility domain before performing synthesis imaging. We also evaluated the stability of the sources used as the background. They show very similar morphology as that shown in Figure 3.7(b).

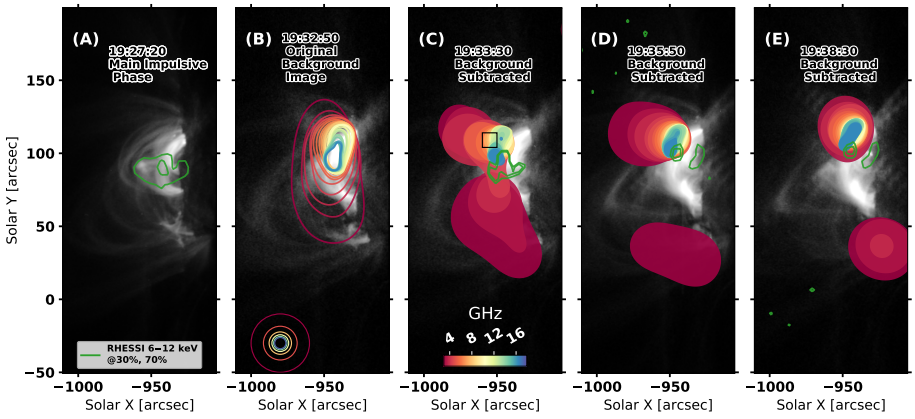

Figure 3.7 EOVSA multi-frequency microwave images and RHESSI 6–12 keV sources during the main impulsive phase and the three post-impulsive bursts. (a) RHESSI 6–12 keV source at the peak of the main-impulsive phase. The contour levels are 30% and 70% of the maximum. (b) Multi-frequency microwave images at the background time just prior to the first post-impulsive burst (the time is indicated by the first black arrow in Figure 3.2). The open contours are at the level of 50% of the maximum brightness at each frequency. The restoring beam size of each frequency is shown in the bottom left corner. The microwave source morphology at all the selected background times prior to the three post-impulsive bursts is similar to each other. (c)–(e) Background-subtracted multi-frequency microwave images at the peak of the three post-impulsive bursts (indicated by the three blue arrows in Figure 3.2). The level of the filled contours is as same as that of open contours in (b). The background gray-scale images are from SDO/AIA 131 Å at the corresponding times.

The background-subtracted microwave sources during the peak of the three post-impulsive bursts are mainly located above the top of the bright post-flare arcades seen in SDO/AIA 131 Å. For bursts 2 and 3, the above-the-looptop microwave source shows an obvious dispersion in height, with the high-frequency source located lower than the low-frequency ones. Such a microwave source morphology has already

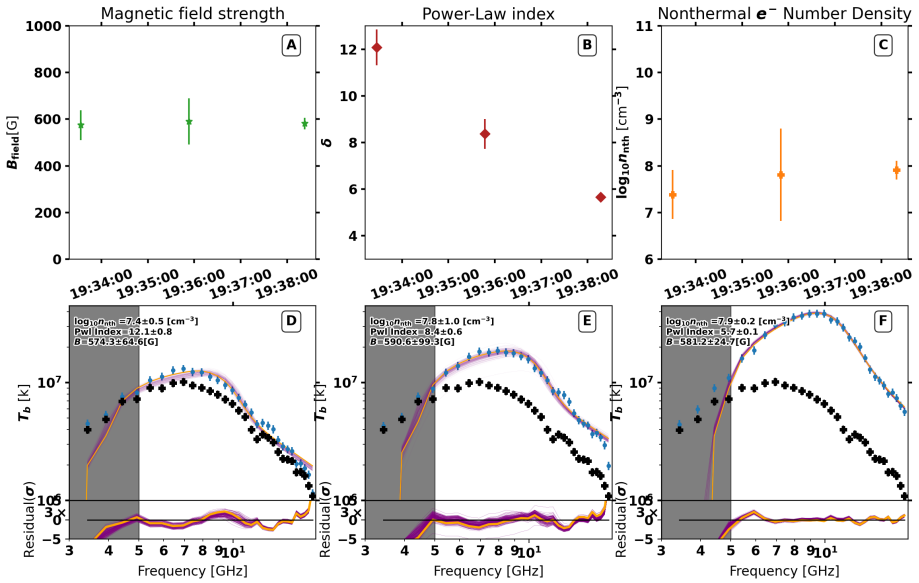

Figure 3.8 Microwave spectra derived from the above-the-loop-top (ALT) region during the three post-impulsive bursts and corresponding spectral fitting results. (a)–(c) The evolution of the best-fit values of magnetic field strength B, power-law index of the electron energy distribution δ', and total nonthermal electron density $n_{\rm nth}$ above 20 keV, respectively. (d)–(f) EOVSA microwave brightness temperature spectra (blue dots) at the above-the-loop-top region during the post-impulsive phase bursts. The solid orange curve shows the best-fit results while the solid purple curve is the distribution of the MCMC runs within 1-σ of the median MCMC values. The corresponding residuals are shown at the bottom of each panel.

been reported by Gary et al. [84], Chen et al. [37] for the early impulsive phase of the X8.2 solar flare on September 10, 2017. The source dispersion above the looptop was interpreted as the signature of nonthermal electrons distributing along the reconnection current sheet, with the higher frequency source generally originating from sources regions with a greater magnetic field strength. During the peak of the three post-impulsive bursts, a southern low-frequency source (<5 GHz) appears to the south of the above-the-looptop source. The source is identified as the microwave counterpart of the southern footpoint of the flux rope. Figure 3.8(d)–(f) shows the brightness temperature spectra from the above-loop-top (ALT) region (black box in Figure 3.7(c)) at the peak time of each post-impulsive phase burst (blue dots with error bars). The spectra show characteristics of the nonthermal gyrosynchrontron

radiation [65]. Therefore, we fit the observed spectra using a nonthermal gyrosynchrontron radiation model from a homogeneous source with a power-law electron energy distribution based on the fast gyrosynchrotron codes developed by [70]. Three free parameters are used in the spectral fitting: magnetic field strength B, the total number density of nonthermal electrons $n_{\rm nth}$, and the power-law index δ' of the nonthermal electron energy distribution ($f(\varepsilon) = dn_{\rm nth}(\varepsilon)/d\varepsilon \propto \varepsilon^{-\delta'}$). The energy range of the nonthermal electron distribution is fixed to 20 keV–10 MeV. The thermal electron density $n_{\rm th}$ and the plasma temperature T is fixed to 1.7×10^{11} cm^{-3} and 13 MK, respectively. They are derived using differential emission measure (DEM) analysis within the source region, based on measurements by six SDO/AIA EUV channels (94, 131, 171, 193, 211, and 335 Å) using the technique by Hannah and Kontar [104]. The column depth is assumed to be $13''$ based on the observed source size on the plane of the sky at 6.4 GHz.

The best-fit spectra and the corresponding residual are shown as the thick solid orange curves in Figures 3.8(d)–(f). Following Chen et al. [35], we adopt the Markov Chain Monte Carlo (MCMC) method to estimate the uncertainties of the parameters and verify that we have achieved global minimization in the multi-dimensional parameter space. The spectra calculated from the MCMC samples and the corresponding residuals are shown as thin purple curves in Figures 3.8(d)–(f). Figures 3.8(a)–(c) show the temporal evolution of the three fit parameters at the peak time of each post-impulsive phase microwave burst. The corresponding errors are estimated by the MCMC method. Of the three fit parameters, the only one that undergoes a significant change (against the uncertainties) is the power-law index of the nonthermal electron energy distribution δ'. The power-law index shows a large hardening for later post-impulsive microwave bursts, which increases from ~ 12 of burst #1 to ~ 5.5 of burst #3.

The brightness temperature spectra in the background are plotted as the black crosses in Figure 3.8(a)–(c). Spectral analysis indicates that the source is dominated by thermal emission. This thermal loop-top source is very similar to that reported by Yu et al. [260] for the post-impulsive phase of the X8.2 solar flare on September 10, 2017.

3.2.3 Magnetic flux rope kinematics

To accurately track the kinematics of the erupting magnetic flux rope seen in SDO/AIA images in the low corona and the associated white-light CME observed in MLSO/K-Cor images, we obtain a time-distance stack plot by obtaining the intensity along a slice shown as the dashed white lines in Figure 3.5(e). The slice crosses the boundary of the FOV of SDO/AIA and extends to that of the MLSO/K-Cor. The eruption changes its course slightly during its ascent. Hence the slice is slightly bent toward the direction of the flux rope eruption. The width of the slice increases linearly from 3″ at the bottom to 13.8″ at the top to compensate for the general expansion of coronal structures. In order to clearly show the dynamic features, we also apply the running-differential method on the SDO/AIA 94 Å and MLSO/K-Cor white light images and then enhance the edge of those features with a high-pass filter technique.

The resulting time-distance stack plot is shown in Figure 3.9. A number of rising tracks are visible at different heights, which correspond to not only structures that correspond to the core of the erupting magnetic flux rope, but also the overlying loops that enclose the flux rope cavity. We select one of the most visible tracks at the immediate front of the erupting cavity-like structure to measure the kinematics of the flux rope. The selected track is denoted by the red symbols in Figure 3.9(a) and the corresponding feature in the difference images are marked by pink dashed curves in Figure 3.5(g)–(i). At any given time, the height of the tracked feature is determined by finding the peak in the intensity–height profile. To estimate the uncertainty of the

tracked trajectory, we fit a skewed Gaussian function to the intensity–height profile around the peak. The full width at half maximum of this Gaussian function is used as an estimate of the uncertainty, shown as the vertical extension of the red symbols in Figure 3.10(a). A similar time-distance stack plot is derived using the MLSO/K-Cor images at the same selected slice, shown in the upper portion of Figure 3.10(a). It can be seen that the trajectories of the cavity front tracked in the SDO/AIA images and the upper edge of the white light CME core seen by MLSO/K-Cor are well aligned, which demonstrates that we are tracking a coherent flux rope structure erupting from the low to middle corona.

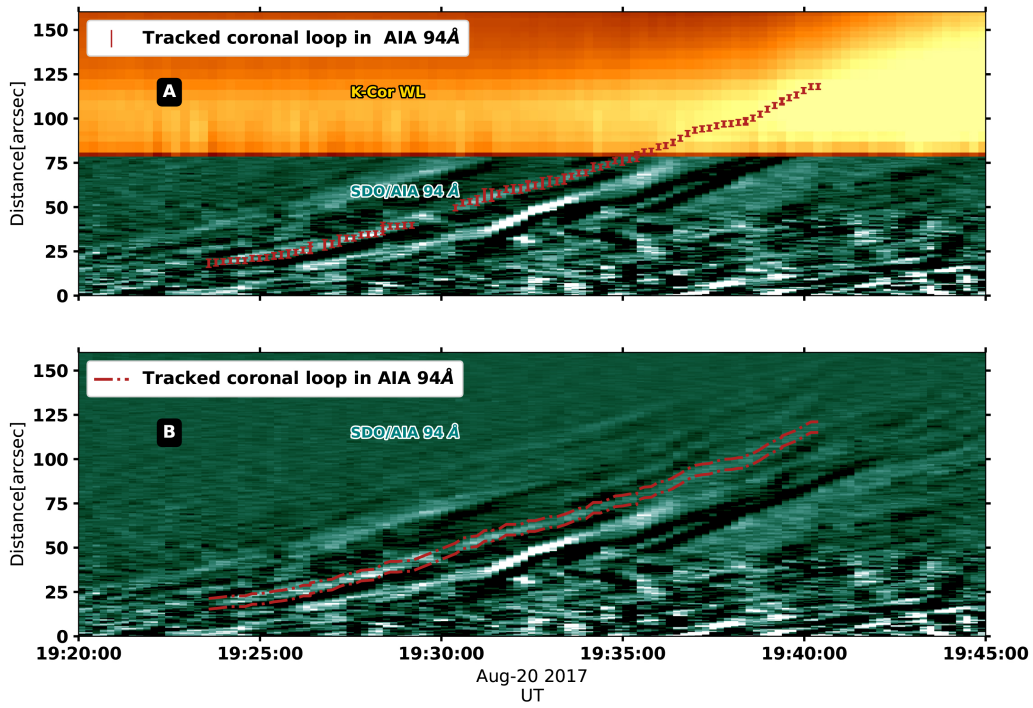

Figure 3.9 (a) Time–distance stack plot of MLSO/K-Cor white light (upper) and SDO/AIA 94 Å (lower; background-detrended) images series made along a slice as indicated by the dashed white curve in Figure 3.5(e). Red symbols indicate the tracked eruption feature that represents the flux rope front. The vertical lengths of the symbols indicate the corresponding uncertainties. (b) Same as (a) but shows the complete time–distance stack plot of the SDO/AIA 94 Å image series. The trajectory of the tracked feature is sandwiched between the red dashed-dotted lines. An accompanying video (Animation **??**) shows the tracked feature on the SDO/AIA 94 Å background-detrended images and the corresponding time–distance plot.

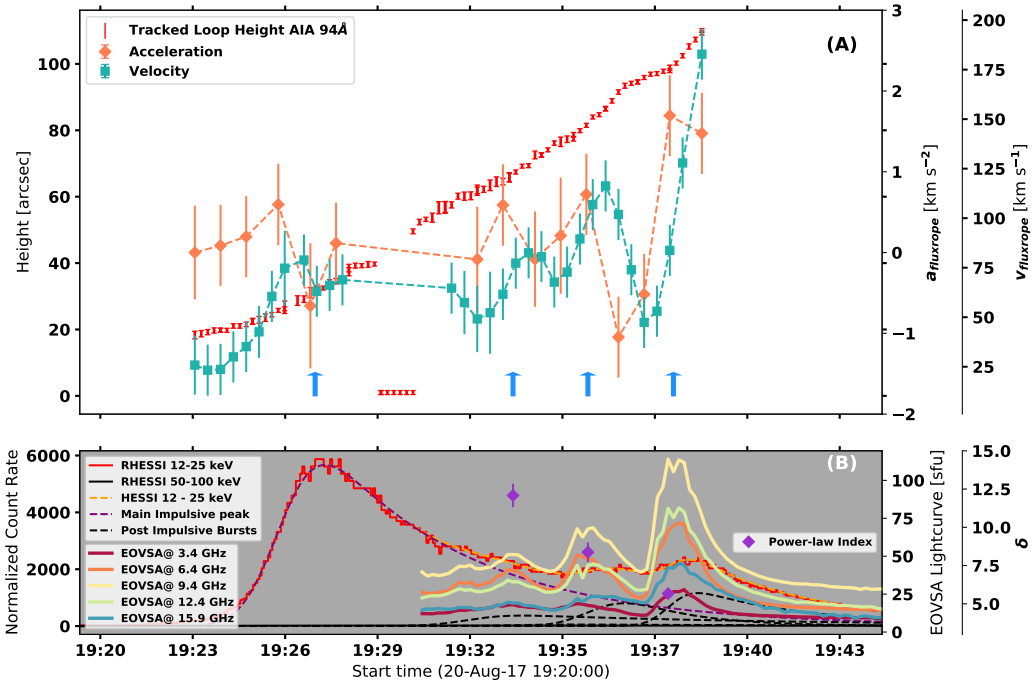

Figure 3.10 (a) Evolution of the height (red symbols), velocity (green symbols), and acceleration (orange symbols) of the erupting flux rope during the main- and post-impulsive phase. The peak time of the main- and post-impulsive phase bursts are indicated by the blue arrows. (b) Microwave and X-ray light curves during the same period (similar to Figure 3.2(b) but with the EOVSA microwave light curves shown instead). Also shown are the microwave-constrained power-law index of the nonthermal electron distribution at the peaks of the three post-impulsive phase bursts (purple symbols).

The speed and acceleration that are derived from the height–time profile (red symbols) are denoted by the light green and light orange symbols, respectively. When estimating the error in the first- and second-order derivative (velocity and acceleration), in addition to the error propagated from the height measurement itself, we include the truncation error to describe the error introduced by smoothing the height measurement. The acceleration of the flux rope in this event extends to and peaks at the post-impulsive phase. As shown in Figure 3.10(a), three clear acceleration processes can be identified from 19:30 UT to 19:40 UT during the post-impulsive phase (Figure 3.10(a)). Interestingly, each acceleration episode coincides in time with a post-impulsive phase microwave/X-ray burst. In addition, as shown

in Figure 3.10, later post-impulsive bursts, which feature stronger microwave/X-ray flux and a harder electron energy spectrum, correspond to a larger peak acceleration value (purple symbols in Figure 3.10(b) and Figure 3.8(b)). However, the relation in the main-impulsive phase does not follow the same trend as in the post-impulsive phase. The maximum count rate of the RHESSI 12–25 keV time profile at the main-impulsive phase is 16 times larger than that at the first post-impulsive phase, while the corresponding maximum acceleration values are similar.

3.2.4 Source motion at flare looptops and footpoints

During the post-impulsive phase, we also observed a synchronized motion of various energy release signatures above the flare looptops and at the footpoints. First, as shown in Figure 3.7(c)–(e), despite the dispersion in height (largely in the east–west direction) as a function of frequency, the background-subtracted microwave source from post-impulsive bursts #1 to #3 displays an evident systematic motion from the southern to northern side of the flare arcade. To better demonstrate the overall motion of the microwave source, in Figure 3.11(a), we show the centroid locations of the corresponding microwave sources as filled color circles. The centroid locations at each frequency are estimated by fitting the corresponding background-subtracted microwave source to a two-dimensional Gaussian ellipse using CASA task `IMFIT` [176]. The locations shown in the figure are obtained by averaging the centroid locations derived from individual images in 6.4–14.4 GHz. The uncertainties are determined by the standard deviation of the image source centroids across the frequency range.

Similarly, both the centroid location of the RHESSI 6–12 keV X-ray looptop source and the looptop EUV brightening show a northward trend during the three post-impulsive bursts. In Figure 3.11, the open circles mark the centroids of the RHESSI 6–12 keV source during the main-impulsive phase (red) and the post-impulsive phase bursts (the color code is as same as the microwave circles), with

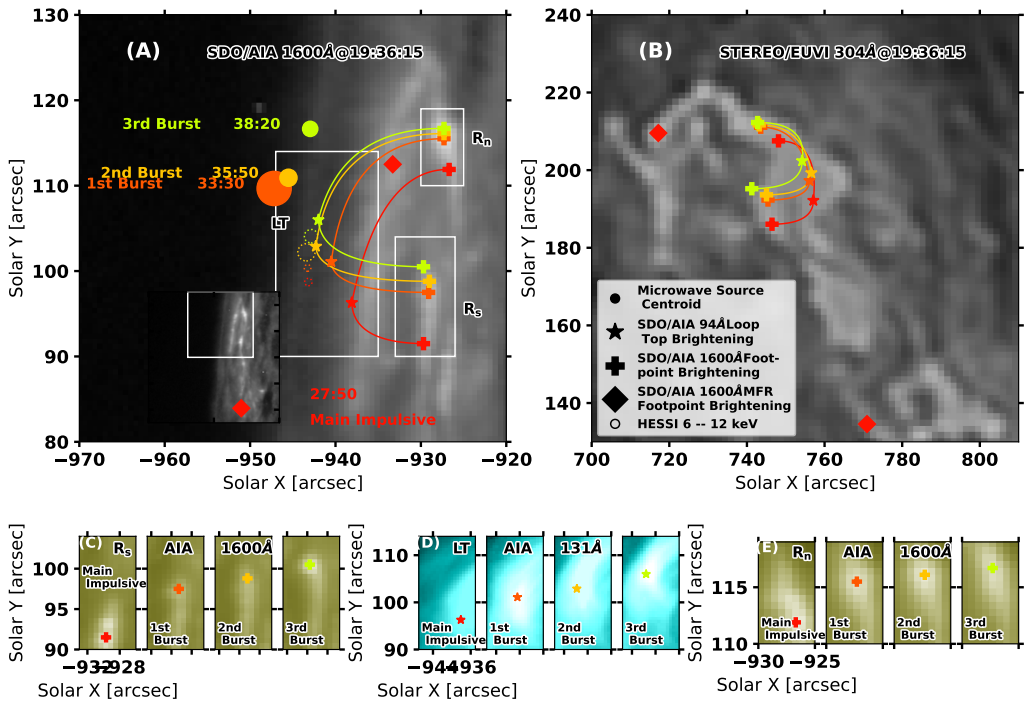

Figure 3.11 Synchronized northward motion of the microwave/X-ray/EUV looptop sources and corresponding UV footpoint brightenings. (a) Centroid locations of background-subtracted EOVSA microwave sources (filled circle), RHESSI 6–12 keV X-ray looptop sources (dashed open circle), EUV looptop brightening observed by SDO/AIA 131 Å images(stars). Also shown are the northern (R_n)/ southern (R_s) ribbon brightenings in SDO/AIA 1600 Å UV images (crosses) at the peak time of three post-impulsive bursts. The symbols are color-coded by time, as written in (a). The uncertainties of the microwave and X-ray sources are indicated by the radius of the corresponding filled/open circle. (b) Same as (a), but all the measured locations in (a) are re-projected into STEREO-A/EUVI's viewing perspective. (c)–(e) Detailed view of the northern ribbon region (R_n; c), flare looptop (LT; d), and southern ribbon region (R_s; e) at the peak time of the main impulsive phase and the three post-impulsive bursts. The corresponding FOV are indicated by the white boxes in (a).

their sizes corresponding to the uncertainties. The centroid location of the X-ray sources and their uncertainties are determined using Detector 3 images made with the `VIS_FWDFIT` algorithm. Meanwhile, the star symbols in Figure 3.11(a) represent the locations (pixels) of the brightest SDO/AIA 131 Å emission in the looptop region (within the box labeled "LT") at the corresponding times. The star symbols are also plotted in the SDO/AIA 131 Åimages in Figure 3.11(d).

The synchronized northward motion as observed in the looptop region is also observed at the conjugate footpoints of the post-flare arcade. In Figure 3.11(a), the straight ends of the two ribbons are enclosed in the white boxes with "R_n" and "R_s". The crosses are selected from the brightest point in SDO/AIA 1600 Åwithin the corresponding FOV at the corresponding time. The corresponding images are shown in Figure 3.11(c), (e). Similar to the coronal emissions, the conjugate footpoints have a unidirectional northward motion.

During the main-impulsive phase, UV brightening is also observed in the hook regions of the ribbons. The locations are shown as red diamonds in Figure 3.11. The southern hook region is plotted in the left-bottom corner plot in Figure 3.11(a), in which the original FOV of Figure 3.11(a) is shown as the white box.

The STEREO-A/EUVI images provide further confirmation of the locations of the footpoint brightenings. In Figure 3.11(b), we show the same ribbon brightnenings identified in SDO/AIA 1600 Å images reprojected to STEREO-A/EUVI's viewing perspective (color cross symbols). For the re-projection, we have assumed that the footpoint brightnenings occur at a chromospheric height of 1000 km (the solar radius $R_\odot$ used in the re-projection is 695.66 Mm [102]). Re-projection of the flare arcades seen by SDO/AIA is less straightforward owing to their unknown heights. For illustration purposes, in Figure 3.11(b), we show re-projected flare arcades and the looptop EUV brightenings at the respective times in STEREO-A/EUVI's view, by assuming that all the flare arcades stand vertically above the solar surface.

The unidirectional motion of the conjugate footpoints during the post-impulsive phase also implies a varying inclination angle of the post-reconnection flare arcade with respect to the PIL. However, as the event is close to the limb from SDO's viewing perspective and the unavailability of magnetic field measurements by STEREO-A, a direct determination of the PIL is not possible. In Figure 3.12(b), we use the rough mid-point location between the parallel portion of the two ribbons seen by STEREO-

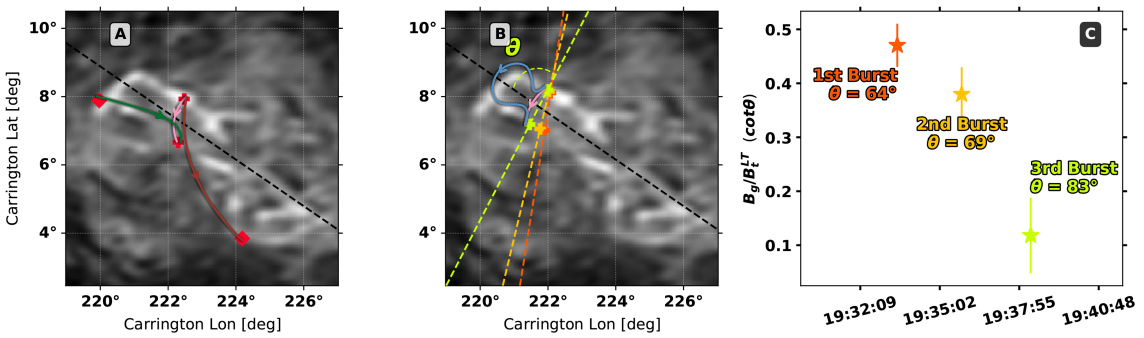

Figure 3.12 (a) Reconnection geometry and the inclination angle during the main impulsive phase. The images are the STEREO-A/EUVI 304 Å image at 19:06 UT re-projected to the heliographic Carrington coordinates. The red crosses show the represented locations of the footpoint brightenings (similar to Figure 3.11(b)). The dashed black line shows the estimated location of the polarity inversion line (PIL). The solid green and red curves demonstrate the pre-reconnection field lines, while the solid pink line shows the post-reconnection arcade. (b) Same as (a), but demonstrating the reconnection geometry (the pre-reconnection field line is demonstrated by the blue curve) and the inclination angle during the three post-impulsive phase bursts. (c) Evolution of the inclination angle θ during the three post-impulsive bursts and the corresponding normalized guide field estimates B_g/B_t^{LT}. The color code in (b) and (c) follows Figures 3.11.

A/EUVI as a proxy for the PIL (shown as a black dashed line). Then, we use straight lines that connect the three pairs of conjugate footpoint brightenings during the post-impulsive phase (shown in Figure 3.12(b) as the orange, yellow, and green dashed lines, respectively, for bursts #1, #2, and #3) to represent the orientations of the post-reconnection field lines. It can be seen that the lines connecting the post-impulsive footpoints become more and more perpendicular to the PIL as the flare progresses, indicating a smaller and smaller shear between the reconnecting magnetic field lines. In order to quantify the evolution of the normalized guide field, following Qiu et al. 204, we define the inclination angle θ as the sharp angle between the post-reconnection arcade and the PIL. The inclination angle θ can be used to estimate the normalized guide field: $R_g = B_g/B_t^{LT} \approx \cot\theta$, where B_g and B_t^{LT} are the guide field (parallel to the PIL) and the transverse component (perpendicular to the PIL) of the magnetic field at the looptop region, respectively. In Figure 3.12(c),

we show the evolution of the inclination angle θ and R_g during the post-impulsive bursts. The θ value increases from 64° during the first burst to 83° during the last burst, demonstrating an increasing shear[2].

In the main-impulsive phase, estimating the shear and the guide field is not as straightforward. However, we can use the observed ribbon brightenings and coronal loops to constrain the reconnection geometry. The pre-reconnection loops during the main-impulsive phase, illustrated as the red and green curves in Figure 3.12(a), correspond to the two loops highlighted in Figure 3.4(b) observed by SDO/AIA 131 Å. The post-reconnection arcade, displayed as the pink solid arcade in Figure 3.12(a), corresponds to the arcade in SDO/AIA 131 Å outlined by a pink dashed curve in Figure 3.4(c). The outer footpoints of the two pre-reconnection loops located in the hook regions of the ribbons are indicated by a pair of red diamonds in Figure 3.12(a), and the inner footpoints are shown by a pair of red crosses. In contrast to the post-impulsive phase in which the reconnecting field lines are nearly anti-parallel to each other, the reconnecting loops during the main impulsive phase likely have a very small inclination angle ($\theta \ll 45°$), suggestive of a much greater shear or guide field component.

3.2.5 Summary of the observations

The main observational phenomena are summarized as follows:

- The eruptive flare features three post-impulsive bursts in both microwaves and X-rays. Imaging reveals that the source is located at and above the top of the post-flare arcade.

[2]A larger θ value means a smaller shear. In particular, $\theta = 90°$ corresponds to the case in which the reconnecting field lines are completely anti-parallel to each other, while $\theta = 0°$ corresponds to purely parallel field lines.

- The power-law index δ' of the nonthermal electron energy distribution diagnosed using the microwave data at the ALT region shows a remarkable hardening for later post-impulsive bursts.

- The time evolution of the erupting flux rope features a short episode of acceleration during each of the post-impulsive bursts. The later ones appear to the stronger.

- A synchronized northward motion of the microwave/X-ray/EUV looptop source and UV footpoint brightening is observed during the post-impulsive phase.

- The inclination angle of the flare arcades with respect to PIL, inferred by the UV brightening on the flare ribbons, shows an increase for later post-impulsive bursts. In other words, the shearing decreases during the post-impulsive phase.

- The flux rope has a stronger acceleration during the post-impulsive phase than the main-impulsive phase. The X-ray power-law index during the post-impulsive bursts is also harder than that during the main impulsive phase.

3.3 Discussion and Conclusions

Our observation reveals a positive correlation between the microwave electron spectral hardness diagnosed by EOVSA microwave imaging spectroscopy and the acceleration of the associated flux rope in multiple microwave/X-ray bursts during the post-impulsive phase of a single eruptive flare event. The observation resembles the widely observed temporal correlation between the CME acceleration and the hard X-ray flux (or SXR derivative) in previous studies [e.g. 263, 203, 125, 172, 229]. However, most, if not all, of the previous reports were made during the main-impulsive phase of eruptive flares. In stark contrast, the main-impulsive phase of our event does not correspond to the strongest flux rope acceleration compared to its post-impulsive

counterpart. Coincidentally, despite featuring a brighter flare emission in X-rays, the main-impulsive phase has a softer X-ray spectrum than the post-impulsive phase.

To interpret these observed phenomena in the context of the eruptive flare, Figure 3.13 places the various observed features into the flare context for the pre- and main-impulsive phase (panels (a) and (b)) and the post-impulsive phase (panels (c) and (d)). During the pre- and main-impulsive phases, two highly sheared magnetic field lines (red and green solid curves in Figure 3.13(a), (b)) reconnect with each other in a "tether-cutting" fashion, with their inner footpoints coincide with the ribbon brightenings. After the reconnection, one set of the overlying, highly sheared post-reconnection field lines (upper solid pink line) join the flux rope, and the other set of lower-lying field line become the bright flare arcade (lower solid pink line). The released energy from the reconnection results in heating of both the flux rope and the flare arcade, which are observed as the bright coronal structure and the flare arcade seen in EUV (Figure 3.4(d)).

The heating and associated electron acceleration during this period may be also responsible for the observation of the multiple RHESSI 6–12 keV sources at the bright coronal structure, the looptop, and footpoint (Figure 3.7(a)). We conclude that the observations during the pre- and main-impulsive phase are broadly consistent with the tether-cutting reconnection scenario (see, e.g., Chen et al. 41, for similar observations), which may also contribute to the slow rise motion of the magnetic flux rope.

During the post-impulsive phase, the reconnection geometry represents that of the standard scenario for eruptive flares, in which the overlying magnetic fields reconnect below the flux rope and form a large-scale current sheet. In line with suggestions made in other studies [235, 8**?** , 122, 206] that expand the essentially two-dimensional standard flare model to three dimensions, our observation of a synchronized northward motion of the microwave/X-ray/EUV looptop source and the

UV footpoints favors a scenario in which the flux rope erupts in a zipper-like fashion. In this scenario, the primary reconnection site moves parallel to the ribbon. The motion is considered as a result of asymmetric flux rope eruption, which is usually caused by an asymmetric external magnetic confinement [e.g. 235, 163, 159, 268]. This "zipper-like" reconnection is considered as the main reason for multiple episodes of burst observed in multi-wavelengths.

We argue that the observed kinematics of the erupting flux rope is also consistent with the two reconnection scenarios during the pre- to post-impulsive phase of this event. The flux rope starts to accelerate right after the event enters the main-impulsive phase. Compared to that in the post-impulsive phase (especially bursts # 2 and 3), the increase in acceleration during the main-impulsive phase is relatively insignificant (Figure 3.10). In contrast, the acceleration shows a clear increase when entering each post-impulsive phase burst. In a typical eruptive flare, the kinematic evolution of the flux rope usually starts with a slow-rise phase followed by an impulsive acceleration phase [263].

The slow-rise phase is often found to have an approximately linear height-time profile, and the process is usually attributed to the tether-cutting reconnection scenario [220, 215, 48]. By contrast, the fast-rise phase is often attributed to either runaway reconnection [221] or positive feedback from the fast flare reconnection below the flux rope [155, 48, 167, 124]. We argue that the differences we observe in the main- and post-impulsive phase in the flux rope acceleration are generally similar to those that distinguish the slow- and fast-rise phase in other eruptive flares.

Similar to the previous studies, we attribute the acceleration of the flux rope to the positive feedback from the reconnection occurring in the current sheet trailing the flux rope. However, rather than a dominating driver in a main reconnection current sheet that gives rise to a prominent acceleration period, in our event, the driver is intermittent because of the zipper-like reconnection scenario. The rise of the flux rope

is likely asymmetric. It propagates from the active leg on the southwestern side to the anchored leg on the northeastern side (Figure 3.13(c) and (d)). Accordingly, the reconnection proceeds from southwest to northeast in an intermittent fashion [see, e.g., 163], driving the multiple acceleration episodes during the post-impulsive phase.

Now we turn our attention to the energization of nonthermal electrons during the main- and post-impulsive phase. As shown in Figure 3.6 and Table 3.1, the power-law index of the observed X-ray spectrum during the main-impulsive phase seems much larger (softer) than that during the post-impulsive phase despite having a bright flare emission at <30 keV.

Different from the reconnection scenario in a large-scale current sheet trailing the erupting flux rope in the post-impulsive phase, the tether-cutting geometry during the impulsive phase involves reconnection between magnetic loops with a much greater shear [184, 185] (Figure 3.12(a)). It implies the (normalized) guide field in the main-impulsive phase is also much greater, although, as discussed in Section 3.2, the guide field can not be estimated in the same way as in the post-impulsive phase. Nevertheless, we argue that the implied much greater guide field may be responsible for the low productivity of nonthermal electrons during the main impulsive phase according to recent theoretical and modeling studies [53, 151, 7, 202].

For the post-impulsive phase bursts, with the diagnosis using EOVSA's microwave imaging spectroscopy, we find that the power-law index δ' of the nonthermal electron energy distribution shows a remarkably harder electron spectrum for later post-impulsive bursts. The hardening of the electron energy spectrum coincides with an increasing acceleration of the flux rope during these post-impulsive bursts. Previous observational and modeling studies have suggested that, when the eruption is well underway, the flux rope acceleration serves as an excellent proxy for the rate of magnetic energy release via reconnection. Therefore, we attribute the hardening of the nonthermal electron spectra to an increasing magnetic energy

release rate which, in turn, facilitates the acceleration of nonthermal electrons to higher energies. We also note that the inclination angle θ of the post-flare arcade with regard to the PIL appears to increase throughout the post-impulsive bursts (Figure 3.12(b)). Such a change implies a smaller shear of the reconnecting magnetic field and a decreasing guide field. We argue that such a decreasing guide field component also contributes to the hardening of the nonthermal electron spectra.

In summary, we have presented an eruptive flare event that features three post-impulsive X-ray and microwave bursts immediately following its main impulsive phase. We have investigated the relationship between the flux rope acceleration and the electron energization in the context of the flare geometry and its evolution. We have found a positive correlation between the flux rope acceleration and electron energization during the post-impulsive phase bursts, conforming to the standard CME-flare scenario in which a positive feedback between flare reconnection and flux rope acceleration is expected. In contrast, such a correlation does not seem to hold during its main impulsive phase. We attribute the lack of flux rope acceleration during the main impulsive phase to the tether-cutting reconnection scenario when the flux rope eruption has not been fully underway. Our observations also suggest a weakening guide field may contribute to the hardening of the nonthermal electron spectrum throughout the main- and post-impulsive phase of the event.

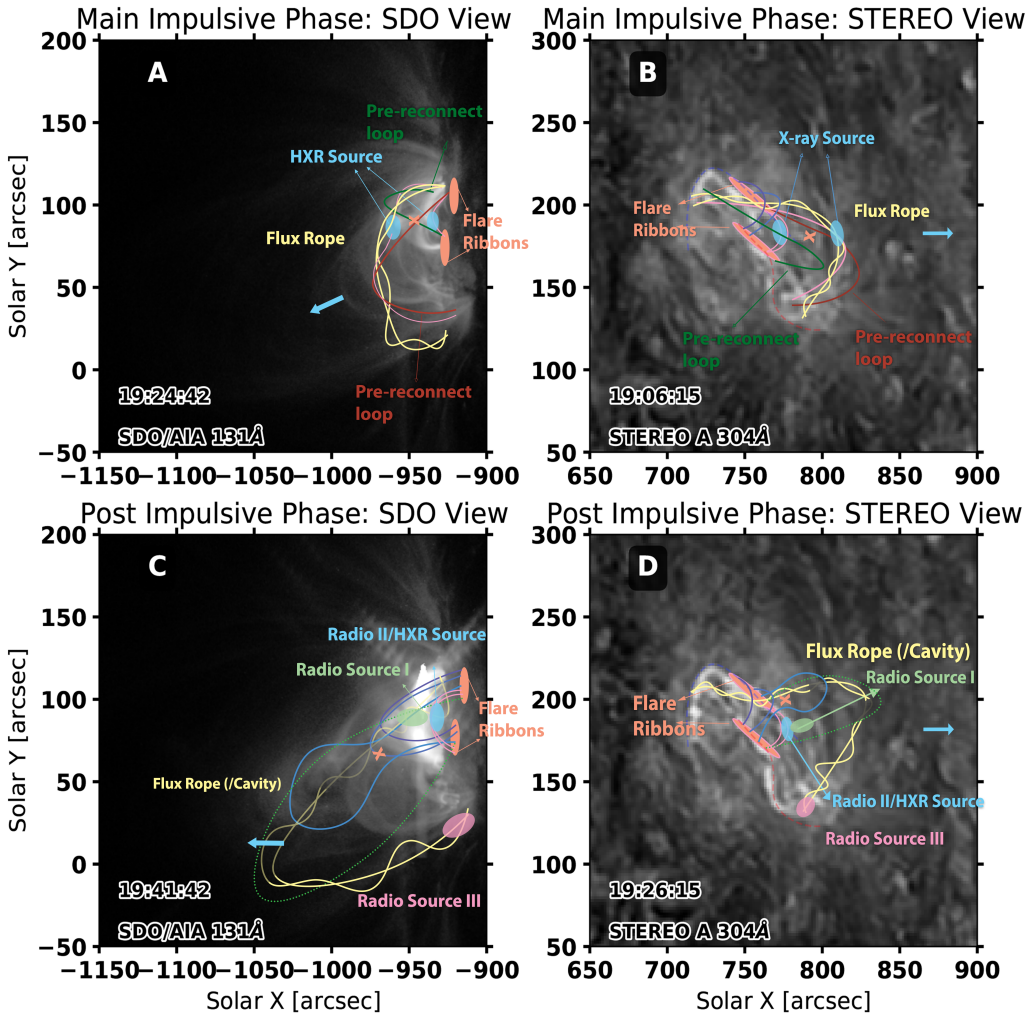

Figure 3.13 Schematic cartoon of the flare geometry in the main-impulsive phase (a)–(b) and post-impulsive phase (c)–(d). (a) The flare geometry from the viewing perspective of the SDO/AIA during the main-impulsive phase. The rising flux rope is marked by the twisted yellow curves. Red and green curves represent magnetic field lines reconnecting in a tether-cutting scenario. The reconnection forms a new field line adding to the flux rope (upper pink curve) and a post-flare arcade (lower pink curve). The orange X denotes the reconnection point. (b) Same as (a), but is plotted in the viewing perspective of STEREO-A/EUVI on 304 Å image. (c) The flare geometry in the viewing perspective of the SDO/AIA during the post-impulsive phase. The overlying field line around the erupting flux rope cavity is marked by the solid blue curve. The EOVSA microwave source (green oval), RHESSI X-ray source (blue oval), post-flare arcades (solid pink curves), and ribbon brightening (orange ovals) are also shown. The EOVSA microwave source at the southern footpoint of the erupting flux rope is shown as the pink oval. The background image is the same as in Figure 3.5(a), showing the cross-section of the flux rope cavity. (d) Same as (c), but is plotted in the viewing perspective of STEREO-A/EUVI on 304 Å image.

CHAPTER 4

DISSERTATION SUMMARY AND FUTURE PROSPECTIVES

4.1 Summary

As discussed in Chapter 1 this dissertation focuses on two science questions:

- What are the three-dimensional magnetic structures of solar flares and MFRs?
- What is the relationship between the different forms of energy that are released during a flare? How are they coupled together?

In chapter 2, we address question Number one. With the microwave imaging spectroscopy observations from EOVSA, we provide the first measurement of the spatially resolved magnetic field along an erupting filament in a flare-productive AR. The magnetic field strength ranges from 600–1400 Gauss from its apex to the legs. The results agree well with those derived from the NLFFF extrapolation. The study demonstrates that microwave imaging spectroscopy observation is the only solution so far to measure the dynamically evolving magnetic field of filament-MFR system. The measurement provides direct constraints for understanding the eruption conditions for the flux rope in the mechanisms that involve MHD instabilities (e.g., torus instability [131], kink instability [109]). The results also suggest that the microwave counterpart of the erupting filament is likely due to flare-accelerated electrons injected into the filament-hosting magnetic flux rope cavity following the newly reconnected magnetic field lines. Furthermore, the limited angular resolution, dynamic range, and image fidelity of EOVSA observations of this event do not allow us to derive a detailed map of the magnetic field distribution above the filament. However, these measurements should be routinely available with a next-generation solar radio telescope with superb spatial resolution and sensitivity, such as the Frequency Agile Solar Radiotelescope [85].

In chapter 3, we turn to question Number two. As discussed in Chapter 1, electron energization and bulk kinetic energy are important energy forms that are released during the solar flare. In a CME-associated solar flare, the relation between the evolution of electron energization and the bulk kinetic energy of the flux rope is critical to understand the physical relation between solar flare and the associated CME. In chapter 3, we have reported a study on an eruptive flare event which features three post-impulsive X-ray and microwave bursts immediately following its main impulsive phase. We have investigated the relationship between the flux rope acceleration and the electron energization in the context of the flare geometry and its evolution. We have found a positive correlation between the flux rope acceleration and electron energization during the post-impulsive phase bursts, conforming to the standard CME-flare scenario in which a positive feedback between flare reconnection and flux rope acceleration is expected. In contrast, such a correlation does not seem to hold during its main impulsive phase. We attribute the lack of flux rope acceleration during the main impulsive phase to the tether-cutting reconnection scenario when the flux rope eruption has not been fully underway. In addition, our observations also suggest a weakening guide field may contribute to the hardening of the nonthermal electron spectrum throughout the main- and post-impulsive phase of the event. The observation provides some constrains on determining the role of two electron-acceleration mechanisms in the reconnection: acceleration in parallel electric fields and "Fermi-type" mechanism [53, 7].

4.2 Future Prospectives

After EOVSA started providing microwave imaging spectroscopy observations, its unique role in contributing to nonthermal electron analysis and diagnosis on the magnetic field has been demonstrated by a great number of studies [84, 72, 37, 35, 38, 73]. The whole-day, full-disk observation makes the EOVSA data a gold

mine. Further progress will be anticipated with EOVSA imaging spectroscopy data to solve the "big questions," especially those on coronal magnetometry and particle acceleration.

On the one hand, Although we measured the spatially resolved magnetic field along an erupting filament in Chapter 2, our measurement did not reveal the quantitative evolution of the magnetic field strength in the source region. For example, the toroidal flux of the magnetic flux rope at its leg region is believed to be the indicator of many critical processes of the flux rope during its eruption, which includes but not limited to the unwinding motion of the flux rope during its eruption, reconnection between the field lines within the flux rope, and build-up of the flux rope. It is expected that such an evolution can be reflected in the evolution of the magnetic field strength and can be potentially diagnosed using EOVSA's microwave imaging spectroscopy observations.

Next-generation radio interferometric arrays in the near future, such as the Frequency Agile Solar Radiotelescope (FASR; Gary et al. 85), will bring microwave spectroscopy with a much larger dynamic range, polarization purity, resolution, and imaging fidelity. Such observations can map the detailed line-of-sight component of the magnetic field B_{LOS} dynamically not only at the footpoint region of the flux rope, but also the entire flux rope simultaneously.

With the measurements of the highly dynamic coronal magnetic field in and around the energy release region in the corona, the energy release during the reconnection can be better understood. In most of the previous studies, the energy release is inferred indirectly by the magnetic flux change rate which is constrained by the spreading motion of the flare ribbons [203, 125, 158, 267]. A spatially resolved coronal magnetometry is therefore critical to understanding the reconnection region. Recently, using EOVSA's microwave imaging spectroscopy, Chen et al. [35] has already reported magnetic field measurements along a current-sheet feature in a

solar flare. In the future, a spatially and temporally resolved line-of-sight component of the magnetic field diagnostic of the reconnection region may be expected. As discussed in Chapter 3, the guide field component measurement of the magnetic field in the reconnection region is critical in particle energization during the reconnection. For the events with a proper viewing geometry, the guide field component can be directly constrained owing to the accurate radio polarimetry of FASR.

On the other hand, the diagnostic of accelerated electrons during solar flares is still not comprehensive enough. As the most important tools for tracing and diagnosing the accelerated electrons during the flares, microwave and HXR observation have already been proven to be a good combination that complements each other perfectly [251, 38]. The operation of the Spectrometer/Telescope for Imaging X-rays (STIX; Krucker et al. 143) on Solar Orbiter [188] brings back the missing X-ray imaging spectroscopy observation since RHESSI decomissioned in 2018. Meanwhile, STIX also provides nonthermal electron diagnostics from different viewing perspectives. In the near future, we may expect next-generation HXR and radio instruments such as a Focusing Optics X-ray Solar Imager (FOXSI; Krucker et al. 141) satellite and FASR working together. These joint observations of HXR and microwave imaging spectroscopy provide critical inputs to revealing the primary site and the main mechanism(s) of the electron acceleration during the solar flares. The observations from different perspectives would also be helpful in extending the standard flare model into a three-dimensional model by revealing the distribution of the energized electrons and its evolution along PIL. It is important to study events jointly observed by STIX and EOVSA.

Macroscopic kinetic modeling has been progressing rapidly in the past few years [7, 152, 265]. In recent studies, nonthermal spatial distribution and spectral index of the nonthermal electrons are found to be comparable between microwave/X-ray observation [38] and simulation[153]. The studies have shown a big potential of data-

constrained Macroscopic kinetic modeling in understanding particle acceleration and transport during the solar flare. Advances are anticipated to carry out similar studies with EOVSA data.

As discussed in Chapter 1, particle acceleration not only occurs during the impulsive phase. EOVSA data has been utilized to shed new light into the particle acceleration processes during the decay phase of a solar flare [260]. Other phenomena during the decay phase may also be associated with electron acceleration, such as the supra-arcade downflows (SADs). A promising event has already been found in the EOVSA archive, which is also covered by STIX. Last but not least, the research into flare precursors observed in the microwave regime is still very limited. As a sensitive probe of accelerated electrons in the solar corona, EOVSA microwave imaging spectroscopy will be an important complement to the multi-band observation of flare precursors to better understand the initiation of solar flares.

CHAPTER 5

BIBLIOGRAPHY

[1] L.W. Acton, Uri Feldman, Marilyn E. Bruner, George A. Doschek, Tadashi Hirayama, Hugh S. Hudson, James R. Lemen, Yoshiaki Ogawara, Keith T. Strong, and Saku Tsuneta. The Morphology of 20times 10(6) K Plasma in Large Non-Impulsive Solar Flares. *Publications of the Astronomical Society of Japan*, 44:L71–L75, October 1992. ISSN 0004-6264.

[2] M.D. Andrews. A Search for CMEs Associated with Big Flares. *Solar Physics*, 218(1):261–279, December 2003. ISSN 1573-093X. doi: 10.1023/B:SOLA.0000013039.69550.bf.

[3] J. Andries, T. Van Doorsselaere, B. Roberts, G. Verth, E. Verwichte, and R. Erdélyi. Coronal Seismology by Means of Kink Oscillation Overtones. *Space Science Reviews*, 149(1-4):3–29, dec 2009. ISSN 0038-6308. doi: 10.1007/s11214-009-9561-2. URL `http://link.springer.com/10.1007/s11214-009-9561-2`.

[4] Sergey A. Anfinogentov, Alexey G. Stupishin, Ivan I. Mysh'yakov, and Gregory D. Fleishman. Record-breaking Coronal Magnetic Field in Solar Active Region 12673. *The Astrophysical Journal*, 880(2):L29, aug 2019. ISSN 2041-8213. doi: 10.3847/2041-8213/ab3042. URL `https://iopscience.iop.org/article/10.3847/2041-8213/ab3042`.

[5] S. K. Antiochos, R. B. Dahlburg, and J. A. Klimchuk. The Magnetic Field of Solar Prominences. *The Astrophysical Journal*, 420:L41, January 1994. ISSN 0004-637X. doi: 10.1086/187158.

[6] S. K. Antiochos, C. R. DeVore, and J. A. Klimchuk. A Model for Solar Coronal Mass Ejections. *The Astrophysical Journal*, 510(1):485, January 1999. ISSN 0004-637X. doi: 10.1086/306563.

[7] H. Arnold, J. F. Drake, M. Swisdak, F. Guo, J. T. Dahlin, B. Chen, G. Fleishman, L. Glesener, E. Kontar, T. Phan, and C. Shen. Electron Acceleration during Macroscale Magnetic Reconnection. *Physical Review Letters*, 126(13):135101, March 2021. doi: 10.1103/PhysRevLett.126.135101.

[8] G. Aulanier, M. Janvier, and B. Schmieder. The standard flare model in three dimensions. *Astronomy and Astrophysics*, 543:A110, jul 2012. ISSN 0004-6361. doi: 10.1051/0004-6361/201219311. URL `http://www.aanda.org/10.1051/0004-6361/201219311`.

[9] G. Aulanier, M. Janvier, and B. Schmieder. The standard flare model in three dimensions - I. Strong-to-weak shear transition in post-flare loops. *Astronomy & Astrophysics*, 543:A110, July 2012. ISSN 0004-6361, 1432-0746. doi: 10.1051/0004-6361/201219311.

[10] H. M. Bain, S. Krucker, P. Saint-Hilaire, and C. L. Raftery. Radio Imaging of a Type IVM Radio Burst on the 14th of August 2010. , 782(1):43, February 2014. doi: 10.1088/0004-637X/782/1/43.

[11] T. S. Bastian, A. O. Benz, and D. E. Gary. Radio Emission from Solar Flares. *Annual Review of Astronomy and Astrophysics*, 36(1):131–188, 1998. doi: 10.1146/annurev.astro.36.1.131.

[12] T. S. Bastian, M. Pick, A. Kerdraon, D. Maia, and A. Vourlidas. The Coronal Mass Ejection of 1998 April 20: Direct Imaging at Radio Wavelengths. , 558 (1):L65–L69, September 2001. doi: 10.1086/323421.

[13] Tim Bastian, H. Bain, R. Bradley, B. Chen, J. Dahlin, E. DeLuca, J. Drake, G. Fleishman, D. Gary, L. Glesener, Fan Guo, G. Hallinan, G. Hurford, J. Kasper, Hantao Ji, J. Klimchuk, A. Kobelski, S. Krucker, N. Kuroda, D. Loncope, C. Lonsdale, J. McTiernan, G. Nita, J. Qiu, K. Reeves, P. Saint-Hilaire, S. Schonfeld, Chengcai Shen, S. Tun, D. Wertheimer, and S. White. Frequency Agile Solar Radiotelescope. *Astro2020: Decadal Survey on Astronomy and Astrophysics*, 2020:56, Sep 2019. URL `https://ui.adsabs.harvard.edu/abs/2019astro2020U..56B/abstract`.

[14] G. Bateman. MHD instabilities. January 1978.

[15] M. Battaglia and A. O. Benz. Relations between concurrent hard X-ray sources in solar flares. *Astronomy and Astrophysics*, 456(2):751–760, September 2006. ISSN 0004-6361, 1432-0746. doi: 10.1051/0004-6361:20065233.

[16] M. Battaglia and A. O. Benz. Exploring the connection between coronal and footpoint sources in a thin-thick target solar flare model. *Astronomy and Astrophysics*, 466(2):713–716, May 2007. ISSN 0004-6361, 1432-0746. doi: 10.1051/0004-6361:20077144.

[17] U. Bąk-Stęślicka, Sarah E. Gibson, Yuhong Fan, Christian Bethge, Blake Forland, and Laurel A. Rachmeler. The magnetic structure of solar prominence cavities: New observational signature revealed by coronal magnetometry. *Astrophysical Journal Letters*, 770(2):L28, jun 2013. ISSN 20418205. doi: 10.1088/2041-8205/770/2/L28. URL `http://people.hao.ucar.edu/sgibson/FORWARD/`.

[18] A. O. Benz. *Plasma Astrophysics: Kinetic Processes in Solar and Stellar Coronae*. Springer, Netherlands, Dordrecht, 2002. ISBN 978-1-4020-0695-1 978-0-306-47719-5. doi: 10.1007/0-306-47719-X.

[19] A. O. Benz. Flare Observations. *Living Reviews in Solar Physics*, 14(1):2, dec 2017. ISSN 2367-3648. doi: 10.1007/s41116-016-0004-3. URL `http://link.springer.com/10.1007/s41116-016-0004-3`.

[20] Mitchell A. Berger and Chris Prior. The writhe of open and closed curves. *Journal of Physics A: Mathematical and General*, 39(26):8321, June 2006. ISSN 0305-4470. doi: 10.1088/0305-4470/39/26/005.

[21] H. Bethe, W. Heitler, and Paul Adrien Maurice Dirac. On the stopping of fast particles and on the creation of positive electrons. *Proceedings of the Royal Society of London. Series A, Containing Papers of a Mathematical and Physical Character*, 146(856):83–112, January 1934. doi: 10.1098/rspa.1934.0140.

[22] J. Birn, L. Fletcher, M. Hesse, and T. Neukirch. Energy Release and Transfer in Solar Flares: Simulations of Three-Dimensional Reconnection. *The Astrophysical Journal*, 695(2):1151, April 2009. ISSN 0004-637X. doi: 10.1088/0004-637X/695/2/1151.

[23] Véronique Bommier, Egidio Landi Degl'Innocenti, Jean-Louis Leroy, and Sylvie Sahal-Bréchot. Complete determination of the magnetic field vector and of the electron density in 14 prominences from linear polarizaton measurements in the hei d3 and hα lines. *Solar Physics*, 154(2):231–260, Oct 1994. ISSN 1573-093X. doi: 10.1007/BF00681098. URL `https://doi.org/10.1007/BF00681098`.

[24] David H. Brooks, Harry P. Warren, and Enrico Landi. Measurements of Coronal Magnetic Field Strengths in Solar Active Region Loops. , 915(1):L24, July 2021. doi: 10.3847/2041-8213/ac0c84.

[25] J. C. Brown, V. A. Carlaw, D. Cromwell, and S. R. Kane. A Comparison of the Thick Target Model with Stereo Data on the Height Structure of Solar Hard

X-Ray Bursts. *Solar Physics*, 88:281–295, October 1983. ISSN 0038-0938. doi: 10.1007/BF00196193.

[26] John C. Brown. The deduction of energy spectra of non-thermal electrons in flares from the observed dynamic spectra of hard X-ray bursts. *Solar Physics*, 18(3):489–502, July 1971. ISSN 1573-093X. doi: 10.1007/BF00149070.

[27] G. E. Brueckner, R. A. Howard, M. J. Koomen, C. M. Korendyke, D. J. Michels, J. D. Moses, D. G. Socker, K. P. Dere, P. L. Lamy, A. Llebaria, M. V. Bout, R. Schwenn, G. M. Simnett, D. K. Bedford, and C. J. Eyles. The Large Angle Spectroscopic Coronagraph (LASCO). In B. Fleck, V. Domingo, and A. Poland, editors, *The SOHO Mission*, pages 357–402. Springer, Netherlands, Dordrecht, 1995. ISBN 978-94-009-0191-9. doi: 10.1007/978-94-009-0191-9_10.

[28] A. Canou and T. Amari. A Twisted Flux Rope as the Magnetic Structure of a Filament in Active Region 10953 Observed by Hinode. *The Astrophysical Journal*, 715(2):1566, May 2010. ISSN 0004-637X. doi: 10.1088/0004-637X/715/2/1566.

[29] W. Cao, N. Gorceix, R. Coulter, K. Ahn, T. R. Rimmele, and P. R. Goode. Scientific instrumentation for the 1.6 m New Solar Telescope in Big Bear. *Astronomische Nachrichten*, 331(6):636–639, jun 2010. ISSN 00046337. doi: 10.1002/asna.201011390. URL `http://doi.wiley.com/10.1002/asna.201011390`.

[30] Eoin P. Carley, Nicole Vilmer, Paulo J. A. Simões, and Brían Ó Fearraigh. Estimation of a coronal mass ejection magnetic field strength using radio observations of gyrosynchrotron radiation. , 608:A137, December 2017. doi: 10.1051/0004-6361/201731368.

[31] H. Carmichael. A Process for Flares. *NASA Special Publication*, 50:451, January 1964.

[32] R. C. Carrington. Description of a Singular Appearance seen in the Sun on September 1, 1859. *Monthly Notices of the Royal Astronomical Society*, 20(1): 13–15, November 1859. ISSN 0035-8711. doi: 10.1093/mnras/20.1.13.

[33] R. Chandra, B. Schmieder, G. Aulanier, and J. M. Malherbe. Evidence of Magnetic Helicity in Emerging Flux and Associated Flare. *Solar Physics*, 258 (1):53–67, August 2009. ISSN 1573-093X. doi: 10.1007/s11207-009-9392-z.

[34] B. Chen, Chengcai Shen, Dale E. Gary, Katharine K. Reeves, Gregory D. Fleishman, Sijie Yu, Fan Guo, Säm Krucker, Jun Lin, Gelu M. Nita, and Xiangliang Kong. Measurement of magnetic field and relativistic electrons along a solar flare current sheet - Nature Astronomy. *Nat. Astron.*, 4(12):1140–1147, Dec 2020. ISSN 2397-3366. doi: 10.1038/s41550-020-1147-7.

[35] B. Chen, Chengcai Shen, Dale E. Gary, Katharine K. Reeves, Gregory D. Fleishman, Sijie Yu, Fan Guo, Säm Krucker, Jun Lin, Gelu Nita, and Xiangliang Kong. Measurement of magnetic field and relativistic electrons along a solar flare current sheet. *Nature Astronomy*, 4(12):1140–1147, December 2020. ISSN 2397-3366. doi: 10.1038/s41550-020-1147-7.

[36] B. Chen, Sijie Yu, Katharine K. Reeves, and Dale E. Gary. Microwave Spectral Imaging of an Erupting Magnetic Flux Rope: Implications for the Standard Solar Flare Model in Three Dimensions. *The Astrophysical Journal*, 895 (2):L50, jun 2020. ISSN 2041-8213. doi: 10.3847/2041-8213/ab901a. URL `https://iopscience.iop.org/article/10.3847/2041-8213/ab901ahttps://iopscience.iop.org/article/10.3847/2041-8213/ab901a/meta`.

[37] B. Chen, Sijie Yu, Katharine K. Reeves, and Dale E. Gary. Microwave Spectral Imaging of an Erupting Magnetic Flux Rope: Implications for the Standard Solar Flare Model in Three Dimensions. *The Astrophysical Journal Letters*, 895(2):L50, June 2020. ISSN 2041-8205. doi: 10.3847/2041-8213/ab901a.

[38] B. Chen, Marina Battaglia, Säm Krucker, Katharine K. Reeves, and Lindsay Glesener. Energetic Electron Distribution of the Coronal Acceleration Region: First Results from Joint Microwave and Hard X-Ray Imaging Spectroscopy. *The Astrophysical Journal Letters*, 908(2):L55, February 2021. ISSN 2041-8205. doi: 10.3847/2041-8213/abe471.

[39] Bin Chen, T. S. Bastian, and D. E. Gary. Direct Evidence of an Eruptive, Filament-hosting Magnetic Flux Rope Leading to a Fast Solar Coronal Mass Ejection. , 794(2):149, October 2014. doi: 10.1088/0004-637X/794/2/149.

[40] Bin Chen, Marina Battaglia, Säm Krucker, Katharine K. Reeves, and Lindsay Glesener. Energetic Electron Distribution of the Coronal Acceleration Region: First Results from Joint Microwave and Hard X-Ray Imaging Spectroscopy. , 908(2):L55, February 2021. doi: 10.3847/2041-8213/abe471.

[41] H. Chen, Jun Zhang, Xin Cheng, Suli Ma, Shuhong Yang, and Ting Li. DIRECT OBSERVATIONS OF TETHER-CUTTING RECONNECTION DURING A MAJOR SOLAR EVENT FROM 2014 FEBRUARY 24 TO 25. *The Astrophysical Journal Letters*, 797(2):L15, December 2014. ISSN 2041-8205. doi: 10.1088/2041-8205/797/2/L15.

[42] P. F. Chen. Coronal Mass Ejections: Models and Their Observational Basis. *Living Reviews in Solar Physics*, 8(1):1, April 2011. ISSN 1614-4961. doi: 10.12942/lrsp-2011-1.

[43] Yajie Chen, Xianyu Liu, Hui Tian, Xianyong Bai, Meng Jin, Wenxian Li, Yang Yang, Zihao Yang, and Yuanyong Deng. Measurements of the Magnetic Field Strengths at the Bases of Stellar Coronae Using the Magnetic-field-induced Transition Theory. , 918(1):L13, September 2021. doi: 10.3847/2041-8213/ac1e9a.

[44] Yu Chen, Qiang Hu, Lingling Zhao, Justin C. Kasper, Stuart D. Bale, Kelly E. Korreck, Anthony W. Case, Michael L. Stevens, John W. Bonnell, Keith Goetz, Peter R. Harvey, Kristopher G. Klein, Davin E. Larson, Roberto Livi, Robert J. MacDowall, David M. Malaspina, Marc Pulupa, and Phyllis L. Whittlesey. Small-scale Magnetic Flux Ropes in the First Two Parker Solar Probe Encounters. *The Astrophysical Journal*, 903(1):76, November 2020. ISSN 0004-637X. doi: 10.3847/1538-4357/abb820.

[45] C Z Cheng, Y Ren, and G S Choe. Flux Rope Acceleration and Enhanced Magnetic Reconnection Rate. 596(2):6, 2003.

[46] X. Cheng, J. Zhang, Y. Liu, and M. D. Ding. Observing Flux Rope Formation During the Impulsive Phase of a Solar Eruption. *The Astrophysical Journal Letters*, 732(2):L25, April 2011. ISSN 2041-8205. doi: 10.1088/2041-8205/732/2/L25.

[47] X. Cheng, M. D. Ding, Y. Guo, J. Zhang, A. Vourlidas, Y. D. Liu, O. Olmedo, J. Q. Sun, and C. Li. Tracking the Evolution of a Coherent Magnetic Flux Rope Continuously From the Inner to the Outer Corona. *The Astrophysical Journal*, 780(1):28, December 2013. ISSN 0004-637X. doi: 10.1088/0004-637X/780/1/28.

[48] X. Cheng, J. Zhang, B. Kliem, T. Török, C. Xing, Z. J. Zhou, B. Inhester, and M. D. Ding. Initiation and Early Kinematic Evolution of Solar Eruptions. *The*

Astrophysical Journal, 894(2):85, May 2020. ISSN 0004-637X. doi: 10.3847/1538-4357/ab886a.

[49] Sherry Chhabra, Dale E. Gary, Gregg Hallinan, Marin M. Anderson, Bin Chen, Lincoln J. Greenhill, and Danny C. Price. Imaging Spectroscopy of CME-associated Solar Radio Bursts using OVRO-LWA. , 906(2):132, January 2021. doi: 10.3847/1538-4357/abc94b.

[50] Steven Christe, Samuel Krucker, Lindsay Glesener, Albert Shih, Pascal Saint-Hilaire, Amir Caspi, Joel Allred, Marina Battaglia, B. Chen, James Drake, Brian Dennis, Dale Gary, Szymon Gburek, Keith Goetz, Brian Grefenstette, Mikhail Gubarev, Iain Hannah, Gordon Holman, Hugh Hudson, Andrew Inglis, Jack Ireland, Shinosuke Ishikawa, James Klimchuk, Eduard Kontar, Adam Kowalski, Dana Longcope, Anna-Maria Massone, Sophie Musset, Michele Piana, Brian Ramsey, Daniel Ryan, Richard Schwartz, Marek Steślicki, Paul Turin, Alexander Warmuth, Colleen Wilson-Hodge, Stephen White, Astrid Veronig, Nicole Vilmer, and Tom Woods. Exploring impulsive solar magnetic energy release and particle acceleration with focused hard X-ray imaging spectroscopy, January 2017.

[51] J. T. Dahlin, J. F. Drake, and M. Swisdak. The mechanisms of electron heating and acceleration during magnetic reconnection. *Physics of Plasmas*, 21(9): 092304, September 2014. ISSN 1070-664X. doi: 10.1063/1.4894484.

[52] J. T. Dahlin, J. F. Drake, and M. Swisdak. Electron acceleration in three-dimensional magnetic reconnection with a guide field. *Physics of Plasmas*, 22 (10):100704, October 2015. ISSN 1070-664X. doi: 10.1063/1.4933212.

[53] J. T. Dahlin, J. F. Drake, and M. Swisdak. Parallel electric fields are inefficient drivers of energetic electrons in magnetic reconnection. *Physics of Plasmas*, 23

(12):120704, December 2016. ISSN 1070-664X. doi: 10.1063/1.4972082.

[54] Joel T. Dahlin, Spiro K. Antiochos, Jiong Qiu, and C. Richard DeVore. Variability of the Reconnection Guide Field in Solar Flares. *The Astrophysical Journal*, 932(2):94, June 2022. ISSN 0004-637X. doi: 10.3847/1538-4357/ac6e3d.

[55] B. De Pontieu, A. M. Title, J. R. Lemen, G. D. Kushner, D. J. Akin, B. Allard, T. Berger, P. Boerner, M. Cheung, C. Chou, J. F. Drake, D. W. Duncan, S. Freeland, G. F. Heyman, C. Hoffman, N. E. Hurlburt, R. W. Lindgren, D. Mathur, R. Rehse, D. Sabolish, R. Seguin, C. J. Schrijver, T. D. Tarbell, J.-P. Wülser, C. J. Wolfson, C. Yanari, J. Mudge, N. Nguyen-Phuc, R. Timmons, R. van Bezooijen, I. Weingrod, R. Brookner, G. Butcher, B. Dougherty, J. Eder, V. Knagenhjelm, S. Larsen, D. Mansir, L. Phan, P. Boyle, P. N. Cheimets, E. E. DeLuca, L. Golub, R. Gates, E. Hertz, S. McKillop, S. Park, T. Perry, W. A. Podgorski, K. Reeves, S. Saar, P. Testa, H. Tian, M. Weber, C. Dunn, S. Eccles, S. A. Jaeggli, C. C. Kankelborg, K. Mashburn, N. Pust, L. Springer, R. Carvalho, L. Kleint, J. Marmie, E. Mazmanian, T. M. D. Pereira, S. Sawyer, J. Strong, S. P. Worden, M. Carlsson, V. H. Hansteen, J. Leenaarts, M. Wiesmann, J. Aloise, K.-C. Chu, R. I. Bush, P. H. Scherrer, P. Brekke, J. Martinez-Sykora, B. W. Lites, S. W. McIntosh, H. Uitenbroek, T. J. Okamoto, M. A. Gummin, G. Auker, P. Jerram, P. Pool, and N. Waltham. The Interface Region Imaging Spectrograph (IRIS). *Solar Physics*, 289(7): 2733–2779, July 2014. ISSN 1573-093X. doi: 10.1007/s11207-014-0485-y.

[56] Marc L. De Rosa, Carolus J. Schrijver, Graham Barnes, K. D. Leka, Bruce W. Lites, Markus J. Aschwanden, Tahar Amari, Aurélien Canou, James M. McTiernan, Stéphane Régnier, Julia K. Thalmann, Gherardo Valori, Michael S. Wheatland, Thomas Wiegelmann, Mark C. M. Cheung, Paul A. Conlon, Marcel

Fuhrmann, Bernd Inhester, and Tilaye Tadesse. A Critical Assessment of Nonlinear Force-Free Field Modeling of the Solar Corona for Active Region 10953. , 696(2):1780–1791, May 2009. doi: 10.1088/0004-637X/696/2/1780.

[57] Brian R. Dennis and Dominic M. Zarro. The Neupert effect: What can it tell us about the impulsive and gradual phases of solar flares? *Solar Physics*, 146 (1):177–190, July 1993. ISSN 1573-093X. doi: 10.1007/BF00662178.

[58] E. C. M. Dickson and E. P. Kontar. Measurements of Electron Anisotropy in Solar Flares Using Albedo with RHESSI X-Ray Data. *Solar Physics*, 284(2): 405–425, June 2013. ISSN 1573-093X. doi: 10.1007/s11207-012-0178-3.

[59] G. A. Doschek. The Solar Flare Plasma: Observation and Interpretation. *International Astronomical Union Colloquium*, 14:765–821, November 1972. ISSN 0252-9211. doi: 10.1017/S0252921100089971.

[60] G. A. Doschek. Soft X-Ray Spectroscopy of Solar Flares: An Overview. *The Astrophysical Journal Supplement Series*, 73:117, June 1990. ISSN 0067-0049. doi: 10.1086/191443.

[61] J. B. Dove, S. E. Gibson, L. A. Rachmeler, S. Tomczyk, and P. Judge. A ring of polarized light: Evidence for twisted coronal magnetism in cavities. *Astrophysical Journal Letters*, 731(1 PART II):1, apr 2011. ISSN 20418213. doi: 10.1088/2041-8205/731/1/L1. URL `https://iopscience.iop.org/article/10.1088/2041-8205/731/1/L1https://iopscience.iop.org/article/10.1088/2041-8205/731/1/L1/meta`.

[62] J. F. Drake, M. A. Shay, W. Thongthai, and M. Swisdak. Production of Energetic Electrons during Magnetic Reconnection. *Physical Review Letters*, 94(9):095001, March 2005. doi: 10.1103/PhysRevLett.94.095001.

[63] M. Dryer. Coronal transient phenomena. *Space Science Reviews*, 33:233–275, March 1982. ISSN 0038-6308. doi: 10.1007/BF00213256.

[64] G. A. Dulk. Radio emission from the sun and stars. , 23:169–224, January 1985. doi: 10.1146/annurev.aa.23.090185.001125.

[65] George A. Dulk. Radio Emission from the Sun and Stars. *Annual Review of Astronomy and Astrophysics*, 23(1):169–224, 1985. doi: 10.1146/annurev.aa.23.090185.001125.

[66] J. Egedal, W. Daughton, J. F. Drake, N. Katz, and A. Lê. Formation of a localized acceleration potential during magnetic reconnection with a guide field. *Physics of Plasmas*, 16(5):050701, May 2009. ISSN 1070-664X. doi: 10.1063/1.3130732.

[67] David F. Elmore, Joan T. Burkepile, J. Anthony Darnell, Alice R. Lecinski, and Andrew L. Stanger. Calibration of a ground-based solar coronal polarimeter. In *Polarimetry in Astronomy*, volume 4843, pages 66–75. SPIE, February 2003. doi: 10.1117/12.459279.

[68] Uri Feldman. Elemental abundances in the upper solar atmosphere. *Physica Scripta*, 46(3):202, September 1992. ISSN 1402-4896. doi: 10.1088/0031-8949/46/3/002.

[69] Boris Filippov, Olesya Martsenyuk, Abhishek K. Srivastava, and Wahab Uddin. Solar Magnetic Flux Ropes. *J. Astrophys. Astron.*, 36(1):157–184, Mar 2015. ISSN 0973-7758. doi: 10.1007/s12036-015-9321-5.

[70] Gregory D. Fleishman and Alexey A. Kuznetsov. FAST GYROSYNCHROTRON CODES. *The Astrophysical Journal*, 721(2):1127–1141, oct 2010. ISSN 0004-637X. doi: 10.1088/0004-637X/721/2/1127.

URL https://iopscience.iop.org/article/10.1088/0004-637X/721/2/1127.

[71] Gregory D. Fleishman and Alexey A. Kuznetsov. FAST GYROSYNCHROTRON CODES. *The Astrophysical Journal*, 721(2): 1127, September 2010. ISSN 0004-637X. doi: 10.1088/0004-637X/721/2/1127.

[72] Gregory D. Fleishman, Dale E. Gary, B. Chen, Natsuha Kuroda, Sijie Yu, and Gelu M. Nita. Decay of the coronal magnetic field can release sufficient energy to power a solar flare. *Science*, 367(6475):278–280, jan 2020. ISSN 10959203. doi: 10.1126/science.aax6874.

[73] Gregory D. Fleishman, Gelu M. Nita, B. Chen, Sijie Yu, and Dale E. Gary. Solar flare accelerates nearly all electrons in a large coronal volume. *Nature*, 606:674–677, June 2022. ISSN 0028-0836. doi: 10.1038/s41586-022-04728-8.

[74] L. Fletcher and H. S. Hudson. Impulsive Phase Flare Energy Transport by Large-Scale Alfvén Waves and the Electron Acceleration Problem. *The Astrophysical Journal*, 675(2):1645, March 2008. ISSN 0004-637X. doi: 10.1086/527044.

[75] L. Fletcher and H.S. Hudson. Spectral and Spatial Variations of Flare Hard X-ray Footpoints. *Solar Physics*, 210(1):307–321, November 2002. ISSN 1573-093X. doi: 10.1023/A:1022479610710.

[76] L. Fletcher, I. G. Hannah, H. S. Hudson, and T. R. Metcalf. A TRACE White Light and RHESSI Hard X-Ray Study of Flare Energetics. *The Astrophysical Journal*, 656(2):1187, February 2007. ISSN 0004-637X. doi: 10.1086/510446.

[77] T. G. Forbes, J. A. Linker, J. Chen, C. Cid, J. Kóta, M. A. Lee, G. Mann, Z. Mikić, M. S. Potgieter, J. M. Schmidt, G. L. Siscoe, R. Vainio, S. K.

Antiochos, and P. Riley. CME Theory and Models. *Space Science Reviews*, 123 (1):251–302, March 2006. ISSN 1572-9672. doi: 10.1007/s11214-006-9019-8.

[78] S.L. Freeland and B.N. Handy. Data Analysis with the SolarSoft System. *Solar Physics*, 182(2):497–500, October 1998. ISSN 1573-093X. doi: 10.1023/A:1005038224881.

[79] D. E. Gary and C. U. Keller. *Solar and Space Weather Radiophysics*. Springer, Netherlands, Springer Science+Business Media B.V., 2004. ISBN 978-1-4020-2813-7. doi: 10.1007/978-1-4020-2814-4.

[80] D. E. Gary and C. U. Keller. *Solar and Space Weather Radiophysics: Current Status and Future Developments*. Springer Science & Business Media, September 2004. ISBN 978-1-4020-2813-7.

[81] D. E. Gary, G. A. Dulk, L. L. House, R. Illing, W. J. Wagner, and D. J. Mclean. The type IV burst of 1980 June 29, 0233 UT - Harmonic plasma emission? *Astron. Astrophys.*, 152:42–50, Nov 1985. ISSN 0004-6361. URL `https://ui.adsabs.harvard.edu/abs/1985A%26A...152...42G/abstract`.

[82] D. E. Gary, G. D. Fleishman, and G. M. Nita. Magnetography of Solar Flaring Loops with Microwave Imaging Spectropolarimetry. *Solar Physics*, 288(2):549–565, dec 2013. ISSN 0038-0938. doi: 10.1007/s11207-013-0299-3. URL `http://link.springer.com/10.1007/s11207-013-0299-3`.

[83] Dale E. Gary and G. J. Hurford. Multifrequency Observations of a Solar Microwave Burst with Two-dimensional Spatial Resolution. *The Astrophysical Journal*, 361:290, September 1990. ISSN 0004-637X. doi: 10.1086/169194.

[84] Dale E. Gary, B. Chen, Brian R. Dennis, Gregory D. Fleishman, Gordon J. Hurford, Säm Krucker, James M. McTiernan, Gelu M. Nita, Albert Y. Shih,

Stephen M. White, and Sijie Yu. Microwave and Hard X-Ray Observations of the 2017 September 10 Solar Limb Flare. *The Astrophysical Journal*, 863(1): 83, aug 2018. ISSN 1538-4357. doi: 10.3847/1538-4357/aad0ef. URL `https://iopscience.iop.org/article/10.3847/1538-4357/aad0ef`.

[85] Dale E. Gary, B. Chen, James F. Drake, Gregory D. Fleishman, Lindsay Glesener, Pascal Saint-Hilaire, and Stephen M. White. Frequency Agile Solar Radiotelescope: A Next-Generation Radio Telescope for Solar Physics and Space Weather, October 2022.

[86] S. E. Gibson and Y. Fan. The Partial Expulsion of a Magnetic Flux Rope. *The Astrophysical Journal*, 637(1):L65, jan 2006. ISSN 0004-637X. doi: 10.1086/500452. URL `https://iopscience.iop.org/article/10.1086/500452https://iopscience.iop.org/article/10.1086/500452/meta`.

[87] S. E. Gibson and Y. Fan. Coronal prominence structure and dynamics: A magnetic flux rope interpretation. *J. Geophys. Res. Space Phys.*, 111(A12), Dec 2006. ISSN 0148-0227. doi: 10.1029/2006JA011871.

[88] S. E. Gibson and Y. Fan. Coronal prominence structure and dynamics: A magnetic flux rope interpretation. *Journal of Geophysical Research: Space Physics*, 111(A12), 2006. ISSN 2156-2202. doi: 10.1029/2006JA011871.

[89] S. E. Gibson, L. Fletcher, G. Del Zanna, C. D. Pike, H. E. Mason, C. H. Mandrini, P. Démoulin, H. Gilbert, J. Burkepile, T. Holzer, D. Alexander, Y. Liu, N. Nitta, J. Qiu, B. Schmieder, and B. J. Thompson. The Structure and Evolution of a Sigmoidal Active Region. *The Astrophysical Journal*, 574 (2):1021, August 2002. ISSN 0004-637X. doi: 10.1086/341090.

[90] Sarah E. Gibson. Solar prominences: Theory and models. *Living Reviews in Solar Physics*, 15(1):7, October 2018. ISSN 1614-4961. doi: 10.1007/s41116-018-0016-2.

[91] Sarah E. Gibson, Therese A. Kucera, Stephen M. White, James B. Dove, Yuhong Fan, Blake C. Forland, Laurel A. Rachmeler, Cooper Downs, and Katharine K. Reeves. FORWARD: A toolset for multiwavelength coronal magnetometry. 3, mar 2016. doi: 10.3389/fspas.2016.00008.

[92] Jan Gieseler, Nina Dresing, Christian Palmroos, Johan L. Freiherr von Forstner, Daniel J. Price, Rami Vainio, Athanasios Kouloumvakos, Laura Rodríguez-García, Domenico Trotta, Vincent Génot, Arnaud Masson, Markus Roth, and Astrid Veronig. Solar-MACH: An open-source tool to analyze solar magnetic connection configurations. *Frontiers in Astronomy and Space Sciences*, 9, 2023. ISSN 2296-987X.

[93] V. L. Ginzburg and V. V. Zhelezniakov. On the Possible Mechanisms of Sporadic Solar Radio Emission (Radiation in an Isotropic Plasma). *Soviet Astronomy*, 2:653, October 1958. ISSN 0038-5301.

[94] Lindsay Glesener, Säm Krucker, Hazel M. Bain, and Robert P. Lin. Observation of Heating by Flare-accelerated Electrons in a Solar Coronal Mass Ejection. , 779(2):L29, December 2013. doi: 10.1088/2041-8205/779/2/L29.

[95] Philip R. Goode and Wenda Cao. The 1.6 m off-axis New Solar Telescope (NST) in Big Bear. page 844403, sep 2012. doi: 10.1117/12.925494. URL `http://proceedings.spiedigitallibrary.org/proceeding.aspx?doi=10.1117/12.925494`.

[96] L. M. Green and B. Kliem. FLUX ROPE FORMATION PRECEDING CORONAL MASS EJECTION ONSET. *The Astrophysical Journal*, 700(2): L83, July 2009. ISSN 0004-637X. doi: 10.1088/0004-637X/700/2/L83.

[97] L. M. Green, B. Kliem, T. Török, L. van Driel-Gesztelyi, and G. D. R. Attrill. Transient Coronal Sigmoids and Rotating Erupting Flux Ropes. *Solar Physics*, 246(2):365–391, December 2007. ISSN 1573-093X. doi: 10.1007/s11207-007-9061-z.

[98] L. M. Green, B. Kliem, and A. J. Wallace. Photospheric flux cancellation and associated flux rope formation and eruption. *Astronomy & Astrophysics*, 526:A2, February 2011. ISSN 0004-6361, 1432-0746. doi: 10.1051/0004-6361/201015146.

[99] M. Gryciuk, M. Siarkowski, J. Sylwester, S. Gburek, P. Podgorski, A. Kepa, B. Sylwester, and T. Mrozek. Flare Characteristics from X-ray Light Curves. *Solar Physics*, 292(6):77, June 2017. ISSN 1573-093X. doi: 10.1007/s11207-017-1101-8.

[100] Y. Guo, M. D. Ding, B. Schmieder, H. Li, T. Török, and T. Wiegelmann. DRIVING MECHANISM AND ONSET CONDITION OF A CONFINED ERUPTION. *The Astrophysical Journal Letters*, 725(1):L38, November 2010. ISSN 2041-8205. doi: 10.1088/2041-8205/725/1/L38.

[101] Yang Guo, Yu Xu, M. D. Ding, P. F. Chen, Chun Xia, and Rony Keppens. The Magnetic Flux Rope Structure of a Triangulated Solar Filament. *The Astrophysical Journal*, 884(1):L1, oct 2019. ISSN 2041-8213. doi: 10.3847/2041-8213/ab4514. URL `https://iopscience.iop.org/article/10.3847/2041-8213/ab4514`.

[102] M. Haberreiter, W. Schmutz, and A. G. Kosovichev. Solving the Discrepancy between the Seismic and Photospheric Solar Radius. *The Astrophysical Journal*, 675:L53, March 2008. ISSN 0004-637X. doi: 10.1086/529492.

[103] M. J. Hagyard, P. Venkatakrishnan, and J. B. Jr Smith. Nonpotential magnetic fields at sites of gamma-ray flares. June 1990. ISSN 0067-0049.

[104] I. G. Hannah and E. P. Kontar. Differential Emission Measures from the Regularized Inversion of Hinode and SDO data. *Astronomy & Astrophysics*, 539:A146, March 2012. ISSN 0004-6361, 1432-0746. doi: 10.1051/0004-6361/201117576.

[105] David M. Harrington and Stacey R. Sueoka. Polarization modeling and predictions for DKIST part 1: telescope and example instrument configurations. In *Advances in Optical and Mechanical Technologies for Telescopes and Instrumentation II*, volume 9912, pages 2107–2126. SPIE, Jul 2016. doi: 10.1117/12.2233176.

[106] R. A. Harrison. The nature of solar flares associated with coronal mass ejection. *Astronomy and Astrophysics*, 304:585, December 1995. ISSN 0004-6361.

[107] T. Hirayama. Theoretical model of flares and prominences. *Solar Physics*, 34 (2):323–338, February 1974. ISSN 1573-093X. doi: 10.1007/BF00153671.

[108] G. D. Holman, M. J. Aschwanden, H. Aurass, M. Battaglia, P. C. Grigis, E. P. Kontar, W. Liu, P. Saint-Hilaire, and V. V. Zharkova. Implications of X-ray Observations for Electron Acceleration and Propagation in Solar Flares. *Space Science Reviews*, 159(1):107, August 2011. ISSN 1572-9672. doi: 10.1007/s11214-010-9680-9.

[109] A. W. Hood and E. R. Priest. Critical Conditions for Magnetic Instabilities in Force-Free Coronal Loops. *Geophysical & Astrophysical Fluid Dynamics*, 17

(1):297–318, jan 1981. ISSN 10290419. doi: 10.1080/03091928108243687. URL https://www.tandfonline.com/doi/abs/10.1080/03091928108243687.

[110] M. Hoshino, T. Mukai, T. Terasawa, and I. Shinohara. Suprathermal electron acceleration in magnetic reconnection. *Journal of Geophysical Research: Space Physics*, 106(A11):25979–25997, 2001. ISSN 2156-2202. doi: 10.1029/2001JA900052.

[111] Y. J. Hou, J. Zhang, T. Li, S. H. Yang, and X. H. Li. Eruption of a multi-flux-rope system in solar active region 12673 leading to the two largest flares in Solar Cycle 24. *Astronomy & Astrophysics*, 619:A100, November 2018. ISSN 0004-6361, 1432-0746. doi: 10.1051/0004-6361/201732530.

[112] T. A. Howard, C. E. DeForest, U. G. Schneck, and C. R. Alden. Challenging Some Contemporary Views of Coronal Mass Ejections. II. The Case for Absent Filaments. *The Astrophysical Journal*, 834(1):86, January 2017. ISSN 0004-637X. doi: 10.3847/1538-4357/834/1/86.

[113] T. A. Howard, C. E. DeForest, U. G. Schneck, and C. R. Alden. Challenging Some Contemporary Views of Coronal Mass Ejections. II. The Case for Absent Filaments. *The Astrophysical Journal*, 834(1):86, January 2017. ISSN 0004-637X. doi: 10.3847/1538-4357/834/1/86.

[114] Qiang Hu, Jiong Qiu, B. Dasgupta, A. Khare, and G. M. Webb. STRUCTURES OF INTERPLANETARY MAGNETIC FLUX ROPES AND COMPARISON WITH THEIR SOLAR SOURCES. *The Astrophysical Journal*, 793(1):53, September 2014. ISSN 0004-637X. doi: 10.1088/0004-637X/793/1/53.

[115] H. S. Hudson, J. R. Lemen, O. C. St. Cyr, A. C. Sterling, and D. F. Webb. X-ray coronal changes during Halo CMEs. *Geophysical Research Letters*, 25 (14):2481–2484, 1998. ISSN 1944-8007. doi: 10.1029/98GL01303.

[116] H. S. Hudson, T. Kosugi, N. V. Nitta, and M. Shimojo. Hard X-Radiation from a Fast Coronal Ejection. , 561(2):L211–L214, November 2001. doi: 10.1086/324760.

[117] G. J. Hurford, E. J. Schmahl, R. A. Schwartz, A. J. Conway, M. J. Aschwanden, A. Csillaghy, B. R. Dennis, C. Johns-Krull, S. Krucker, R. P. Lin, J. McTiernan, T. R. Metcalf, J. Sato, and D. M. Smith. The RHESSI imaging concept. *Solar Physics*, 210(1-2):61–86, 2002. ISSN 00380938. doi: 10.1023/A:1022436213688. URL `https://ui.adsabs.harvard.edu/abs/2002SoPh..210...61H/abstract`.

[118] R. M. E. Illing and A. J. Hundhausen. Possible observation of a disconnected magnetic structure in a coronal transient. *Journal of Geophysical Research: Space Physics*, 88(A12):10210–10214, 1983. ISSN 2156-2202. doi: 10.1029/JA088iA12p10210.

[119] R. M. E. Illing and A. J. Hundhausen. Observation of a coronal transient from 1.2 to 6 solar radii. *Journal of Geophysical Research: Space Physics*, 90(A1):275–282, 1985. ISSN 2156-2202. doi: 10.1029/JA090iA01p00275.

[120] S. Inoue, K. Hayashi, D. Shiota, T. Magara, and G. S. Choe. MAGNETIC STRUCTURE PRODUCING X- AND M-CLASS SOLAR FLARES IN SOLAR ACTIVE REGION 11158. *The Astrophysical Journal*, 770(1):79, May 2013. ISSN 0004-637X. doi: 10.1088/0004-637X/770/1/79.

[121] Satoshi Inoue. Magnetohydrodynamics modeling of coronal magnetic field and solar eruptions based on the photospheric magnetic field, dec 2016. ISSN 21974284. URL `https://progearthplanetsci.springeropen.com/articles/10.1186/s40645-016-0084-7`.

[122] M. Janvier, G. Aulanier, E. Pariat, and P. Démoulin. The standard flare model in three dimensions - III. Slip-running reconnection properties. *Astronomy & Astrophysics*, 555:A77, July 2013. ISSN 0004-6361, 1432-0746. doi: 10.1051/0004-6361/201321164.

[123] David B. Jess, Veronika E. Reznikova, Robert S. I. Ryans, Damian J. Christian, Peter H. Keys, Mihalis Mathioudakis, Duncan H. Mackay, S. Krishna Prasad, Dipankar Banerjee, Samuel D. T. Grant, Sean Yau, and Conor Diamond. Solar coronal magnetic fields derived using seismology techniques applied to omnipresent sunspot waves. *Nature Physics*, 12(2):179–185, feb 2016. ISSN 1745-2473. doi: 10.1038/nphys3544. URL `http://www.nature.com/articles/nphys3544`.

[124] Chaowei Jiang, Xueshang Feng, Rui Liu, XiaoLi Yan, Qiang Hu, Ronald L. Moore, Aiying Duan, Jun Cui, Pingbing Zuo, Yi Wang, and Fengsi Wei. A fundamental mechanism of solar eruption initiation. *Nature Astronomy*, pages 1–13, July 2021. ISSN 2397-3366. doi: 10.1038/s41550-021-01414-z.

[125] Ju Jing, Jiong Qiu, Jun Lin, Ming Qu, Yan Xu, and Haimin Wang. Magnetic Reconnection Rate and Flux-Rope Acceleration of Two-Ribbon Flares. *The Astrophysical Journal*, 620(2):1085, February 2005. ISSN 0004-637X. doi: 10.1086/427165.

[126] Jack Randolph Jokipii, Charles P. Sonett, and Mark S. Giampapa. *Cosmic Winds and the Heliosphere*. University of Arizona Press, October 1997. ISBN 978-0-8165-1825-8.

[127] M. L. Kaiser, T. A. Kucera, J. M. Davila, O. C. St. Cyr, M. Guhathakurta, and E. Christian. The STEREO Mission: An Introduction. *Space Science Reviews*, 136(1):5–16, April 2008. ISSN 1572-9672. doi: 10.1007/s11214-007-9277-0.

[128] S. R. Kane, J. McTiernan, J. Loran, E. E. Fenimore, R. W. Klebesadel, and J. G. Laros. Stereoscopic Observations of a Solar Flare Hard X-Ray Source in the High Corona. , 390:687, May 1992. doi: 10.1086/171320.

[129] J. T. Karpen, S. K. Antiochos, and C. R. DeVore. THE MECHANISMS FOR THE ONSET AND EXPLOSIVE ERUPTION OF CORONAL MASS EJECTIONS AND ERUPTIVE FLARES. *The Astrophysical Journal*, 760(1): 81, November 2012. ISSN 0004-637X. doi: 10.1088/0004-637X/760/1/81.

[130] B. Kliem and T. Török. Torus instability. *Physical Review Letters*, 96(25): 255002, 2006. ISSN 00319007. doi: 10.1103/PhysRevLett.96.255002. URL `https://ui.adsabs.harvard.edu/abs/2006PhRvL..96y5002K/abstract`.

[131] B. Kliem and T. Török. Torus Instability. *Physical Review Letters*, 96(25): 255002, June 2006. doi: 10.1103/PhysRevLett.96.255002.

[132] B. Kliem, V. S. Titov, and T. Török. Formation of current sheets and sigmoidal structure by the kink instability of a magnetic loop. *Astronomy & Astrophysics*, 413(3):L23–L26, January 2004. ISSN 0004-6361, 1432-0746. doi: 10.1051/0004-6361:20031690.

[133] B. Kliem, Y. N. Su, A. A. Van Ballegooijen, and E. E. Deluca. Magnetohydrodynamic modeling of the solar eruption on 2010 April 8. *Astrophysical Journal*, 779(2):129, dec 2013. ISSN 15384357. doi: 10.1088/0004-637X/779/2/129. URL `https://ui.adsabs.harvard.edu/abs/2013ApJ...779..129K/abstract`.

[134] Bernhard Kliem, Tibor Török, Viacheslav S. Titov, Roberto Lionello, Jon A. Linker, Rui Liu, Chang Liu, and Haimin Wang. SLOW RISE AND PARTIAL ERUPTION OF A DOUBLE-DECKER FILAMENT. II. A DOUBLE FLUX

ROPE MODEL. *The Astrophysical Journal*, 792(2):107, August 2014. ISSN 0004-637X. doi: 10.1088/0004-637X/792/2/107.

[135] R. A. Kopp and G. W. Pneuman. Magnetic reconnection in the corona and the loop prominence phenomenon. *Solar Physics*, 50(1):85–98, September 1976. ISSN 1573-093X. doi: 10.1007/BF00206193.

[136] Yuankun Kou, Xin Cheng, Yulei Wang, Sijie Yu, B. Chen, Eduard P. Kontar, and Mingde Ding. Microwave imaging of quasi-periodic pulsations at flare current sheet. *Nature Communications*, 13(1):7680, December 2022. ISSN 2041-1723. doi: 10.1038/s41467-022-35377-0.

[137] K. R. Krall, J. B. Smith, M. J. Hagyard, E. A. West, and N. P. Cummings. Vector magnetic field evolution, energy storage, and associated photospheric velocity shear within a flare-productive active region. *Solar Physics*, 79(1): 59–75, July 1982. ISSN 1573-093X. doi: 10.1007/BF00146973.

[138] S. Krucker, M. Battaglia, P. J. Cargill, L. Fletcher, H. S. Hudson, A. L. MacKinnon, S. Masuda, L. Sui, M. Tomczak, A. L. Veronig, L. Vlahos, and S. M. White. Hard X-ray emission from the solar corona. *The Astronomy and Astrophysics Review*, 16(3):155–208, December 2008. ISSN 1432-0754. doi: 10.1007/s00159-008-0014-9.

[139] Säm Krucker, S. M. White, and R. P. Lin. Solar Flare Hard X-Ray Emission from the High Corona. , 669(1):L49–L52, November 2007. doi: 10.1086/523759.

[140] Säm Krucker, H. S. Hudson, L. Glesener, S. M. White, S. Masuda, J.-P. Wuelser, and R. P. Lin. Measurements of the Coronal Acceleration Region of a Solar Flare. *The Astrophysical Journal*, 714(2):1108, April 2010. ISSN 0004-637X. doi: 10.1088/0004-637X/714/2/1108.

[141] Säm Krucker, Steven Christe, Lindsay Glesener, Shin-nosuke Ishikawa, Stephen McBride, David Glaser, Paul Turin, R. P. Lin, Mikhail Gubarev, Brian Ramsey, Shinya Saito, Yasuyuki Tanaka, Tadayuki Takahashi, Shin Watanabe, Takaaki Tanaka, Hiroyasu Tajima, and Satoshi Masuda. The Focusing Optics X-ray Solar Imager (FOXSI). In *Optics for EUV, X-Ray, and Gamma-Ray Astronomy V*, volume 8147, pages 45–58. SPIE, October 2011. doi: 10.1117/12.895271.

[142] Säm Krucker, H. S. Hudson, N. L. S. Jeffrey, M. Battaglia, E. P. Kontar, A. O. Benz, A. Csillaghy, and R. P. Lin. High-resolution Imaging of Solar Flare Ribbons and Its Implication on the Thick-target Beam Model. *The Astrophysical Journal*, 739:96, October 2011. ISSN 0004-637X. doi: 10.1088/0004-637X/739/2/96.

[143] Säm Krucker, G. J. Hurford, O. Grimm, S. Kögl, H.-P. Gröbelbauer, L. Etesi, D. Casadei, A. Csillaghy, A. O. Benz, N. G. Arnold, F. Molendini, P. Orleanski, D. Schori, H. Xiao, M. Kuhar, N. Hochmuth, S. Felix, F. Schramka, S. Marcin, S. Kobler, L. Iseli, M. Dreier, H. J. Wiehl, L. Kleint, M. Battaglia, E. Lastufka, H. Sathiapal, K. Lapadula, M. Bednarzik, G. Birrer, St Stutz, Ch Wild, F. Marone, K. R. Skup, A. Cichocki, K. Ber, K. Rutkowski, W. Bujwan, G. Juchnikowski, M. Winkler, M. Darmetko, M. Michalska, K. Seweryn, A. Białek, P. Osica, J. Sylwester, M. Kowalinski, D. Ścisłowski, M. Siarkowski, M. Steślicki, T. Mrozek, P. Podgórski, A. Meuris, O. Limousin, O. Gevin, I. Le Mer, S. Brun, A. Strugarek, N. Vilmer, S. Musset, M. Maksimović, F. Fárník, Z. Kozáček, J. Kašparová, G. Mann, H. Önel, A. Warmuth, J. Rendtel, J. Anderson, S. Bauer, F. Dionies, J. Paschke, D. Plüschke, M. Woche, F. Schuller, A. M. Veronig, E. C. M. Dickson, P. T. Gallagher, S. A. Maloney, D. S. Bloomfield, M. Piana, A. M. Massone, F. Benvenuto, P. Massa, R. A. Schwartz, B. R. Dennis, H. F. van Beek, J. Rodríguez-Pacheco, and R. P.

Lin. The Spectrometer/Telescope for Imaging X-rays (STIX). *Astronomy & Astrophysics*, 642:A15, October 2020. ISSN 0004-6361, 1432-0746. doi: 10.1051/0004-6361/201937362.

[144] M. Kuperus and M. A. Raadu. The Support of Prominences Formed in Neutral Sheets. *Astronomy and Astrophysics*, 31:189, March 1974. ISSN 0004-6361.

[145] D. Kuridze, M. Mathioudakis, H. Morgan, R. Oliver, L. Kleint, T. V. Zaqarashvili, A. Reid, J. Koza, M. G. Löfdahl, T. Hillberg, V. Kukhianidze, and A. Hanslmeier. Mapping the Magnetic Field of Flare Coronal Loops. , 874 (2):126, April 2019. doi: 10.3847/1538-4357/ab08e9.

[146] Alexey A. Kuznetsov and Gregory D. Fleishman. Ultimate Fast Gyrosynchrotron Codes. *The Astrophysical Journal*, 922(2):103, November 2021. ISSN 0004-637X. doi: 10.3847/1538-4357/ac29c0.

[147] E. Landi, W. Li, T. Brage, and R. Hutton. Hinode/EIS Coronal Magnetic Field Measurements at the Onset of a C2 Flare. , 913(1):1, May 2021. doi: 10.3847/1538-4357/abf6d1.

[148] James R. Lemen, Alan M. Title, David J. Akin, Paul F. Boerner, Catherine Chou, Jerry F. Drake, Dexter W. Duncan, Christopher G. Edwards, Frank M. Friedlaender, Gary F. Heyman, Neal E. Hurlburt, Noah L. Katz, Gary D. Kushner, Michael Levay, Russell W. Lindgren, Dnyanesh P. Mathur, Edward L. McFeaters, Sarah Mitchell, Roger A. Rehse, Carolus J. Schrijver, Larry A. Springer, Robert A. Stern, Theodore D. Tarbell, Jean-Pierre Wuelser, C. Jacob Wolfson, Carl Yanari, Jay A. Bookbinder, Peter N. Cheimets, David Caldwell, Edward E. Deluca, Richard Gates, Leon Golub, Sang Park, William A. Podgorski, Rock I. Bush, Philip H. Scherrer, Mark A. Gummin, Peter Smith, Gary Auker, Paul Jerram, Peter Pool, Regina Soufli, David L. Windt,

Sarah Beardsley, Matthew Clapp, James Lang, and Nicholas Waltham. The Atmospheric Imaging Assembly (AIA) on the Solar Dynamics Observatory (SDO). *Solar Physics*, 275(1):17–40, January 2012. ISSN 1573-093X. doi: 10.1007/s11207-011-9776-8.

[149] James R. Lemen, Alan M. Title, David J. Akin, Paul F. Boerner, Catherine Chou, Jerry F. Drake, Dexter W. Duncan, Christopher G. Edwards, Frank M. Friedlaender, Gary F. Heyman, Neal E. Hurlburt, Noah L. Katz, Gary D. Kushner, Michael Levay, Russell W. Lindgren, Dnyanesh P. Mathur, Edward L. McFeaters, Sarah Mitchell, Roger A. Rehse, Carolus J. Schrijver, Larry A. Springer, Robert A. Stern, Theodore D. Tarbell, Jean-Pierre Wuelser, C. Jacob Wolfson, Carl Yanari, Jay A. Bookbinder, Peter N. Cheimets, David Caldwell, Edward E. Deluca, Richard Gates, Leon Golub, Sang Park, William A. Podgorski, Rock I. Bush, Philip H. Scherrer, Mark A. Gummin, Peter Smith, Gary Auker, Paul Jerram, Peter Pool, Regina Soufli, David L. Windt, Sarah Beardsley, Matthew Clapp, James Lang, and Nicholas Waltham. The Atmospheric Imaging Assembly (AIA) on the Solar Dynamics Observatory (SDO). *Solar Physics*, 275:17–40, January 2012. ISSN 0038-0938. doi: 10.1007/s11207-011-9776-8.

[150] J. L. Leroy, V. Bommier, and S. Sahal-Brechot. New data on the magnetic structure of quiescent prominences. *Astronomy and Astrophysics*, 131(1):33–44, February 1984. ISSN 0004-6361.

[151] Xiaocan Li, Fan Guo, Hui Li, and Gang Li. Particle Acceleration during Magnetic Reconnection in a Low-beta Plasma. *The Astrophysical Journal*, 843 (1):21, June 2017. ISSN 0004-637X. doi: 10.3847/1538-4357/aa745e.

[152] Xiaocan Li, Fan Guo, Hui Li, and Shengtai Li. Large-scale Compression Acceleration during Magnetic Reconnection in a Low-β Plasma. *The*

Astrophysical Journal, 866(1):4, October 2018. ISSN 0004-637X. doi: 10.3847/1538-4357/aae07b.

[153] Xiaocan Li, Fan Guo, B. Chen, Chengcai Shen, and Lindsay Glesener. Modeling Electron Acceleration and Transport in the Early Impulsive Phase of the 2017 September 10th Solar Flare. *The Astrophysical Journal*, 932(2):92, June 2022. ISSN 0004-637X. doi: 10.3847/1538-4357/ac6efe.

[154] H. Lin, J. R. Kuhn, and R. Coulter. Coronal magnetic field measurements. *The Astrophysical Journal*, 613(2):L177–L180, aug 2004. doi: 10.1086/425217. URL `https://doi.org/10.1086%2F425217`.

[155] J. Lin and T. G. Forbes. Effects of reconnection on the coronal mass ejection process. *Journal of Geophysical Research: Space Physics*, 105(A2):2375–2392, 2000. ISSN 2156-2202. doi: 10.1029/1999JA900477.

[156] J. Lin, Y.-K. Ko, L. Sui, J. C. Raymond, G. A. Stenborg, Y. Jiang, S. Zhao, and S. Mancuso. Direct Observations of the Magnetic Reconnection Site of an Eruption on 2003 November 18. *The Astrophysical Journal*, 622(2):1251, April 2005. ISSN 0004-637X. doi: 10.1086/428110.

[157] R.P. Lin, B.R. Dennis, G.J. Hurford, D.M. Smith, A. Zehnder, P.R. Harvey, D.W. Curtis, D. Pankow, P. Turin, M. Bester, A. Csillaghy, M. Lewis, N. Madden, H.F. van Beek, M. Appleby, T. Raudorf, J. McTiernan, R. Ramaty, E. Schmahl, R. Schwartz, S. Krucker, R. Abiad, T. Quinn, P. Berg, M. Hashii, R. Sterling, R. Jackson, R. Pratt, R.D. Campbell, D. Malone, D. Landis, C.P. Barrington-Leigh, S. Slassi-Sennou, C. Cork, D. Clark, D. Amato, L. Orwig, R. Boyle, I.S. Banks, K. Shirey, A.K. Tolbert, D. Zarro, F. Snow, K. Thomsen, R. Henneck, A. Mchedlishvili, P. Ming, M. Fivian, John Jordan, Richard Wanner, Jerry Crubb, J. Preble, M. Matranga, A. Benz, H. Hudson, R.C.

Canfield, G.D. Holman, C. Crannell, T. Kosugi, A.G. Emslie, N. Vilmer, J.C. Brown, C. Johns-Krull, M. Aschwanden, T. Metcalf, and A. Conway. The Reuven Ramaty High-Energy Solar Spectroscopic Imager (RHESSI). *Solar Physics*, 210(1):3–32, November 2002. ISSN 1573-093X. doi: 10.1023/A:1022428818870.

[158] Chang Liu and Haimin Wang. RECONNECTION ELECTRIC FIELD AND HARDNESS OF X-RAY EMISSION OF SOLAR FLARES. *The Astrophysical Journal*, 696(1):L27, April 2009. ISSN 0004-637X. doi: 10.1088/0004-637X/696/1/L27.

[159] Chang Liu, Jeongwoo Lee, Ju Jing, Rui Liu, Na Deng, and Haimin Wang. MOTIONS OF HARD X-RAY SOURCES DURING AN ASYMMETRIC ERUPTION. *The Astrophysical Journal Letters*, 721(2):L193, September 2010. ISSN 2041-8205. doi: 10.1088/2041-8205/721/2/L193.

[160] Rui Liu. Magnetic flux ropes in the solar corona: Structure and evolution toward eruption. *Research in Astronomy and Astrophysics*, 20(10):165, October 2020. ISSN 1674-4527. doi: 10.1088/1674-4527/20/10/165.

[161] Rui Liu and Haimin Wang. CORONAL IMPLOSION AND PARTICLE ACCELERATION IN THE WAKE OF A FILAMENT ERUPTION. *The Astrophysical Journal*, 703(1):L23, August 2009. ISSN 0004-637X. doi: 10.1088/0004-637X/703/1/L23.

[162] Rui Liu, Holly R. Gilbert, David Alexander, and Yingna Su. The Effect of Magnetic Reconnection and Writhing in a Partial Filament Eruption. *The Astrophysical Journal*, 680(2):1508, June 2008. ISSN 0004-637X. doi: 10.1086/587482.

[163] Rui Liu, David Alexander, and Holly R. Gilbert. ASYMMETRIC ERUPTIVE FILAMENTS. *The Astrophysical Journal*, 691(2):1079, February 2009. ISSN 0004-637X. doi: 10.1088/0004-637X/691/2/1079.

[164] Rui Liu, Viacheslav S. Titov, Tingyu Gou, Yuming Wang, Kai Liu, and Haimin Wang. AN UNORTHODOX X-CLASS LONG-DURATION CONFINED FLARE. *The Astrophysical Journal*, 790(1):8, June 2014. ISSN 0004-637X. doi: 10.1088/0004-637X/790/1/8.

[165] Rui Liu, Bernhard Kliem, Viacheslav S. Titov, Jun Chen, Yuming Wang, Haimin Wang, Chang Liu, Yan Xu, and Thomas Wiegelmann. STRUCTURE, STABILITY, AND EVOLUTION OF MAGNETIC FLUX ROPES FROM THE PERSPECTIVE OF MAGNETIC TWIST. *The Astrophysical Journal*, 818(2):148, feb 2016. ISSN 1538-4357. doi: 10.3847/0004-637X/818/2/148. URL `https://iopscience.iop.org/article/10.3847/0004-637X/818/2/148`.

[166] Rui Liu, Bernhard Kliem, Viacheslav S. Titov, Jun Chen, Yuming Wang, Haimin Wang, Chang Liu, Yan Xu, and Thomas Wiegelmann. Structure, Stability, And Evolution of Magnetic Flux Ropes From the Perspective of Magnetic Twist. *The Astrophysical Journal*, 818(2):148, February 2016. ISSN 0004-637X. doi: 10.3847/0004-637X/818/2/148.

[167] Tie Liu and Yingna Su. Tether-cutting and Overlying Magnetic Reconnections in an MHD Simulation of Prominence-cavity System. *The Astrophysical Journal*, 915(1):55, July 2021. ISSN 0004-637X. doi: 10.3847/1538-4357/ac013a.

[168] B. C. Low. Magnetic field configurations associated with polarity intrusion in a solar active region. *Solar Physics*, 77(1):43–61, April 1982. ISSN 1573-093X.

doi: 10.1007/BF00156094.

[169] B. C. Low. Magnetohydrodynamic processes in the solar corona: Flares, coronal mass ejections, and magnetic helicity*. *Physics of Plasmas*, 1(5):1684–1690, May 1994. ISSN 1070-664X. doi: 10.1063/1.870671.

[170] T. Magara, S. Mineshige, T. Yokoyama, and K. Shibata. Numerical Simulation of Magnetic Reconnection in Eruptive Flares. In Yutaka Uchida, Takeo Kosugi, and Hugh S. Hudson, editors, *Magnetodynamic Phenomena in the Solar Atmosphere: Prototypes of Stellar Magnetic Activity*, pages 585–586. Springer, Netherlands, Dordrecht, 1996. ISBN 978-94-009-0315-9. doi: 10.1007/978-94-009-0315-9_151.

[171] Dalmiro Jorge Filipe Maia, Ricardo Gama, Claude Mercier, Monique Pick, Alain Kerdraon, and Marian Karlický. The Radio-Coronal Mass Ejection Event on 2001 April 15. , 660(1):874–881, May 2007. doi: 10.1086/508011.

[172] Darije Maričić, Bojan Vršnak, Andrew L. Stanger, Astrid M. Veronig, Manuela Temmer, and Dragan Roša. Acceleration Phase of Coronal Mass Ejections: II. Synchronization of the Energy Release in the Associated Flare. *Solar Physics*, 241(1):99–112, March 2007. ISSN 1573-093X. doi: 10.1007/s11207-007-0291-x.

[173] Juan-Carlos Martínez Oliveros, Hugh S. Hudson, Gordon J. Hurford, Säm Krucker, R. P. Lin, Charles Lindsey, Sebastien Couvidat, Jesper Schou, and W. T. Thompson. The Height of a White-light Flare and Its Hard X-Ray Sources. *The Astrophysical Journal*, 753:L26, July 2012. ISSN 0004-637X. doi: 10.1088/2041-8205/753/2/L26.

[174] S. Masuda, T. Kosugi, H. Hara, S. Tsuneta, and Y. Ogawara. A loop-top hard X-ray source in a compact solar flare as evidence for magnetic reconnection.

Nature, 371(6497):495–497, October 1994. ISSN 1476-4687. doi: 10.1038/371495a0.

[175] Alan Maxwell, Murray Dryer, and Patrick McIntosh. A piston-driven shock in the solar corona. *Solar Physics*, 97(2):401–413, June 1985. ISSN 1573-093X. doi: 10.1007/BF00165999.

[176] J. P. McMullin, B. Waters, D. Schiebel, W. Young, and K. Golap. CASA Architecture and Applications. *Astronomical Data Analysis Software and Systems XVI*, 376:127, Oct 2007. ISSN 1050-3390. URL `https://ui.adsabs.harvard.edu/abs/2007ASPC..376..127M/abstract`.

[177] James M. McTiernan, George H. Fisher, and Peng Li. The Solar Flare Soft X-Ray Differential Emission Measure and the Neupert Effect at Different Temperatures. *The Astrophysical Journal*, 514(1):472, March 1999. ISSN 0004-637X. doi: 10.1086/306924.

[178] Charles Meegan, Giselher Lichti, P. N. Bhat, Elisabetta Bissaldi, Michael S. Briggs, Valerie Connaughton, Roland Diehl, Gerald Fishman, Jochen Greiner, Andrew S. Hoover, Alexander J. van der Horst, Andreas von Kienlin, R. Marc Kippen, Chryssa Kouveliotou, Sheila McBreen, W. S. Paciesas, Robert Preece, Helmut Steinle, Mark S. Wallace, Robert B. Wilson, and Colleen Wilson-Hodge. THE FERMI GAMMA-RAY BURST MONITOR. *The Astrophysical Journal*, 702(1):791, August 2009. ISSN 0004-637X. doi: 10.1088/0004-637X/702/1/791.

[179] D. B. Melrose. Collective Plasma Radiation Processes. *Annual Review of Astronomy and Astrophysics*, 29(1):31–57, 1991. doi: 10.1146/annurev.aa.29.090191.000335.

[180] D. B. Melrose. Coherent emission mechanisms in astrophysical plasmas. *Reviews of Modern Plasma Physics*, 1(1):5, July 2017. ISSN 2367-3192. doi: 10.1007/s41614-017-0007-0.

[181] L. Merenda, J. Trujillo Bueno, E. Landi Degl'Innocenti, and M. Collados. Determination of the Magnetic Field Vector via the Hanle and Zeeman Effects in the He i λ10830 Multiplet: Evidence for Nearly Vertical Magnetic Fields in a Polar Crown Prominence . *The Astrophysical Journal*, 642(1):554–561, may 2006. ISSN 0004-637X. doi: 10.1086/501038. URL https://iopscience.iop.org/article/10.1086/501038https://iopscience.iop.org/article/10.1086/501038/meta.

[182] Thomas R. Metcalf, Marc L. DeRosa, Carolus J. Schrijver, Graham Barnes, Adriaan A. van Ballegooijen, Thomas Wiegelmann, Michael S. Wheatland, Gherardo Valori, and James M. McTtiernan. Nonlinear force-free modeling of coronal magnetic fields. ii. modeling a filament arcade and simulated chromospheric and photospheric vector fields. *Solar Physics*, 247(2):269–299, Feb 2008. ISSN 1573-093X. doi: 10.1007/s11207-007-9110-7. URL https://doi.org/10.1007/s11207-007-9110-7.

[183] Surajit Mondal, Divya Oberoi, and Angelos Vourlidas. Estimation of the Physical Parameters of a CME at High Coronal Heights Using Low-frequency Radio Observations. , 893(1):28, April 2020. doi: 10.3847/1538-4357/ab7fab.

[184] R. L. Moore and B. J. Labonte. The filament eruption in the 3B flare of July 29, 1973 - Onset and magnetic field configuration. *IAUS*, 91:207–210, 1980. ISSN 1743-9221. URL https://ui.adsabs.harvard.edu/abs/1980IAUS...91..207M/abstract.

[185] Ronald L. Moore, Alphonse C. Sterling, Hugh S. Hudson, and James R. Lemen. Onset of the Magnetic Explosion in Solar Flares and Coronal Mass Ejections. *The Astrophysical Journal*, 552(2):833–848, may 2001. ISSN 0004-637X. doi: 10.1086/320559. URL `https://ui.adsabs.harvard.edu/abs/2001ApJ...552..833M/abstract`.

[186] Huw Morgan and Miloslav Druckmüller. Multi-Scale Gaussian Normalization for Solar Image Processing. *Solar Physics*, 289(8):2945–2955, apr 2014. ISSN 1573093X. doi: 10.1007/s11207-014-0523-9. URL `https://link.springer.com/article/10.1007/s11207-014-0523-9`.

[187] D. E. Morosan, E. K. J. Kilpua, E. P. Carley, and C. Monstein. Variable emission mechanism of a Type IV radio burst. , 623:A63, March 2019. doi: 10.1051/0004-6361/201834510.

[188] D. Müller, O. C. St Cyr, I. Zouganelis, H. R. Gilbert, R. Marsden, T. Nieves-Chinchilla, E. Antonucci, F. Auchère, D. Berghmans, T. S. Horbury, R. A. Howard, S. Krucker, M. Maksimovic, C. J. Owen, P. Rochus, J. Rodriguez-Pacheco, M. Romoli, S. K. Solanki, R. Bruno, M. Carlsson, A. Fludra, L. Harra, D. M. Hassler, S. Livi, P. Louarn, H. Peter, U. Schühle, L. Teriaca, J. C. del Toro Iniesta, R. F. Wimmer-Schweingruber, E. Marsch, M. Velli, A. De Groof, A. Walsh, and D. Williams. The Solar Orbiter mission - Science overview. *Astronomy & Astrophysics*, 642:A1, October 2020. ISSN 0004-6361, 1432-0746. doi: 10.1051/0004-6361/202038467.

[189] Valery M. Nakariakov and Erwin Verwichte. Coronal Waves and Oscillations. *Living Rev. Sol. Phys.*, 2(1):3–65, May 2005. ISSN 1614-4961. doi: 10.12942/lrsp-2005-3.

[190] S. J. Naus, J. Qiu, C. R. DeVore, S. K. Antiochos, J. T. Dahlin, J. F. Drake, and M. Swisdak. Correlated Spatio-temporal Evolution of Extreme-Ultraviolet Ribbons and Hard X-Rays in a Solar Flare. *The Astrophysical Journal*, 926(2): 218, February 2022. ISSN 0004-637X. doi: 10.3847/1538-4357/ac4028.

[191] Werner M. Neupert. Comparison of Solar X-Ray Line Emission with Microwave Emission during Flares. *The Astrophysical Journal*, 153:L59, July 1968. ISSN 0004-637X. doi: 10.1086/180220.

[192] A. Nindos, S. Patsourakos, A. Vourlidas, and C. Tagikas. HOW COMMON ARE HOT MAGNETIC FLUX ROPES IN THE LOW SOLAR CORONA? A STATISTICAL STUDY OF EUV OBSERVATIONS. *The Astrophysical Journal*, 808(2):117, July 2015. ISSN 0004-637X. doi: 10.1088/0004-637X/808/2/117.

[193] Gelu M. Nita, Jack Hickish, David MacMahon, and Dale E. Gary. EOVSA Implementation of a Spectral Kurtosis Correlator for Transient Detection and Classification. *Journal of Astronomical Instrumentation*, 05(04):1641009, dec 2016. ISSN 2251-1717. doi: 10.1142/S2251171716410099. URL `https://www.worldscientific.com/doi/abs/10.1142/S2251171716410099`.

[194] E. N. Parker. Sweet's mechanism for merging magnetic fields in conducting fluids. *Journal of Geophysical Research (1896-1977)*, 62(4):509–520, 1957. ISSN 2156-2202. doi: 10.1029/JZ062i004p00509.

[195] W. Pesnell, B. Thompson, and P. Chamberlin. The Solar Dynamics Observatory (SDO). *Solar Physics*, 275(1):3–15, 2012. ISSN 0038-0938. doi: 10.1007/s11207-011-9841-3.

[196] V. Petrosian. Impulsive solar X-ray bursts: Bremsstrahlung radiation from a beam of electrons in the solar chromosphere and the total energy of solar flares. Technical Report SU-IPR-528, June 1973.

[197] E. R. Priest and P. Démoulin. Three-dimensional magnetic reconnection without null points: 1. Basic theory of magnetic flipping. *Journal of Geophysical Research: Space Physics*, 100(A12):23443–23463, 1995. ISSN 2156-2202. doi: 10.1029/95JA02740.

[198] E. R. Priest, G. Hornig, and D. I. Pontin. On the nature of three-dimensional magnetic reconnection. *Journal of Geophysical Research: Space Physics*, 108 (A7), 2003. ISSN 2156-2202. doi: 10.1029/2002JA009812.

[199] Eric Priest and Terry Forbes. *Magnetic Reconnection: MHD Theory and Applications*. Cambridge University Press, Cambridge, 2000. ISBN 978-0-521-03394-7. doi: 10.1017/CBO9780511525087.

[200] P. L. Pritchett. Relativistic electron production during guide field magnetic reconnection. *Journal of Geophysical Research: Space Physics*, 111(A10), 2006. ISSN 2156-2202. doi: 10.1029/2006JA011793.

[201] P. L. Pritchett and F. V. Coroniti. Three-dimensional collisionless magnetic reconnection in the presence of a guide field. *Journal of Geophysical Research: Space Physics*, 109(A1), 2004. ISSN 2156-2202. doi: 10.1029/2003JA009999.

[202] J. Qiu and J. Cheng. Properties and Energetics of Magnetic Reconnection: I. Evolution of Flare Ribbons. *Solar Physics*, 297(7):80, July 2022. ISSN 1573-093X. doi: 10.1007/s11207-022-02003-7.

[203] Jiong Qiu, Haimin Wang, C. Z. Cheng, and Dale E. Gary. Magnetic Reconnection and Mass Acceleration in Flare-Coronal Mass Ejection Events.

The Astrophysical Journal, 604(2):900, April 2004. ISSN 0004-637X. doi: 10.1086/382122.

[204] Jiong Qiu, WenJuan Liu, Nicholas Hill, and Maria Kazachenko. RECONNECTION AND ENERGETICS IN TWO-RIBBON FLARES: A REVISIT OF THE BASTILLE-DAY FLARE. *The Astrophysical Journal*, 725 (1):319, November 2010. ISSN 0004-637X. doi: 10.1088/0004-637X/725/1/319.

[205] Jiong Qiu, Dana W. Longcope, Paul A. Cassak, and Eric R. Priest. Elongation of Flare Ribbons. *The Astrophysical Journal*, 838(1):17, March 2017. ISSN 0004-637X. doi: 10.3847/1538-4357/aa6341.

[206] Jiong Qiu, Dana W. Longcope, Paul A. Cassak, and Eric R. Priest. Elongation of Flare Ribbons. *The Astrophysical Journal*, 838(1):17, March 2017. ISSN 0004-637X. doi: 10.3847/1538-4357/aa6341.

[207] Reuven Ramaty. Gyrosynchrotron Emission and Absorption in a Magnetoactive Plasma. *The Astrophysical Journal*, 158:753, November 1969. ISSN 0004-637X. doi: 10.1086/150235.

[208] Nour E. Raouafi, Pete Riley, Sarah Gibson, Silvano Fineschi, and Sami K. Solanki. Diagnostics of Coronal Magnetic Fields through the Hanle Effect in UV and IR Lines. *Front. Astron. Space Sci.*, 0, 2016. ISSN 2296-987X. doi: 10.3389/fspas.2016.00020.

[209] Katharine K. Reeves. The Relationship between Flux Rope Acceleration and Thermal Energy Release in a Model of Eruptive Solar Phenomena. *The Astrophysical Journal*, 644(1):592, June 2006. ISSN 0004-637X. doi: 10.1086/503352.

[210] Katharine K. Reeves and Stephanie J. Moats. RELATING CORONAL MASS EJECTION KINEMATICS AND THERMAL ENERGY RELEASE

TO FLARE EMISSIONS USING A MODEL OF SOLAR ERUPTIONS. *The Astrophysical Journal*, 712(1):429, March 2010. ISSN 0004-637X. doi: 10.1088/0004-637X/712/1/429.

[211] Pete Riley, Roberto Lionello, Zoran Mikić, and Jon Linker. Using Global Simulations to Relate the Three-Part Structure of Coronal Mass Ejections to In Situ Signatures. *The Astrophysical Journal*, 672(2):1221, January 2008. ISSN 0004-637X. doi: 10.1086/523893.

[212] Takashi Sakurai. Calculation of force-free magnetic field with non-constant α. *Solar Physics*, 69(2):343–359, February 1981. ISSN 1573-093X. doi: 10.1007/BF00149999.

[213] P. H. Scherrer, J. Schou, R. I. Bush, A. G. Kosovichev, R. S. Bogart, J. T. Hoeksema, Y. Liu, T. L. Duvall, J. Zhao, A. M. Title, C. J. Schrijver, T. D. Tarbell, and S. Tomczyk. The Helioseismic and Magnetic Imager (HMI) Investigation for the Solar Dynamics Observatory (SDO). *Solar Physics*, 275: 207–227, January 2012. ISSN 0038-0938. doi: 10.1007/s11207-011-9834-2.

[214] P. H. Scherrer, J. Schou, R. I. Bush, A. G. Kosovichev, R. S. Bogart, J. T. Hoeksema, Y. Liu, T. L. Duvall, J. Zhao, A. M. Title, C. J. Schrijver, T. D. Tarbell, and S. Tomczyk. The Helioseismic and Magnetic Imager (HMI) Investigation for the Solar Dynamics Observatory (SDO). *Solar Physics*, 275 (1):207–227, January 2012. ISSN 1573-093X. doi: 10.1007/s11207-011-9834-2.

[215] Carolus J. Schrijver, Christopher Elmore, Bernhard Kliem, Tibor Török, and Alan M. Title. Observations and Modeling of the Early Acceleration Phase of Erupting Filaments Involved in Coronal Mass Ejections. *The Astrophysical Journal*, 674(1):586, February 2008. ISSN 0004-637X. doi: 10.1086/524294.

[216] N. R. Sheeley Jr., J. H. Walters, Y.-M. Wang, and R. A. Howard. Continuous tracking of coronal outflows: Two kinds of coronal mass ejections. *Journal of Geophysical Research: Space Physics*, 104(A11):24739–24767, 1999. ISSN 2156-2202. doi: 10.1029/1999JA900308.

[217] H. Q. Song, J. Zhang, X. Cheng, Y. Chen, R. Liu, Y. M. Wang, and B. Li. Temperature Evolution of a Magnetic Flux Rope in a Failed Solar Eruption. *The Astrophysical Journal*, 784(1):48, March 2014. ISSN 0004-637X. doi: 10.1088/0004-637X/784/1/48.

[218] H. Q. Song, J. Zhang, X. Cheng, L. P. Li, Y. Z. Tang, B. Wang, R. S. Zheng, and Y. Chen. On the Nature of the Bright Core of Solar Coronal Mass Ejections. *The Astrophysical Journal*, 883(1):43, September 2019. ISSN 0004-637X. doi: 10.3847/1538-4357/ab304c.

[219] H. Q. Song, J. Zhang, L. P. Li, Y. D. Liu, B. Zhu, B. Wang, R. S. Zheng, and Y. Chen. The Structure of Solar Coronal Mass Ejections in the Extreme-ultraviolet Passbands. *The Astrophysical Journal*, 887(2):124, December 2019. ISSN 0004-637X. doi: 10.3847/1538-4357/ab50b6.

[220] Alphonse C. Sterling, Louise K. Harra, and Ronald L. Moore. New Evidence for the Role of Emerging Flux in a Solar Filament's Slow Rise Preceding Its CME-producing Fast Eruption. *The Astrophysical Journal*, 669(2):1359, November 2007. ISSN 0004-637X. doi: 10.1086/520829.

[221] Alphonse C. Sterling, Ronald L. Moore, and Samuel L. Freeland. INSIGHTS INTO FILAMENT ERUPTION ONSET FROM SOLAR DYNAMICS OBSERVATORY OBSERVATIONS. *The Astrophysical Journal Letters*, 731 (1):L3, March 2011. ISSN 2041-8205. doi: 10.1088/2041-8205/731/1/L3.

[222] Alphonse C. Sterling, Ronald L. Moore, David A. Falconer, and Mitzi Adams. Small-scale filament eruptions as the driver of X-ray jets in solar coronal holes. *Nature*, 523(7561):437–440, July 2015. ISSN 1476-4687. doi: 10.1038/nature14556.

[223] R. T. Stewart, G. A. Dulk, K. V. Sheridan, L. L. House, W. J. Wagner, R. Illing, and C. Sawyer. Visible light observations of a dense plasmoid associated with a moving Type IV solar radio burst. *Astron. Astrophys.*, 116(2):217–223, Dec 1982. ISSN 0004-6361. URL `https://ui.adsabs.harvard.edu/abs/1982A%26A...116..217S/abstract`.

[224] P. A. Sturrock. Model of the High-Energy Phase of Solar Flares. *Nature*, 211 (5050):695–697, August 1966. ISSN 1476-4687. doi: 10.1038/211695a0.

[225] Xudong Sun. On the Coordinate System of Space-Weather HMI Active Region Patches (SHARPs): A Technical Note. *arXiv e-prints*, page arXiv:1309.2392, Sep 2013. URL `https://ui.adsabs.harvard.edu/abs/2013arXiv1309.2392S/abstract`.

[226] Xudong Sun and Aimee A. Norton. Super-flaring Active Region 12673 Has One of the Fastest Magnetic Flux Emergence Ever Observed. *Res. Notes AAS*, 1(1): 24, Nov 2017. ISSN 2515-5172. doi: 10.3847/2515-5172/aa9be9.

[227] Einar Tandberg-Hanssen and A. Gordon Emslie. *The Physics of Solar Flares*. Cambridge University Press, November 1988. ISBN 978-0-521-30804-5.

[228] M. Temmer, A. M. Veronig, B. Vršnak, and C. Miklenic. Energy Release Rates along Hα Flare Ribbons and the Location of Hard X-Ray Sources. *The Astrophysical Journal*, 654(1):665, January 2007. ISSN 0004-637X. doi: 10.1086/509634.

[229] M. Temmer, A. M. Veronig, B. Vršnak, J. Rybák, P. Gömöry, S. Stoiser, and D. Maričić. Acceleration in Fast Halo CMEs and Synchronized Flare HXR Bursts. *The Astrophysical Journal*, 673(1):L95, January 2008. ISSN 0004-637X. doi: 10.1086/527414.

[230] V. S. Titov and P. Démoulin. Basic topology of twisted magnetic configurations in solar flares. *Astronomy and Astrophysics*, 351:707–720, November 1999. ISSN 0004-6361.

[231] Vyacheslav S. Titov, Gunnar Hornig, and Pascal Démoulin. Theory of magnetic connectivity in the solar corona. *Journal of Geophysical Research: Space Physics*, 107(A8):SSH 3–1–SSH 3–13, 2002. ISSN 2156-2202. doi: 10.1029/2001JA000278.

[232] M. Tomczak. The analysis of hard X-ray radiation of flares with occulted footpoints. *Astronomy & Astrophysics*, 366(1):294–305, January 2001. ISSN 0004-6361, 1432-0746. doi: 10.1051/0004-6361:20000204.

[233] Shin Toriumi and Haimin Wang. Flare-productive active regions. *Living Reviews in Solar Physics*, 16(1):3, May 2019. ISSN 1614-4961. doi: 10.1007/s41116-019-0019-7.

[234] T. Török and B. Kliem. Confined and Ejective Eruptions of Kink-unstable Flux Ropes. *The Astrophysical Journal*, 630(1):L97–L100, sep 2005. ISSN 0004-637X. doi: 10.1086/462412. URL `https://ui.adsabs.harvard.edu/abs/2005ApJ...630L..97T/abstract`.

[235] D. Tripathi, H. Isobe, and H. E. Mason. On the propagation of brightening after filament/prominence eruptions, as seen by SoHO-EIT. *Astronomy & Astrophysics*, 453(3):1111–1116, July 2006. ISSN 0004-6361, 1432-0746. doi: 10.1051/0004-6361:20064993.

[236] Samuel D. Tun and A. Vourlidas. Derivation of the Magnetic Field in a Coronal Mass Ejection Core via Multi-frequency Radio Imaging. , 766(2):130, April 2013. doi: 10.1088/0004-637X/766/2/130.

[237] A. Veronig, B. Vrsnak, B. R. Dennis, M. Temmer, A. Hanslmeier, and J. Magdalenic. Investigation of the Neupert effect in solar flares. I. Statistical properties and the evaporation model. *Astronomy & Astrophysics*, 392(2): 699–712, September 2002. ISSN 0004-6361, 1432-0746. doi: 10.1051/0004-6361: 20020947.

[238] Astrid M. Veronig and John C. Brown. A Coronal Thick-Target Interpretation of Two Hard X-Ray Loop Events. *The Astrophysical Journal*, 603(2):L117, February 2004. ISSN 0004-637X. doi: 10.1086/383199.

[239] Astrid M. Veronig, Tatiana Podladchikova, Karin Dissauer, Manuela Temmer, Daniel B. Seaton, David Long, Jingnan Guo, Bojan Vršnak, Louise Harra, and Bernhard Kliem. Genesis and Impulsive Evolution of the 2017 September 10 Coronal Mass Ejection. *The Astrophysical Journal*, 868(2):107, November 2018. ISSN 0004-637X. doi: 10.3847/1538-4357/aaeac5.

[240] Pauli Virtanen, Ralf Gommers, Travis E. Oliphant, Matt Haberland, Tyler Reddy, David Cournapeau, Evgeni Burovski, Pearu Peterson, Warren Weckesser, Jonathan Bright, Stéfan J. van der Walt, Matthew Brett, Joshua Wilson, K. Jarrod Millman, Nikolay Mayorov, Andrew R. J. Nelson, Eric Jones, Robert Kern, Eric Larson, C J Carey, İlhan Polat, Yu Feng, Eric W. Moore, Jake VanderPlas, Denis Laxalde, Josef Perktold, Robert Cimrman, Ian Henriksen, E. A. Quintero, Charles R. Harris, Anne M. Archibald, Antônio H. Ribeiro, Fabian Pedregosa, Paul van Mulbregt, and SciPy 1.0 Contributors. SciPy 1.0: Fundamental Algorithms for Scientific Computing in Python. *Nature Methods*, 17:261–272, 2020. doi: 10.1038/s41592-019-0686-2.

[241] A. Vourlidas, B. J. Lynch, R. A. Howard, and Y. Li. How Many CMEs Have Flux Ropes? Deciphering the Signatures of Shocks, Flux Ropes, and Prominences in Coronagraph Observations of CMEs. *Solar Physics*, 284(1): 179–201, May 2013. ISSN 1573-093X. doi: 10.1007/s11207-012-0084-8.

[242] Bojan Vršnak, Karl-Ludwig Klein, Alexander Warmuth, Wolfgang Otruba, and Marina Skender. Vertical Dynamics of the Energy Release Process in a Simple two-Ribbon Flare. *Sol. Phys.*, 214(2):325–338, Jun 2003. ISSN 0038-0938. doi: 10.1023/A:1024273512811.

[243] Haimin Wang and Chang Liu. Structure and evolution of magnetic fields associated with solar eruptions. *Research in Astronomy and Astrophysics*, 15(2): 145–174, feb 2015. ISSN 1674-4527. doi: 10.1088/1674-4527/15/2/001. URL `https://iopscience.iop.org/article/10.1088/1674-4527/15/2/001`.

[244] Haimin Wang, B. Chen, Ju Jing, Sijie Yu, Chang Liu, Vasyl B. Yurchyshyn, Kwangsu Ahn, Takenori Okamoto, Shin Toriumi, Wenda Cao, and Dale E. Gary. Multi-wavelength Multi-height Study of Super Strong Surface and Coronal Magnetic Fields in Active Region 12673. *American Astronomical Society Meeting Abstracts #234*, 234:402.05, Jun 2019. URL `https://ui.adsabs.harvard.edu/abs/2019AAS...23440205W/abstract`.

[245] Tongjiang Wang, Linhui Sui, and Jiong Qiu. Direct Observation of High-Speed Plasma Outflows Produced by Magnetic Reconnection in Solar Impulsive Events. *The Astrophysical Journal*, 661(2):L207, May 2007. ISSN 0004-637X. doi: 10.1086/519004.

[246] Yuming Wang and J. Zhang. A Comparative Study between Eruptive X-class Flares Associated with Coronal Mass Ejections and Confined X-class Flares. 210:29.17, May 2007.

[247] Harry P. Warren, John T. Mariska, and George A. Doschek. Observations of Thermal Flare Plasma With the Euv Variability Experiment. *The Astrophysical Journal*, 770(2):116, June 2013. ISSN 0004-637X. doi: 10.1088/0004-637X/770/2/116.

[248] David F. Webb and Timothy A. Howard. Coronal Mass Ejections: Observations. *Living Reviews in Solar Physics*, 9, 2012. ISSN 1614-4961. doi: 10.12942/lrsp-2012-3. URL `http://link.springer.com/10.12942/lrsp-2012-3`.

[249] David F. Webb and Timothy A. Howard. Coronal Mass Ejections: Observations. *Living Reviews in Solar Physics*, 9(1):3, June 2012. ISSN 1614-4961. doi: 10.12942/lrsp-2012-3.

[250] Brian T. Welsch. Flux Accretion and Coronal Mass Ejection Dynamics. *Solar Physics*, 293(7):113, July 2018. ISSN 1573-093X. doi: 10.1007/s11207-018-1329-y.

[251] S. M. White, A. O. Benz, S. Christe, F. Fárník, M. R. Kundu, G. Mann, Z. Ning, J.-P. Raulin, A. V. R. Silva-Válio, P. Saint-Hilaire, N. Vilmer, and A. Warmuth. The Relationship Between Solar Radio and Hard X-ray Emission. *Space Science Reviews*, 159(1-4):225–261, sep 2011. ISSN 0038-6308. doi: 10.1007/s11214-010-9708-1. URL `http://link.springer.com/10.1007/s11214-010-9708-1`.

[252] T. Wiegelmann. Nonlinear force-free modeling of the solar coronal magnetic field. *J. Geophys. Res. Space Phys.*, 113(A3), Mar 2008. ISSN 0148-0227. doi: 10.1029/2007JA012432.

[253] T. N. Woods, F. G. Eparvier, R. Hock, A. R. Jones, D. Woodraska, D. Judge, L. Didkovsky, J. Lean, J. Mariska, H. Warren, D. McMullin, P. Chamberlin,

G. Berthiaume, S. Bailey, T. Fuller-Rowell, J. Sojka, W. K. Tobiska, and R. Viereck. Extreme Ultraviolet Variability Experiment (EVE) on the Solar Dynamics Observatory (SDO): Overview of Science Objectives, Instrument Design, Data Products, and Model Developments. In Phillip Chamberlin, William Dean Pesnell, and Barbara Thompson, editors, *The Solar Dynamics Observatory*, pages 115–143. Springer US, New York, NY, 2012. ISBN 978-1-4614-3673-7. doi: 10.1007/978-1-4614-3673-7_7.

[254] Thomas N. Woods, Francis G. Eparvier, Juan Fontenla, Jerald Harder, Greg Kopp, William E. McClintock, Gary Rottman, Byron Smiley, and Martin Snow. Solar irradiance variability during the October 2003 solar storm period. *Geophysical Research Letters*, 31(10), 2004. ISSN 1944-8007. doi: 10.1029/2004GL019571.

[255] S. T. Wu, W. P. Guo, D. J. Michels, and L. F. Burlaga. MHD description of the dynamical relationships between a flux rope, streamer, coronal mass ejection, and magnetic cloud: An analysis of the January 1997 Sun-Earth connection event. *Journal of Geophysical Research: Space Physics*, 104(A7):14789–14801, 1999. ISSN 2156-2202. doi: 10.1029/1999JA900099.

[256] Jean-Pierre Wuelser, James R. Lemen, Theodore D. Tarbell, C. Jacob Wolfson, Joseph C. Cannon, Brock A. Carpenter, Dexter W. Duncan, Glenn S. Gradwohl, Syndie B. Meyer, Augustus S. Moore, Rosemarie L. Navarro, J. Dunagan Pearson, George R. Rossi, Larry A. Springer, Russell A. Howard, John Daniel Moses, Jeffrey S. Newmark, Jean-Pierre Delaboudiniere, Guy Edouard Artzner, Frederic Auchere, Marie Bougnet, Philippe Bouyries, Francoise Bridou, Jean-Yves Clotaire, Gerard Colas, Franck Delmotte, Arnaud Jerome, Michel Lamare, Raymond Mercier, Michel Mullot, Marie-Francoise Ravet, Xueyan Song, Volker Bothmer, and Werner Deutsch. EUVI: The STEREO-SECCHI extreme

ultraviolet imager. In *Telescopes and Instrumentation for Solar Astrophysics*, volume 5171, pages 111–122. SPIE, February 2004. doi: 10.1117/12.506877.

[257] Zhike Xue, Xiaoli Yan, Xin Cheng, Liheng Yang, Yingna Su, Bernhard Kliem, Jun Zhang, Zhong Liu, Yi Bi, Yongyuan Xiang, Kai Yang, and Li Zhao. Observing the release of twist by magnetic reconnection in a solar filament eruption. *Nature Communications*, 7(1):11837, June 2016. ISSN 2041-1723. doi: 10.1038/ncomms11837.

[258] Masaaki Yamada, Russell Kulsrud, and Hantao Ji. Magnetic reconnection. *Reviews of Modern Physics*, 82(1):603–664, March 2010. doi: 10.1103/RevModPhys.82.603.

[259] Zihao Yang, Christian Bethge, Hui Tian, Steven Tomczyk, Richard Morton, Giulio Del Zanna, Scott W. McIntosh, Bidya Binay Karak, Sarah Gibson, Tanmoy Samanta, Jiansen He, Yajie Chen, and Linghua Wang. Global maps of the magnetic field in the solar corona. *Science*, 369(6504):694–697, aug 2020. ISSN 10959203. doi: 10.1126/science.abb4462. URL `https://science.sciencemag.org/content/369/6504/694https://science.sciencemag.org/content/369/6504/694.abstract`.

[260] Sijie Yu, B. Chen, Katharine K. Reeves, Dale E. Gary, Sophie Musset, Gregory D. Fleishman, Gelu M. Nita, and Lindsay Glesener. Magnetic Reconnection during the Post-impulsive Phase of a Long-duration Solar Flare: Bidirectional Outflows as a Cause of Microwave and X-Ray Bursts. *The Astrophysical Journal*, 900(1):17, aug 2020. ISSN 1538-4357. doi: 10.3847/1538-4357/aba8a6. URL `https://iopscience.iop.org/article/10.3847/1538-4357/aba8a6`.

[261] V. Yurchyshyn, P. Kumar, V. Abramenko, Y. Xu, P. R. Goode, K.-S. Cho, and E.-K. Lim. High-resolution Observations of a White-light Flare with NST. *The Astrophysical Journal*, 838(1):32, March 2017. ISSN 0004-637X. doi: 10.3847/1538-4357/aa633f.

[262] S. Zenitani and M. Hoshino. The Generation of Nonthermal Particles in the Relativistic Magnetic Reconnection of Pair Plasmas. *The Astrophysical Journal*, 562(1):L63, November 2001. ISSN 0004-637X. doi: 10.1086/337972.

[263] J. Zhang, K. P. Dere, R. A. Howard, M. R. Kundu, and S. M. White. On the Temporal Relationship between Coronal Mass Ejections and Flares. *The Astrophysical Journal*, 559(1):452, September 2001. ISSN 0004-637X. doi: 10.1086/322405.

[264] Jie Zhang, Xin Cheng, and Ming-de Ding. Observation of an evolving magnetic flux rope before and during a solar eruption. *Nature Communications*, 3(1):747, March 2012. ISSN 2041-1723. doi: 10.1038/ncomms1753.

[265] L.-L. Zhao, G. P. Zank, O. Khabarova, S. Du, Y. Chen, L. Adhikari, and Q. Hu. An Unusual Energetic Particle Flux Enhancement Associated with Solar Wind Magnetic Island Dynamics. *The Astrophysical Journal Letters*, 864(2):L34, September 2018. ISSN 2041-8205. doi: 10.3847/2041-8213/aaddf6.

[266] Guiping Zhou, Jingxiu Wang, and Zhuoliang Cao. Correlation between halo coronal mass ejections and solar surface activity. *Astronomy & Astrophysics*, 397(3):1057–1067, January 2003. ISSN 0004-6361, 1432-0746. doi: 10.1051/0004-6361:20021463.

[267] Chunming Zhu, Jiong Qiu, Paulett Liewer, Angelos Vourlidas, Michael Spiegel, and Qiang Hu. How Does Magnetic Reconnection Drive the Early-stage

Evolution of Coronal Mass Ejections? *The Astrophysical Journal*, 893(2):141, April 2020. ISSN 0004-637X. doi: 10.3847/1538-4357/ab838a.

[268] Ivan Zimovets, Ivan Sharykin, and Ivan Myshyakov. Quasi-Periodic Energy Release in a Three-Ribbon Solar Flare. *Solar Physics*, 296(12):188, December 2021. ISSN 1573-093X. doi: 10.1007/s11207-021-01936-9.